

## Programmable quantum simulations of spin systems with trapped ions

C. Monroe\*

*Joint Quantum Institute and Joint Center on Quantum Information and Computer Science,  
University of Maryland Department of Physics and  
National Institute of Standards and Technology, College Park, Maryland 20742, USA*

W. C. Campbell

*Department of Physics and Astronomy, University of California,  
Los Angeles, California 90095, USA*

L.-M. Duan

*Center for Quantum Information, Institute for Interdisciplinary Information Sciences,  
Tsinghua University, Beijing 100084, China*

Z.-X. Gong

*Department of Physics, Colorado School of Mines, Golden, Colorado 80401, USA*

A. V. Gorshkov

*Joint Quantum Institute and Joint Center on Quantum Information and Computer Science,  
University of Maryland Department of Physics and  
National Institute of Standards and Technology, College Park, Maryland 20742, USA*

P. W. Hess

*Department of Physics, Middlebury College, Middlebury, Vermont 05753, USA*

R. Islam

*Institute for Quantum Computing and Department of Physics and Astronomy,  
University of Waterloo, Waterloo, Ontario N2L 3G1, Canada*

K. Kim

*Center for Quantum Information, Institute for Interdisciplinary Information Sciences,  
Tsinghua University, Beijing 100084 China*

N. M. Linke

*Joint Quantum Institute, University of Maryland Department of Physics,  
College Park, Maryland 20742, USA*

G. Pagano

*Department of Physics and Astronomy, Rice University, Houston, Texas 77005, USA*


P. Richerme

*Department of Physics, Indiana University, Bloomington, Indiana 47405, USA*

C. Senko

*Institute for Quantum Computing and Department of Physics and Astronomy,  
University of Waterloo, Waterloo, Ontario N2L 3G1, Canada*

N. Y. Yao

*Department of Physics, University of California, Berkeley California 94720, USA* (published 7 April 2021)

Laser-cooled and trapped atomic ions form an ideal standard for the simulation of interacting quantum spin models. Effective spins are represented by appropriate internal energy levels within each ion, and the spins can be measured with near-perfect efficiency using state-dependent fluorescence techniques. By applying optical fields that exert optical dipole forces on the ions, their Coulomb interaction can be modulated to produce long-range and tunable spin-spin interactions that can be reconfigured by shaping the spectrum and pattern of the laser fields in a prototypical example of a quantum simulator. Here the theoretical mapping of atomic ions to interacting spin systems, the preparation of complex equilibrium states, and the study of dynamical processes in these many-body interacting quantum systems are reviewed, and the use of this platform for optimization and other tasks is discussed. The use of such quantum simulators for studying spin models may inform our understanding of exotic quantum materials and shed light on the behavior of interacting quantum systems that cannot be modeled with conventional computers.

DOI: [10.1103/RevModPhys.93.025001](https://doi.org/10.1103/RevModPhys.93.025001)**CONTENTS**

I. Introduction	2
A. Atomic ion spins	3
B. Coulomb-collective motion of trapped-ion crystals	4
C. Programmable magnetic fields and interactions between trapped-ion spins	5
1. Effective magnetic fields	7
2. Effective Ising interactions	7
II. Spin Hamiltonian Benchmarking and Many-Body Spectroscopy	10
A. Sources of error	11
B. Benchmarking Ising couplings	12
III. Equilibrium studies	13
A. Adiabatic ground-state preparation	14
1. Adiabatic ramp profiles	14
2. General adiabatic simulation issues	16
B. Experimental progress in adiabatic quantum simulation	17
1. Transverse Ising model with a small number of spins	17
2. Onset of quantum many-body effects with increasing system size	19
3. Ground-state identification	21
4. Classical Ising model	21
5. Spin-1 simulations	23
IV. Nonequilibrium Phases of Matter and Dynamics	26
A. Information propagation	27
B. Disorder-induced localization	28
C. Prethermalization	32
D. Stroboscopic dynamics and Floquet phases of matter	34
E. Dynamical phase transitions	36
V. Hamiltonian Sequencing and Engineering	38
A. Trotter Hamiltonian expansion	39
B. Variational quantum simulation	40
1. Variational quantum eigensolvers	41
2. Quantum approximate optimization algorithms	44
VI. Outlook and Future Challenges	46

Acknowledgments	47
References	47

**I. INTRODUCTION**

Interacting quantum systems cannot generally be efficiently simulated using classical computational techniques, due to the exponential scaling of the information encoded in a quantum state with the size of the system. Accurate modeling of quantum phenomena such as the magnetism of interacting spins, material superconductivity, electronic structure and molecules and their chemistry, Fermi-Hubbard models of electron transport in solids, and interactions within atomic nuclei is beyond the reach of classical computation even for small numbers of interacting degrees of freedom. A quantum simulator exploits the controlled manipulation of a standard quantum system in order to mimic the properties or evolution of a different (perhaps intractable) quantum system (Feynman, 1982; Trabesinger, 2012). A quantum simulator is a restricted quantum computer (Nielsen and Chuang, 2000; Ladd *et al.*, 2010), with operations that may not be universal but instead may be tailored to a particular quantum physical model under study. While useful general purpose and universal quantum computers are still a future prospect, special purpose quantum simulations have already been demonstrated and may in fact become the first useful application of quantum computers.

The equivalence of quantum bits (qubits) and their quantum gates to effective spin-1/2 systems and their interactions has guided one of the most important classes of quantum simulations: interacting spin systems and quantum magnetism. The most advanced physical system for quantum bits or effective spins is arguably a collection of trapped atomic ions (Steane, 1997; Wineland *et al.*, 1998; Wineland and Blatt, 2008; Monroe and Kim, 2013; Brown, Kim, and Monroe, 2016). This is evidenced by the number of controlled and interacting qubits, the quality of quantum gates and interactions, and the high fidelity of quantum state initialization and measurement. Trapped atomic ions, held in a vacuum chamber and confined by electromagnetic fields to be distant

\*Corresponding author.  
monroe@umd.edu

from surfaces or solids, laser cooled to be nearly at rest and “wired” together with external laser or microwave fields, offer a clean quantum system to perform quantum simulations (Porras and Cirac, 2004; Deng, Porras, and Cirac, 2005; Taylor and Calarco, 2008; Blatt and Roos, 2012).

This review assesses recent progress in the quantum simulation of magnetism and related phenomena using trapped atomic ion crystals. Following an introduction of the mapping of spins to atomic ions, we first cover experimental results on the simulation of magnetic ordering, equilibrium states, and phase transitions in quantum magnetic systems. Then we move to dynamical studies of quantum magnetism, touching on general issues of information and entanglement dynamics, quantum thermalization, inhibitors to thermalization such as many-body localization and prethermalization, “time crystals,” dynamical phase transitions, and Hamiltonian engineering and sequencing techniques that translate quantum physics models to effective magnetic spin models. Recent techniques of variational quantum simulations (VQSS) and quantum approximate optimization algorithms are also reviewed in the context of trapped-ion systems. We conclude with speculations on how these types of simulations with trapped ions may scale in the future and perhaps guide the development of a real magnetic material function or more general quantum simulations as special cases of quantum computations. Trapped-ion spin simulators generally exploit the collective motion of the ions to generate many-body spin interactions, with a controlled coupling through collective bosonic harmonic oscillator modes, or phonons. While not a focus of this review, the phonon degree of freedom itself is an interesting medium to host quantum simulations of bosonic models and is complementary to the field of photonic cavity QED in atomic (Raimond, Brune, and Haroche, 2001; Ye, Kimble, and Katori, 2008) and superconducting (Wallraff *et al.*, 2004) systems. There have been many demonstrations of phonon control and phonon-based simulations in systems of a few trapped ions (Ben-Kish *et al.*, 2003; Um *et al.*, 2016; Kienzler *et al.*, 2017), including bosonic interference (Leibfried *et al.*, 2002; Toyoda *et al.*, 2015), blockades (Debnath *et al.*, 2018; Ohira *et al.*, 2020), sampling molecular vibronic spectra (Shen *et al.*, 2018), quantum walks (Schmitz *et al.*, 2009; Zähringer *et al.*, 2010), spin-boson simulations (Lv *et al.*, 2018), phononic “lasing” (Vahala *et al.*, 2009; Ip *et al.*, 2018) and energy transfer (Gorman *et al.*, 2018), three-body phonon interactions (Ding *et al.*, 2018), quantum thermodynamics (An *et al.*, 2015), and quantum heat engines and refrigerators (Roßnagel *et al.*, 2016; Maslennikov *et al.*, 2019).

We note that there are many other quantum systems amenable to quantum spin simulation, including superconducting circuits (Kandala *et al.*, 2017; Otterbach *et al.*, 2017; Arute *et al.*, 2019), neutral atoms in optical lattices (Gross and Bloch, 2017), and solid-state arrays of effective individual spin systems (J. Choi *et al.*, 2017; S. Choi *et al.*, 2017). Comparisons to these other platforms is made where appropriate, although many of the simulations covered in this review rely on individual quantum state control with long-range interactions not native to other platforms.

## A. Atomic ion spins

We represent a collection of spins by a crystal of electro-magnetically trapped atomic ions, with two electronic energy levels within each ion behaving as an effective spin-1/2 particle. The choice of electronic levels depends on the atomic element and also the desired type of control fields used to manipulate and measure the spin state. The most important features of these spin states for executing quantum simulations are (a) the spin levels are long lived and exhibit excellent coherence properties, (b) the spin states have appropriate strong optical transitions to auxiliary excited states, with selection rules allowing for qubit initialization through optical pumping and qubit detection through fluorescence, and (c) the spins interact through a coherent coupling that can be externally controlled and gated. These requirements restrict the atomic species to a handful of elements and spin states that are encoded in either  $S_{1/2}$  hyperfine or Zeeman ground states of single outer-electron atoms (such as  $\text{Be}^+$ ,  $\text{Mg}^+$ ,  $\text{Ca}^+$ ,  $\text{Sr}^+$ ,  $\text{Ba}^+$ ,  $\text{Cd}^+$ ,  $\text{Zn}^+$ ,  $\text{Hg}^+$ , and  $\text{Yb}^+$ ) with radio-frequency or microwave frequency splittings or ground and  $D$  or  $F$  metastable electronic excited states of single or dual outer-electron atoms (such as  $\text{Ca}^+$ ,  $\text{Sr}^+$ ,  $\text{Ba}^+$ ,  $\text{Yb}^+$ ,  $\text{B}^+$ ,  $\text{Al}^+$ ,  $\text{Ga}^+$ ,  $\text{In}^+$ ,  $\text{Hg}^+$ ,  $\text{Tl}^+$ , and  $\text{Lu}^+$ ) with optical frequency splittings. Some species (such as  $\text{Ba}^+$ ,  $\text{Lu}^+$ , and  $\text{Yb}^+$ ) have sufficiently long  $D$  or  $F$  metastable excited state lifetimes to host spins in their hyperfine or Zeeman levels with radio-frequency or microwave splittings.

In any of these systems, we label the two relevant spin states as  $|\downarrow\rangle \equiv |\downarrow_z\rangle$  and  $|\uparrow\rangle \equiv |\uparrow_z\rangle$ , eigenstates of the Pauli operator  $\sigma_z$  separated by energy  $E_\uparrow - E_\downarrow = \hbar\omega_0$ . In the transverse bases of the Bloch sphere, we define by convention the eigenstates of  $\sigma_x$  as  $|\downarrow_x\rangle \equiv (|\downarrow\rangle - |\uparrow\rangle)/\sqrt{2}$  and  $|\uparrow_x\rangle \equiv (|\downarrow\rangle + |\uparrow\rangle)/\sqrt{2}$ , and the eigenstates of  $\sigma_y$  as  $|\downarrow_y\rangle \equiv (|\downarrow\rangle + i|\uparrow\rangle)/\sqrt{2}$  and  $|\uparrow_y\rangle \equiv (i|\downarrow\rangle + |\uparrow\rangle)/\sqrt{2}$ . We note that in this review the spin direction is often not explicitly labeled, in which case the notation adopts the context of the material.

A typical quantum simulation in the ion-trap system is composed of three sequential steps: initialization, interaction, and measurement, as depicted in Fig. 1. The spins are initialized through an optical pumping process that prepares each spin in a nearly pure quantum state (Happer, 1972). By applying resonant laser radiation that couples the spin states to short-lived excited states, each spin can be initialized with >99.9% state purity in a few microseconds. This relies on appropriate selection rules for the excited states as well as sufficiently split energy levels of the spin states themselves [Fig. 1(a)]. Laser cooling can prepare the motional states of the ions to near the ground state of harmonic motion (Leibfried *et al.*, 2003), which is important for the control of the spin-spin interactions detailed later.

Each spin can be coherently manipulated by driving the atomic ions with external fields that couple the spin states. This can be accomplished by resonantly driving the spin levels with appropriate radiation at frequency  $\omega_0$ ; in Fig. 1(b), this is depicted as a two-field Raman process, with a beat note of two optical fields at  $\omega_0$  driving the spin (this is assumed throughout unless otherwise indicated). This coherent coupling can also drive motional sideband transitions (Leibfried *et al.*,

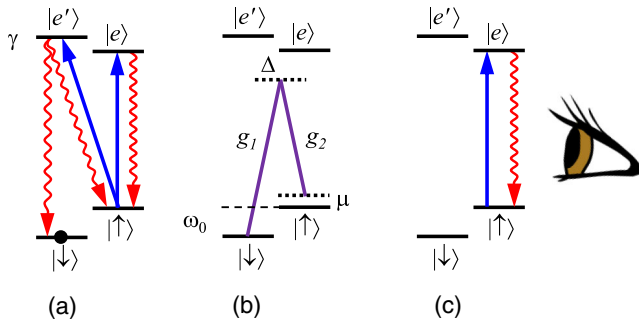


FIG. 1. Reduced energy level diagram of a single atomic ion. Effective spin-1/2 systems are encoded within each atomic ion as stable electronic energy levels  $|\downarrow\rangle$  and  $|\uparrow\rangle$ . A typical quantum simulation is composed of three steps. (a) Resonant radiation (blue solid arrows) connects one of the two spin states to a pair of excited state levels (linewidth  $\gamma$ ) and optically pumps each spin to the  $|\downarrow\rangle$  state through spontaneous emission (red wavy arrows). Here we assume that the excited state  $|e\rangle$  couples only to  $|\uparrow\rangle$ , while the other excited state  $|e'\rangle$  couples to both spin states. (Other sets of selection rules are also possible.) (b) In the case of ground-state (Zeeman or hyperfine) defined spins separated by frequency  $\omega_0$ , two tones of off-resonant radiation (purple solid lines) can drive stimulated Raman transitions between the spin states. The two beams have resonant Rabi frequencies  $g_{1,2}$  connecting respective spin states to excited states and are detuned by  $\Delta \gg \gamma$  and have a difference frequency (beat note) detuned from the spin resonance by  $\mu$ . This coherently couples the spin states to create superpositions ( $\mu = 0$ ) and for non-copropagating beams also couples to the motion of the ion crystal ( $\mu \neq 0$ ). These processes can also be driven directly by radio-frequency or microwave signals, or, for optically defined spin states, a single laser tone. (c) Resonant radiation (blue solid arrow) drives the  $|\uparrow\rangle \leftrightarrow |e\rangle$  cycling transition, causes the  $|\uparrow\rangle$  state to fluoresce strongly (red wavy arrow), while the  $|\downarrow\rangle$  state is far from resonance and therefore dark. This allows the near-perfect detection of the spin state by the collection of this state-dependent fluorescence depicted by the eye.

2003) that couple the spin to the motion of the ion. For multiple ions, this can be used to generate spin-spin couplings mediated by the Coulomb interaction, described in more detail later (Wineland and Blatt, 2008). These external fields provide exquisite control over the effective spin-spin interaction, with the ability to gate the interaction, program different forms of the interaction strength and range, and even reconfigure the interaction graph topology.

At the end of the quantum simulation, the spins are measured by applying resonant laser radiation that couples one of the two spin states to a short-lived excited state through a cycling transition and detecting the resulting fluorescence (Bergquist *et al.*, 1986; Nagourney, Sandberg, and Dehmelt, 1986; Sauter *et al.*, 1986). This is depicted in Fig. 1(c), where we take the  $|\uparrow\rangle$  or “bright” state as fluorescing and the  $|\downarrow\rangle$  or “dark” state as not fluorescing. Even though the photon collection efficiency may be small (typically less than 1%), the effective spin detection efficiency can be well above 99% owing to the low probability of leaving the fluorescence cycle or having the other (dark) state entering the cycle (Acton *et al.*, 2006; Hume, Rosenband, and Wineland, 2007; Benhelm *et al.*, 2008; Myerson *et al.*, 2008; Noek *et al.*,

2013). To detect the spins in other bases in the Bloch sphere ( $\sigma_x$  or  $\sigma_y$ ), prior to fluorescence measurement the spins are coherently rotated by polar angle  $\pi/2$  along the  $y$  or  $x$  axis of the Bloch sphere, respectively.

## B. Coulomb-collective motion of trapped-ion crystals

Atomic ions can be confined in free space with electromagnetic fields supplied by nearby electrodes. Two types of ion traps are used for quantum simulation experiments: the linear radio-frequency (rf) trap and the Penning trap. The linear rf trap (Fig. 2) (Raizen *et al.*, 1992) juxtaposes a static axial confining potential with a two-dimensional rf quadrupole potential that provides a time-averaged or ponderomotive transverse confinement potential (Dehmelt, 1968; Wolfgang, 1990). The trap anisotropy is typically adjusted so that the static axial confinement is much weaker than the transverse confinement and that laser-cooled ions reside on the axis of the trap where the rf fields are null, resulting in a one-dimensional chain of trapped-ion spins. A harmonic axial confinement potential results in an anisotropic linear ion spacing (James, 1998), but the ions can be made nearly equidistant by applying an appropriate quartic axial confining potential (Lin *et al.*, 2009). The Penning trap [Fig. 2(b)] employs a uniform axial magnetic field with static axial electric field confinement, where the transverse confinement is provided by the  $\mathbf{E} \times \mathbf{B}$  drift toward the axis (Brown and Gabrielse, 1986; Bohnet *et al.*, 2016). Here the trap anisotropy is typically adjusted so that the ions form a two-dimensional crystal perpendicular to and rotating about the axis. Both rf and Penning traps can be modified to support other types of crystals in any number of spatial dimensions, but the quantum simulations reviewed here are either 1D chains in rf traps or 2D crystals in Penning traps. However, the dimensionality of the spin-spin interaction graph does not necessarily follow that of the spatial arrangement of spins.

Ions are typically loaded into traps by generating neutral atoms of the desired element and ionizing the atoms once in the trapping volume via electron bombardment or photoionization. Ion-trap depths are usually much larger than room temperature, so rare collisions with background gas do not necessarily eject the ion from the trap, but they can temporarily break up the crystal and scramble the atomic ions in space. Under typical ultrahigh-vacuum conditions, these collisional interruptions occur roughly once per hour per ion (Wineland *et al.*, 1998), but cryogenic vacuum chambers, where the trapped ions can be undisturbed for weeks or longer between collisions, can reduce the collision rate by orders of magnitude.

When atomic ions are laser cooled and localized well below their mean spacing, they form a stable crystal, with the Coulomb repulsion balancing the external confinement force. Typical spacings between adjacent ions in trapped-ion crystals are  $\sim 3\text{--}20\ \mu\text{m}$ , depending on the ion mass, the number of ions in the crystal, the characteristic dimensions of the electrodes, and the applied potential values. The equilibrium positions of ions in the crystal can be calculated numerically (Steane, 1997; James, 1998; Sawyer *et al.*, 2012). The motion of the ions away from their equilibrium positions is well described by harmonic normal modes of oscillation (phonon modes),

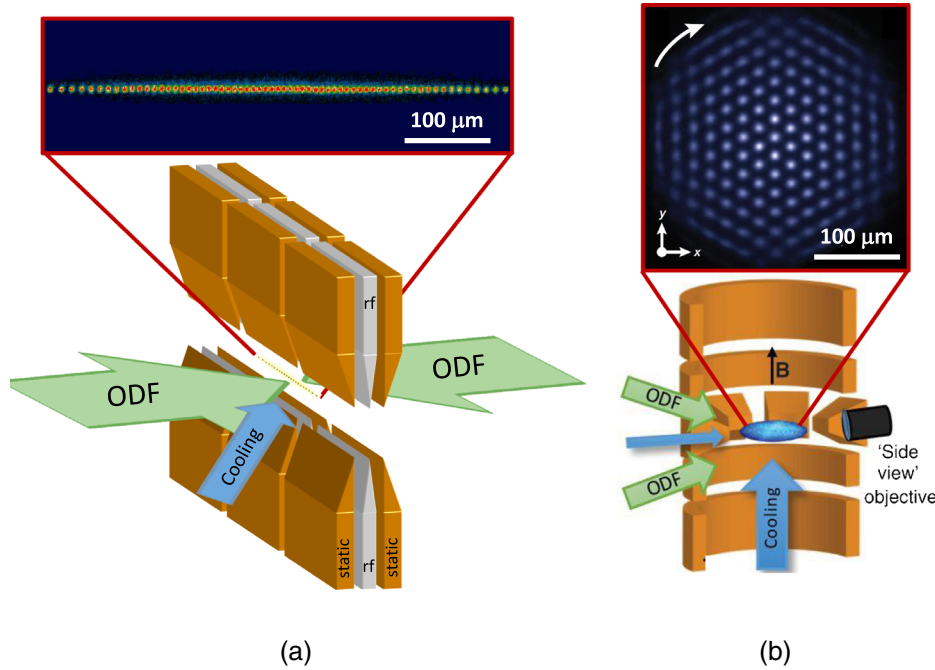


FIG. 2. (a) Radio-frequency (rf) linear trap used to prepare a 1D crystal of atomic ions. The geometry in this trap has three layers of electrodes, with the central (gray) layer carrying rf potentials to generate a 2D quadrupole along the axis of the trap. The outer (gold) electrodes confine the ions along the axis of the trap. For sufficiently strong transverse confinement, the ions form a linear crystal along the trap axis, with an image of 64 ions shown above with characteristic spacing  $5 \mu\text{m}$  for  $^{171}\text{Yb}^+$  ions. From [Islam \*et al.\*, 2011](#). (b) Penning trap used to prepare a 2D crystal of atomic ions. The cylindrical (gold) electrodes provide a static quadrupole field that confines the ions along the vertical axis, and the vertical magnetic field stabilizes their orbits in the transverse plane. For sufficiently strong axial confinement, the lowest energy configuration of the ions is a single plane triangular lattice that undergoes rigid body rotation, with an image of  $\sim 200$   $^9\text{Be}^+$  ions shown above with a characteristic spacing of  $20 \mu\text{m}$ . From [Bohnet \*et al.\*, 2016](#). For both traps, wide arrows (green) indicate non-copropagating optical dipole force (ODF) laser beams that provide spin-dependent forces along their wave vector difference, giving rise to Ising couplings. The other arrows indicate cooling and spin detection beams (imaging objectives are not shown).

with frequencies in the range  $\omega_m/2\pi \sim 0.1\text{--}10$  MHz. The thermal motion of laser-cooled ions and also the driven motion by external forces are typically at the  $10\text{--}100$  nm scale. This is much smaller than the inter-ion spacing, so nonlinearities to the phonon modes ([Marquet, Schmidt-Kaler, and James, 2003](#)) can be safely neglected and the harmonic approximation to the phonon modes is justified. Calculations of the phonon mode frequencies and normal mode eigenfunctions follow straightforwardly from the calculated ion spacings ([Steane, 1997](#); [James, 1998](#); [Sawyer \*et al.\*, 2012](#)). For the systems described here, we primarily consider the motion along a single spatial dimension labeled  $X$ . We write the  $X$  component of the position of the  $i$ th ion as  $\hat{X}_i = \bar{X}_i + \hat{x}_i$ , separating the mean stationary position  $\bar{X}_i$  of the  $i$ th ion from the small harmonic oscillations described by the quantum position operator  $\hat{x}_i$ . The motion of ions in the crystal is tightly coupled by the Coulomb interaction, so it is natural to express the position operator in terms of the  $m = 1, \dots, N$  normal phonon modes  $\hat{x}_i = \sum_{m=1}^N b_{im} \hat{\xi}_m$ , where  $b_{im}$  is the normal mode transformation matrix, with  $\sum_i b_{im} b_{in} = \delta_{nm}$  and  $\sum_m b_{im} b_{jm} = \delta_{ij}$ . Each phonon mode  $\hat{\xi}_m$  oscillates at frequency  $\omega_m$  and can be described as a quantum harmonic oscillator with zero-point spatial spread  $\xi_m^{(0)} = \sqrt{\hbar/2M\omega_m}$ , where  $M$  is the mass of a single ion. In the interaction frame

for each phonon mode, the position of the  $i$ th ion is thus written as

$$\hat{X}_i = \bar{X}_i + \sum_{m=1}^N b_{im} \xi_m^{(0)} (a_m^\dagger e^{i\omega_m t} + a_m e^{-i\omega_m t}), \quad (1)$$

where  $a_m^\dagger$  and  $a_m$  are bosonic raising and lowering operators for each mode, with  $[a_n, a_m^\dagger] = \delta_{nm}$ .

In general, the structure of transverse phonon modes of a 1D or 2D ion crystal (motion perpendicular to the axis or plane of the ions) has the center-of-mass (c.m.) mode as its highest frequency, with the lowest frequency corresponding to zigzag motion where adjacent ions move in opposite directions, as shown in [Fig. 3](#) for a 1D linear chain of 32 ions and a 2D crystal of about 345 ions. The bandwidth of the transverse modes can be controlled by tuning the spatial anisotropy of the trap.

### C. Programmable magnetic fields and interactions between trapped-ion spins

Effective magnetic fields and spin-spin interactions can be realized by applying external microwave or optical fields to the ions. We consider the case of optical fields, since not only

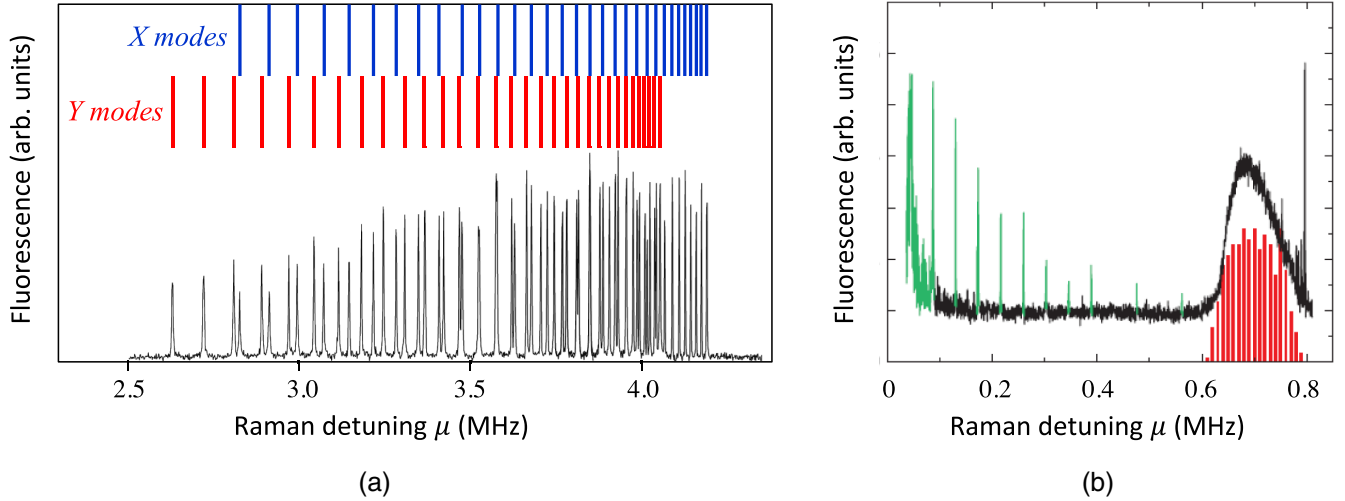


FIG. 3. Raman upper sideband spectrum of the transverse motion of trapped atomic ion crystals. The spectrum is measured by preparing all of the ions in the (dark) state  $|\downarrow\rangle$  and driving them with global Raman laser beams with beat-note detuning  $\mu$  from the spin-flip resonance and measuring the total fluorescence of the chain, which responds when the beat note matches a sideband resonance. (a) 32 trapped  $^{171}\text{Yb}^+$  atomic ions in a linear chain; see Fig. 2(a). Here the Raman excitation is sensitive to both the  $X$  and  $Y$  principal axes of transverse motion, and the theoretical position of both sets of 32 modes along  $X$  and  $Y$  are indicated at the top. The highest frequency sidebands correspond to center-of-mass (c.m.) modes at 4.19 MHz for the  $X$  direction and 4.05 MHz for the  $Y$  direction. Based on unpublished data from the University of Maryland. (b) Measured (black) and calculated [red (gray) lines between 0.6 and 0.8 MHz] sideband spectrum for a 2D crystal of  $345 \pm 25$   $^9\text{Be}^+$  ions in a Penning trap; see Fig. 2(b) with rotation frequency 43.2 kHz. As in the linear chain, the highest frequency sideband at 795 kHz corresponds to c.m. motion. Features at the rotation frequency and its harmonics at low frequency [green (gray)] are due to residual couplings to in-plane degrees of freedom from imperfect beam alignment. Adapted from [Sawyer \*et al.\*, 2012](#).

can they be used to provide effective site-dependent magnetic fields for the spins through tight focusing, but the strong dipole forces from laser beams can also drive effective Ising interactions between the spins ([Cirac and Zoller, 1995](#); [Solano, de Matos Filho, and Zagury, 1999](#); [Sørensen and Mølmer, 1999](#); [Milburn, Schneider, and James, 2000](#)). Such forces can be applied to pairs of ions in order to execute entangling quantum gates applicable to quantum computing ([Wineland and Blatt, 2008](#)). When such forces are instead applied more globally, the resulting interaction network allows the quantum simulation of a variety of spin models, such as the Ising and Heisenberg spin chains ([Porras and Cirac, 2004](#); [Deng, Porras, and Cirac, 2005](#); [Taylor and Calarco, 2008](#)).

Following Fig. 1(b) and assuming that the spins are encoded in stable (Zeeman or hyperfine) levels, the ion crystal is addressed with two laser beams detuned from the excited states by much more than the excited state radiative linewidth ( $\Delta \gg \gamma$ ). By adiabatically eliminating the excited states, this drives coherent Raman transitions between the spin states. Alternatively, optically defined spin levels can be coupled with a single laser beam ([Benhelm \*et al.\*, 2008](#)), but this is more difficult technically, as the spins acquire an optical phase that requires extreme positional stability of the optical setup. With rf- or microwave-defined spin states, the relevant phase is that of the microwave beat note between the Raman beams, which has a much longer wavelength and is easier to control and stabilize. The two Raman beams are oriented to have a projection  $\delta k$  of their wave vector difference along the  $X$  axis of motion. The Raman beat note is detuned by frequency  $\omega_0 + \mu_i$  from the resonance of spin  $i$  with beat-note phase  $\delta\phi_i$ .

The resonant Raman Rabi frequency on ion  $i$  is  $\Omega_i = g_1^i g_2^i / 2\Delta$ , where  $g_{1,2}^i$  are the direct single field Rabi frequencies of the associated transitions through the excited states [see Fig. 1(b)], proportional to the respective applied optical electric fields. The atom-light interaction Hamiltonian in a frame rotating at the spin resonance frequency  $\omega_0 \gg \Omega_i$  (optical rotating-wave approximation) takes the form ( $\hbar = 1$ )

$$H = \frac{1}{2} \sum_i [\Omega_i (\sigma_+^i e^{i(\delta k \hat{X}_i - \mu_i t - \delta\phi_i)} + \sigma_-^i e^{-i(\delta k \hat{X}_i - \mu_i t - \delta\phi_i)}) + d_i \sigma_z^i]. \quad (2)$$

The last term is an ac Stark shift of the  $i$ th spin by amount  $d_i$  and arises from differential ac Stark shifts between the two spin levels from the Raman beams. This shift includes the “two-photon” differential Stark-shift terms scaled by  $(g_1^2 + g_2^2)\omega_0/4\Delta^2$  and summed over each excited state detuned by  $\Delta$ , where  $\omega_0 \ll \Delta$ ; see Fig. 1. There are also “four-photon” Stark shifts scaled by  $\Omega_i^2/4\mu_i$  and summed over each two-photon Raman resonance detuned by  $\mu$ , where  $\Omega_i \ll \mu_i$ . The magnitude of these shifts depends greatly on the atomic energy level structure and light polarization; see [Lee \*et al.\* \(2016\)](#) for a discussion of Raman-coupled qubits (Fig. 1) and [Häffner \*et al.\* \(2003\)](#) for direct optically coupled qubits. These Stark shifts can be either absorbed into the definition of the spin energy levels or used as an effective axial magnetic field for simulations.

We assume here that the ions are confined to the Lamb-Dicke limit ([Wineland \*et al.\*, 1998](#); [Leibfried \*et al.\*, 2003](#)),

where the excursion of ion motion is much less than the associated wavelength of radiation driving transitions:  $\delta k \langle \hat{x}_i^2 \rangle^{1/2} \ll 1$ . This is typically a good assumption for trapped ions laser cooled to near their ground state, with a zero-point spatial spread of all modes  $\xi_m^{(0)}$  that is typically of the order of nanometers in experiments.

### 1. Effective magnetic fields

For a resonant ‘‘carrier’’ interaction ( $\mu = d_i = 0$ ) and under the rotating-wave approximation ( $\omega_m \gg \Omega_i$ ), the time dependence of  $\hat{X}$  averages to zero and the Hamiltonian of Eq. (2) is simply

$$H_B = \frac{1}{2} \sum_i \Omega_i \sigma_{\beta_i}^i, \quad (3)$$

where the transverse-field spin operator is defined by

$$\sigma_{\theta_i}^i \equiv \sigma_+^i e^{-i\theta_i} + \sigma_-^i e^{i\theta_i} = \sigma_x^i \cos \theta_i + \sigma_y^i \sin \theta_i. \quad (4)$$

This Hamiltonian of Eq. (3) describes the precession of spin  $i$  about an effective transverse magnetic field in the  $x$ - $y$  plane of the Bloch sphere at an angle

$$\beta_i = \delta\phi_i - \delta k \bar{X}_i \quad (5)$$

that can be controlled through the phase  $\delta\phi_i$ . In cases where  $\delta k \neq 0$ , the Rabi frequency acquires a dependence on the motion of the ions through Debye-Waller factors (Wineland *et al.*, 1998), but these are small in the Lamb-Dicke limit (Sørensen and Mølmer, 2000; Leibfried *et al.*, 2003).

Tuning the Raman laser beat note away from the carrier with  $\mu \gg \Omega_i$  generally results in a four-photon ac Stark shift of the previously discussed spin levels, given by the last term in Eq. (2) (Häffner *et al.*, 2003; Lee *et al.*, 2016). When each spin is exposed to a unique intensity of light and/or detuning of a single beam, parametrized by  $d_i$ , this gives rise to a site-dependent effective axial ( $z$ ) magnetic field.

### 2. Effective Ising interactions

When the frequency  $\mu_i$  is tuned to the neighborhood of the phonon modes  $\omega_m$ , the spin  $i$  is coupled to the ion motion through the spatial variation of the phase factor in Eq. (2). This generates an effective spin-spin interaction between the exposed ions, mediated by the collective transverse vibrations of the chain. For most simulation experiments, the transverse modes of motion are used to mediate the spin-spin interaction because their frequencies are tightly packed and all contribute

to the effective spin Hamiltonian, allowing control over the form and range of the interaction, described further later on. Transverse modes also oscillate at higher frequencies, leading to better cooling and less sensitivity to external heating and noise (Zhu, Monroe, and Duan, 2006).

In general, when non-copropagating laser beams form bichromatic beat notes at frequencies  $\omega_0 \pm \mu_i$  symmetrically detuned from the carrier with  $\mu_i \approx \omega_m$ , both upper and lower motion-induced sidebands of the normal modes of motion are driven in the ion crystal, giving rise to a spin-dependent force at frequency  $\mu_i$  (Solano, de Matos Filho, and Zagury, 1999; Sørensen and Mølmer, 1999; Milburn, Schneider, and James, 2000; Porras and Cirac, 2004). Owing to the symmetry of the detuned beat notes, the four-photon Stark shift is generally negligible. However, when the bichromatic beat notes are asymmetrically detuned from the carrier by  $\omega_0 + \mu_{i+}$  and  $\omega_0 - \mu_{i-}$ , the effective spin-dependent force occurs at frequency  $\mu_i = (\mu_{i+} + \mu_{i-})/2$  and the asymmetry provides a Stark shift that gives rise to an effective uniform axial magnetic field in Eq. (2) with  $d_i = (\mu_{i+} - \mu_{i-})/2$ .

Under the rotating-wave approximation ( $\omega_0 \gg \mu_i \gg \Omega_i$ ) with symmetric detuning  $\mu_i = \mu_{i+} = \mu_{i-}$  and within the Lamb-Dicke limit, the exponential function in Eq. (2) can be expanded to lowest order, resulting in (Zhu, Monroe, and Duan, 2006)

$$H(t) = \frac{1}{2} \sum_{i,m} \eta_{im} \Omega_i \sigma_{\theta_i}^i [a_m^\dagger e^{-i(\delta_{im}t + \psi_i)} + a_m e^{i(\delta_{im}t + \psi_i)}]. \quad (6)$$

Here the beat-note detuning on ion  $i$  from the  $m$ th motional sideband is defined as  $\delta_{im} = \mu_i - \omega_m$  and the Lamb-Dicke parameter  $\eta_{im} = b_{im} \delta k \xi_m^{(0)}$  describes the coupling between ion  $i$  and mode  $m$ .

Equation (6) includes two phases: a ‘‘spin phase’’  $\theta_i$  that determines the angle of the  $i$ th spin operator in the  $X$ - $Y$  plane of the Bloch sphere that diagonalizes the spin-dependent force, and a ‘‘motion phase’’  $\psi_i$  that determines the phase of the optical forces (but does not play a role in the spin-spin interactions developed later). These phases depend on the geometry of the bichromatic laser beams and there are two cases written in Eqs. (7) and (8) (Haljan *et al.*, 2005; Lee *et al.*, 2005). When the upper and lower sideband running wave beat notes propagate in the same direction ( $\delta k$  has the same sign for both), this is termed the ‘‘phase-sensitive’’ geometry. On the other hand, when the upper and lower sideband running waves propagate in opposite directions (opposite signs of  $\delta k$  for the two beat notes), this is called ‘‘phase insensitive.’’ The phases for each configuration are written

$$\begin{array}{cc} \text{spin phase} & \text{motion phase} \\ \text{Phase sensitive} & \theta_i = \left( \frac{\delta\phi_{i+} + \delta\phi_{i-}}{2} \right) - \delta k \bar{X}_i - \frac{\pi}{2}, \quad \psi_i = \left( \frac{\delta\phi_{i+} - \delta\phi_{i-}}{2} \right), \end{array} \quad (7)$$

$$\text{Phase insensitive} \quad \theta_i = \left( \frac{\delta\phi_{i+} + \delta\phi_{i-}}{2} \right), \quad \psi_i = \left( \frac{\delta\phi_{i+} - \delta\phi_{i-}}{2} \right) - \delta k \bar{X}_i - \frac{\pi}{2}. \quad (8)$$

Here  $\delta\phi_{i+}$  and  $\delta\phi_{i-}$  are the beat-note phases associated with the upper and lower sideband fields, respectively. The additional  $\pi/2$  phase factors compared with Eq. (5) originate from the imaginary linear term in the Lamb-Dicke expansion of  $e^{ik\hat{x}_i}$ .

The sensitivity of the spin phase to  $\delta k \bar{X}_i$  has great importance in the practical implementation of spin-spin Hamiltonians. In the phase-sensitive geometry, this dependence may be desired when the phase of other Hamiltonian terms [such as the carrier spin-flip operation of Eq. (3)] have the same form, as in Eq. (5). This allows a phase-sensitive diagnosis of individual spin operations. However, sensitivity to  $\delta k \bar{X}_i$  over sufficiently long times can lead to decoherence if there are drifts in the relative path length of non-copropagating beams or the ion chain position along the  $X$  direction. The phase-insensitive configuration is therefore useful for long simulation evolution times.

We note that the phase-insensitive geometry using Raman couplings [Fig. 1(b)] can remove the spin-phase sensitivity to not only the absolute optical phase of the optical source but also the relative optical path length difference between the counterpropagating beams by setting  $\delta\phi_{i+} = -\delta\phi_{i-}$  (Haljan *et al.*, 2005; Lee *et al.*, 2005). This is not possible with direct optical upper and lower sideband transitions on spins with an optical energy splitting, as their optical phases add regardless of the geometry.

For either phase configuration, the evolution operator under this Hamiltonian can be written from the Magnus expansion, which terminates after the first two terms (Zhu, Monroe, and Duan, 2006)

$$U(\tau) = \exp \left[ -i \int_0^\tau dt H(t) - \frac{1}{2} \int_0^\tau dt_1 \int_0^{t_1} dt_2 [H(t_1), H(t_2)] \right] \quad (9)$$

$$= \exp \left[ \sum_i \hat{\zeta}_i(\tau) \sigma_{\theta_i}^i - i \sum_{i < j} \chi_{i,j}(\tau) \sigma_{\theta_i}^i \sigma_{\theta_j}^j \right]. \quad (10)$$

The first term of Eq. (10) is a spin-phonon coupling with the operator

$$\hat{\zeta}_i(\tau) = \sum_m [\alpha_{i,m}(\tau) a_m^\dagger - \alpha_{i,m}^*(\tau) a_m], \quad (11)$$

representing the spin-dependent coherent displacements (Glauber, 1963; Leibfried *et al.*, 2003) of the  $m$ th motional mode through phase space by an amount

$$\begin{aligned} \alpha_{i,m}(\tau) &= -\frac{i}{2} \eta_{im} \Omega_i \int_0^\tau dt e^{-i(\delta_{im}t + \psi_i)} \\ &= -\frac{\eta_{im} \Omega_i e^{-i\psi_i}}{2\delta_{im}} (1 - e^{-i\delta_{im}\tau}). \end{aligned} \quad (12)$$

The second term of Eq. (10) is the key result: a spin-spin interaction between ions  $i$  and  $j$  with coupling strength

$$\chi_{i,j}(\tau) = \frac{1}{2} \Omega_i \Omega_j \sum_m \eta_{im} \eta_{jm} \int_0^\tau dt_1 \int_0^{t_1} dt_2 \sin(\delta_{im}t_1 - \delta_{jm}t_2) \quad (13)$$

$$= \Omega_i \Omega_j \sum_m \frac{\eta_{im} \eta_{j,m}}{2\delta_{im} \delta_{jm}} \left[ \left( \frac{\delta_{im} + \delta_{jm}}{2} \right) \tau - \left( \frac{\sin \delta_{im}\tau + \sin \delta_{jm}\tau}{2} \right) \right] \quad (14)$$

$$= \Omega_i \Omega_j \sum_m \frac{\eta_{im} \eta_{j,m}}{2\delta_m} \left( \tau - \frac{\sin \delta_m \tau}{\delta_m} \right) \quad \text{for } \delta_{im} = \delta_{jm}. \quad (15)$$

Fractional corrections to this expression arising from higher-order terms in the Lamb-Dicke expansion leading to Eq. (6) can be shown to be of the order of  $\eta_{im}^2 \eta_{j,m}^2 \bar{n}_m^2$  for each mode (Sørensen and Mølmer, 2000), where  $\bar{n}_m$  is the average number of vibrational quanta in mode  $m$ . In this review, we generally consider global spin Hamiltonians that are realized by exposing all the ions to the spin-dependent force. However, for the special case of applying a spin-dependent force to just two ions  $i$  and  $j$  in the chain, which is common for the execution of entangling two-qubit quantum logic gates (Sørensen and Mølmer, 1999, 2000), the evolution operator in Eq. (10) reduces to

$$U_{ij}(\tau) = e^{-i\chi_{ij}(\tau)} |\uparrow_{\theta_i} \uparrow_{\theta_j}\rangle \langle \uparrow_{\theta_i} \uparrow_{\theta_j}| \prod_m \hat{D}_m[\alpha_{im}(\tau) + \alpha_{jm}(\tau)] \quad (16)$$

$$+ e^{-i\chi_{ij}(\tau)} |\downarrow_{\theta_i} \downarrow_{\theta_j}\rangle \langle \downarrow_{\theta_i} \downarrow_{\theta_j}| \prod_m \hat{D}_m[-\alpha_{im}(\tau) - \alpha_{jm}(\tau)] \quad (17)$$

$$+ e^{i\chi_{ij}(\tau)} |\uparrow_{\theta_i} \downarrow_{\theta_j}\rangle \langle \uparrow_{\theta_i} \downarrow_{\theta_j}| \prod_m \hat{D}_m[\alpha_{im}(\tau) - \alpha_{jm}(\tau)] \quad (18)$$

$$+ e^{i\chi_{ij}(\tau)} |\downarrow_{\theta_i} \uparrow_{\theta_j}\rangle \langle \downarrow_{\theta_i} \uparrow_{\theta_j}| \prod_m \hat{D}_m[-\alpha_{im}(\tau) + \alpha_{jm}(\tau)]. \quad (19)$$

In this expression, the spin projection operators are eigenvectors of  $\sigma_{\theta_i}$ :  $|\uparrow_{\theta_i}\rangle = (|\uparrow_i\rangle + e^{-i\theta_i} |\downarrow_i\rangle)/\sqrt{2}$ ,  $|\downarrow_{\theta_i}\rangle = (|\uparrow_i\rangle - e^{-i\theta_i} |\downarrow_i\rangle)/\sqrt{2}$  and  $\langle \uparrow_{\theta_i} | \sigma_{\theta_i} | \uparrow_{\theta_i} \rangle = +1$ ,  $\langle \downarrow_{\theta_i} | \sigma_{\theta_i} | \downarrow_{\theta_i} \rangle = -1$ . The coherent displacement operator on mode  $m$  is  $\hat{D}_m(\alpha) = e^{\alpha a_m^\dagger - \alpha^* a_m}$  (Glauber, 1963).



There are two regimes where the collective modes of motion contribute to the spin-spin coupling, taking evolution time  $\tau$  to be much longer than the ion normal mode oscillation periods ( $\omega_m \tau \gg 1$ ). In the “resonant” regime (Solano, de Matos Filho, and Zagury, 1999; Milburn, Schneider, and James, 2000; Sørensen and Mølmer, 2000), the optical beat-note detuning  $\mu$  is close to 1 or more normal modes and the spins become entangled with the motion through the spin-dependent displacements. However, at certain times of the evolution  $\alpha_{i,m}(\tau) \approx 0$  for all modes  $m$  and the motion nearly decouples from the spin states, which is useful for applying synchronous entangling quantum logic gates between the spins. For closely spaced modes such as the transverse modes seen in Fig. 3, resolving individual modes becomes difficult and may require laser-pulse-shaping techniques (Zhu, Monroe, and Duan, 2006). For generating pure spin Hamiltonians, we instead operate in the “dispersive” regime (Sørensen and Mølmer, 1999; Porras and Cirac, 2004), where the optical beat-note frequency is far from each normal mode relative to that mode’s sideband Rabi frequency ( $|\delta_{im}| \gg \eta_{im}\Omega_i$ ). In this case, the phonons are only virtually excited as the displacements become negligible [ $|\alpha_{i,m}(t)| \ll 1$ ]. The spin-phonon part of the evolution [Eq. (11)] is therefore negligible, and the spin-spin interaction evolution [Eq. (10)] is dominated by the secular terms of Eqs. (14) and (15) that are linear in time  $\tau$ . The final result is an effective fully connected Ising Hamiltonian

$$H_{J_\theta} = \sum_{i < j} J_{ij} \sigma_{\theta_i}^i \sigma_{\theta_j}^j, \quad (20)$$

where the Ising matrix is given by

$$J_{ij} = \Omega_i \Omega_j \omega_{\text{rec}} \sum_m \frac{b_{im} b_{jm}}{4\omega_m} \left( \frac{1}{\delta_{im}} + \frac{1}{\delta_{jm}} \right) \quad (21)$$

$$= \Omega_i \Omega_j \omega_{\text{rec}} \sum_m \frac{b_{im} b_{jm}}{2\omega_m \delta_m} \quad \text{for } \delta_{im} = \delta_m. \quad (22)$$

Here we use  $\omega_{\text{rec}} = \hbar(\delta k)^2/2M$  as the recoil frequency associated with the transfer of momentum  $\hbar(\delta k)$  to a single ion.

Substituting the exact values for the normal mode matrix  $b_{im}$  and assuming that the optical force is detuned at frequencies higher than all phonon modes ( $\delta_m > 0$ ), we find that for a uniform Rabi frequency over the ions  $\Omega_i = \Omega$  the Ising matrix is well approximated by a long-range antiferromagnetic (AFM) coupling that fall off as an inverse power law with distance

$$J_{ij} = \frac{J_0}{|i-j|^\alpha}, \quad (23)$$

with the nearest-neighbor Ising coupling  $J_0$ . The exponent  $\alpha$  that determines the range of the Ising interaction can be set to  $0 < \alpha < 3$  by simply adjusting the laser detuning  $\mu > \omega_m$  (Porras and Cirac, 2004; Islam *et al.*, 2011). The true asymptotic long-chain behavior of a trapped-ion chain is more subtle (Nevado and Porras, 2016), but the power-law approximation is good, as shown in Fig. 4, comparing numerically exact couplings with best-fit power laws for various detunings in both a linear and a 2D crystal.

When the detuning  $\mu$  is tuned between the modes of motion, many other patterns of the Ising graph can be realized (Lin, Monroe, and Duan, 2011; Korenblit *et al.*, 2012). The spin-spin interaction profile  $J_{ij}$  can in principle be programmed arbitrarily with sufficient control of the individual spin-phonon couplings on  $N$  trapped ions. For example,  $N$  unique bichromatic Raman beat notes applied at frequencies  $\omega_0 \pm \mu_n$ , with  $\mu_n \approx \omega_n$  ( $n = 1, 2, \dots, N$ ), can be used with local intensity control over each ion to create an arbitrary interaction graph

$$J_{ij} = \sum_n \Omega_{i,n} \Omega_{j,n} \omega_{\text{rec}} \sum_m \frac{b_{im} b_{jm}}{2\omega_m (\mu_n - \omega_m)}. \quad (24)$$

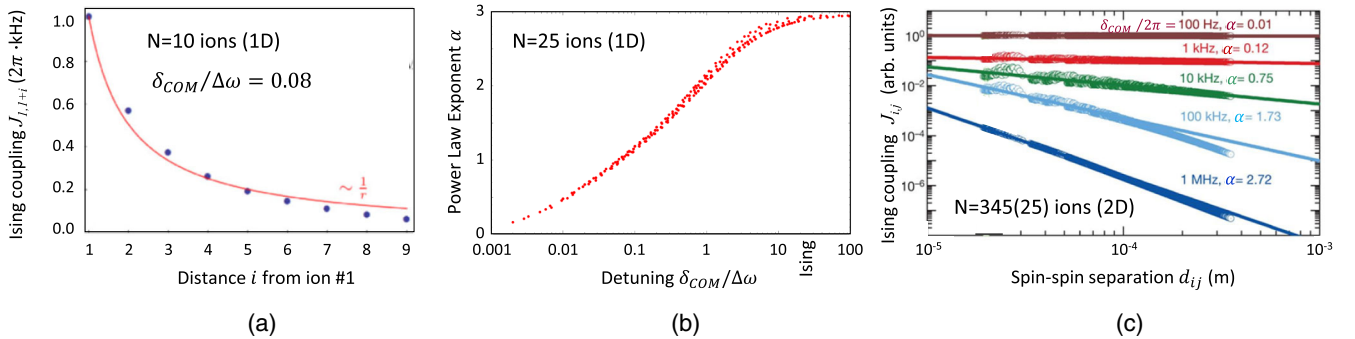


FIG. 4. Theoretical comparison of exact Ising couplings to the inverse power-law form of Eq. (23). (a) Calculated Ising couplings to edge ion in a 1D crystal of ten ions confined with a harmonic external axial potential. The Raman detuning from the c.m. mode, scaled to the bandwidth  $\Delta\omega$  of the transverse modes, is  $\delta_{c.m.}/\Delta\omega$ , with the best-fit power law (line) of  $\alpha = 1$ . Adapted from Islam, 2012. (b) Best-fit inverse power-law exponent  $\alpha$  for calculated Ising couplings within a 1D crystal of 25 ions with harmonic axial confinement, plotted as a function of the Raman detuning from the c.m. mode  $\delta_{c.m.}/\Delta\omega$ . The spread of the points at a given detuning considers various bandwidths  $\Delta\omega$  (axial c.m. confinement frequencies ranging from 100 to 350 kHz with a transverse c.m. confinement frequency of 5 MHz), and the c.m. sideband Rabi frequency  $\eta_{i,c.m.}\Omega$  is always less than 1/3 of the detuning  $\delta_{c.m.}$  in order to limit direct phonon excitation. Adapted from Islam, 2012. (c) Calculated Ising couplings from Eq. (22) in a 2D crystal of 217 ions vs a sampling of the distance  $d_{ij}$  between ion pairs (circles). The lines are best-fit power-law exponents  $\alpha$  (lines) for various detunings from the c.m. mode of 795 kHz. Adapted from Britton *et al.*, 2012.

Here  $\Omega_{i,n}$  is the Rabi frequency corresponding to the  $n$ th beat note on the  $i$ th ion. Note that  $J_{ij}$  is nonlinear under the  $\mathcal{O}(N^2)$  experimental control parameters  $\Omega_{i,n}$  and  $\mu_n$ , and hence tuning the quantum simulator requires nonlinear optimization methods (Korenblit *et al.*, 2012; Teoh *et al.*, 2020). Alternative approaches to realizing a target interaction graph without tuning the full Rabi frequency matrix  $\Omega_{i,n}$  include modifying a global Mølmer-Sørensen coupling profile [such as Eq. (23)] by local spatial control of spins in hybrid analog-digital ways (Hayes, Flammia, and Biercuk, 2014; Rajabi *et al.*, 2019).

This review mainly considers Ising interactions in the slow dispersive regime in order to engineer the pure spin Hamiltonians given by Eqs. (3) and (20) that do not directly involve the bosonic phonon operators. An important class of models in quantum magnetism that appear throughout this review is the transverse-field Ising model, which is one of the simplest physical models that admits a quantum phase transition (Sachdev, 2011) owing to its noncommuting spin operators

$$H_{TI} = \sum_{i<j} J_{ij} \sigma_x^i \sigma_x^j + B_y \sum_i \sigma_y^i. \quad (25)$$

In ion-trap systems, this model can be generated with a combination of the effective magnetic field in Eq. (3) and the Ising interactions in Eq. (20) with appropriate settings of the spin phases  $\theta_i$  in Eqs. (5), (7), and (8). When both non-commuting terms are simultaneously applied, additional spin-dependent ( $\sigma_z^i$ ) phonon terms appear in higher orders of the Magnus expansion of Eq. (9) (Wang and Freericks, 2010, 2012), which is discussed in Sec. II.A. It is often desired to implement interacting spin models with multiple components of Ising interactions along various axes of the Bloch sphere, with the most general being the anisotropic Heisenberg model involving a sum of all three Ising terms

$$H_{\text{Heis}} = J_{ij}^x \sigma_x^i \sigma_x^j + J_{ij}^y \sigma_y^i \sigma_y^j + J_{ij}^z \sigma_z^i \sigma_z^j. \quad (26)$$

Subclasses of the Heisenberg model arise naturally in physics and can possess useful symmetries (Sachdev, 2011). For example, the isotropic Heisenberg model ( $J_{ij}^x = J_{ij}^y = J_{ij}^z$ ) is relevant to natural 3D magnetic interactions. The  $XXZ$  model ( $J_{ij}^x = J_{ij}^y$ ) and the  $XY$  model ( $J_{ij}^x = J_{ij}^y$ ;  $J_{ij}^z = 0$ ) result from standard transformations of fermionic Hubbard models to spin models (Jordan and Wigner, 1928; Bravyi and Kitaev, 2002), which is discussed in Sec. V. The  $XXZ$  and  $XY$  models also conserve the  $z$  component of the total spin in the system, allowing simplifications to the spin dynamics and the interpretation of measurements.

Ion-trap quantum simulators can generate generic Heisenberg models with the previously discussed primitive of the Ising interaction using a variety of extensions. First, the three separate Ising terms in the Hamiltonian can exploit three independent modes (or spatial directions) of motion (Porrás and Cirac, 2004), although this may not easily produce the same form or range of Ising interactions for all three axes. Second, the desired interactions can be applied sequentially in a Trotter expansion of the desired Hamiltonian (Trotter, 1959; Suzuki, 1985; Lloyd, 1996; Lanyon *et al.*, 2011; Johri,

Steiger, and Troyer, 2017), as discussed in Sec. V. Third, a transverse-field Ising model [Eq. (25)] can be applied with  $B_y \gg J_{ij}$ , so the field overwhelms the Ising interactions. This can be seen by expanding the Ising term as  $\sigma_x^i \sigma_x^j = (\sigma_+^i + \sigma_-^i)(\sigma_+^j + \sigma_-^j) \approx \sigma_+^i \sigma_-^j + \sigma_-^i \sigma_+^j = \sigma_x^i \sigma_x^j + \sigma_y^i \sigma_y^j$ . Here the strong field energetically forbids double spin flips or, equivalently, bestows fast oscillations to the  $\sigma_\pm^i \sigma_\pm^j$  terms, which average to zero in an effective rotating-wave approximation (Cohen *et al.*, 2015).

## II. SPIN HAMILTONIAN BENCHMARKING AND MANY-BODY SPECTROSCOPY

A compelling Hamiltonian quantum simulation usually results in some type of nontrivial ground state or dynamics that may elude classical computation. It is therefore important to verify that the desired Hamiltonian is indeed being correctly implemented by the quantum simulator (Cirac and Zoller, 2012; Hangleiter *et al.*, 2017). For systems that are small enough and tractable for a direct comparison between the simulator's results and a theoretical calculation, this provides some confidence that the proper simulation has been run. But scaling up the system can introduce additional imperfections that may call into question the accuracy of the applied Hamiltonian.

Two approaches for verifying quantum simulators beyond classically computability are the use of fault-tolerant techniques in the expression of the simulation in terms of discrete error-corrected gates (Gottesman, 1998; Preskill, 1998), and the comparison of the results of multiple quantum simulators built upon different platforms (Leibfried, 2010). Though this list is not comprehensive [see Hangleiter *et al.* (2017)], we now examine these two approaches.

Universal Hamiltonian digital quantum simulators (DQSs) as discussed in Sec. V break up the simulation evolution into a series of time steps, and the error  $\epsilon$  introduced by this ‘‘Trotter’’ expansion is bounded and inversely proportional to the number of steps  $M$  (Lloyd, 1996). This approach was notably employed for the implementation of various Hamiltonians, including many-body magnetic couplings, in a system of trapped ions (Lanyon *et al.*, 2011). Because DQSs rely on discrete quantum gate sets, one possibility for its verification is that this can in principle be accomplished through fault-tolerant error correction on the gates (Terhal, 2015). This increases the number of operations required, and it has been shown that the run-time can scale exponentially with the desired precision of the parameter being computed, in which case the resource cost for a fault-tolerant DQS for parameter estimation is similar to that of universal quantum computing (Brown, Clark, and Chuang, 2006; Clark *et al.*, 2009). Further, simulations with systems that lack universal gate sets or the digital simulation of open systems may render fault tolerance unavailable in a DQS (Hauke *et al.*, 2012). Since the cost of introducing currently known methods for fault tolerance is too high for precision DQSs (Kendon, Nemoto, and Munro, 2010), other methods for verifying non-fault-tolerant DQSs are needed.

Another way that one might test quantum simulators is to compare the results of two simulations. This could involve

comparing the results of simulations performed on different platforms (Leibfried, 2010), or even comparing the results obtained by using different simulation methods on the same machine. A variation on this second theme is to run a Hamiltonian simulation forward and then backward in time (Cirac and Zoller, 2012), which may reveal flaws that are not undone by the time reversal, such as dissipation. An initial experiment demonstrated this time-reversal technique for a trapped-ion quantum simulation by adiabatically ramping from an initial state of high magnetization along  $y$ , through a phase transition, and then back again (Islam *et al.*, 2013). Measurements of the magnetization at all three extrema in this time sequence revealed a revival in the magnetization, achieving an average of  $\langle S_y \rangle = 68(4)\%$  of the initial value, in agreement with closed-system numerical integration.

Recently a variational eigensolver approach was combined with an ion-trap quantum simulator to perform a VQS of the lattice Schwinger model that combines some ways to verify some features of the result (Kokail *et al.*, 2019). The VQS uses feedback with a classical computer that translates measurement results from the AQS into expectation values of a software Hamiltonian to find energy eigenstates of the underlying Hamiltonian. Since the conversion between the measurement and its interpretation happens in classical software, it provides a way to perform some verification of the resulting states because both the eigenvalues and their variances are accessible. For instance, the VQS demonstrated by Kokail *et al.* (2019) measured the expectation value of the simulated Hamiltonian  $E = \langle H \rangle$ , as well as the expectation value of  $(H - E)^2$ , which should be zero if the state is an energy eigenstate of  $H$  with eigenvalue  $E$ . While this does not guarantee that the state found by the VQS is the ground state, this verification can be used to assess the confidence in the state being an eigenstate.

### A. Sources of error

Quantum simulations with trapped ions can be susceptible to unwanted interactions that lead to inaccuracies in the simulation. Many such error sources are common to both simulations and trapped-ion quantum computing gates, such as spontaneous emission from the lasers driving spin transitions, and have been examined in detail elsewhere (Wineland *et al.*, 1998; Ozeri *et al.*, 2007). Further, the simulation protocol itself may have known approximations (such as the Trotterization errors and nonadiabatic evolution) that may be rigorously bounded, though their effects may not be fully understood.

The inclusion of a transverse effective magnetic field to the spin-dependent force of Eq. (6) includes higher-order terms beyond the simple transverse Ising model of Eq. (25) (Wang and Freericks, 2012). These additional terms can create substantial spin-motion entanglement that can affect measurements in bases other than the Ising direction. For transverse-field strengths that exceed the Ising coupling, the system begins to attain the character of an  $XY$  model with both  $\sigma_x^i \sigma_x^j$  and  $\sigma_y^i \sigma_y^j$  couplings, and the strong-field Ising model can break down. The spins in this case do not strictly decouple from the phonons at any point in time, but it has been shown that they

can typically be made small for experimentally accessible timescales (Wall, Safavi-Naini, and Rey, 2017).

Protocols that rely on adiabatic ramping through a small gap can be susceptible to the breakdown of the adiabatic approximation in the region where the gap is small. As we discuss later, for a linear ramp of  $B(t)$  through a system energy gap of size  $\Delta$ , the adiabaticity criterion is approximately  $|\dot{B}_y/\Delta^2| \ll 1$ . For cases where the gaps are known, the ramp rate can be adaptively matched to the gap to maximize adiabaticity, a technique known as local adiabatic evolution (Roland and Cerf, 2002). However, since repeated experiments can be used to gather statistics about the final state, it has been shown that significant nonadiabaticity can be present and still allow the ground-state spin configuration to be found due to its statistical prevalence (Richerme, Senko, Smith *et al.*, 2013).

State preparation and measurement (SPAM) errors, which are to some degree common to simulators and gate-based quantum computers, are another source of errors in lattice spin simulators. Given an uncorrelated, single-shot, single ion SPAM fidelity  $\mathcal{F}$ , the probability of a single SPAM error is  $1 - \mathcal{F}^N$ . The current state-of-the-art SPAM fidelity for single qubits is  $\mathcal{F} = 0.99971(3)$ , which produces one error on average for single-shot projective measurements of a register with  $N \geq \ln 2/(1 - \mathcal{F}) \approx 2400$  qubits (Christensen *et al.*, 2020). In certain special cases, repeated experiments can be used to mitigate this error through statistical methods (Shen and Duan, 2012). Cross talk between neighboring ions can also lead to measurement errors, and the ion positions must be calibrated to define a region of interest on the camera for each ion's fluorescence detection. State detection infidelity from neighboring ions is typically no more than a few percent per qubit (Zhang *et al.*, 2017), although this error can be suppressed to well below 1% (Cetina *et al.*, 2020) and can be made even smaller with ion shuttling (Kielbinski, Monroe, and Wineland, 2002).

There are various sources of decoherence quantum simulations in the trapped-ion platform, such as stray magnetic and electric fields, mode frequency drifts, off-resonant motional excitation, and spontaneous emission. While these errors have been analyzed in the context of quantum computing (Wineland *et al.*, 1998), decoherence can set a practical time limit for quantum simulations that may lead to other errors, such as diabatic errors. Since many of these error sources increase with system size, it may be necessary to employ methods of mitigation such as magnetic field shielding (Ruster *et al.*, 2016).

Off-resonant excitation to motional modes is nominally already considered in the spin-motional coupling described by Eq. (12). The probability of motion-induced spin-flip errors in a chain of  $N$  ions can be estimated by  $\epsilon = \sum_{i,m}^N |\alpha_{i,m}|^2$ , summing over all modes. By neglecting the time dependence and assuming equally contributing modes, this error is expected to scale as  $\epsilon \sim N(\eta\Omega/\delta)^2$ , where  $\delta$  is the smallest detuning from any mode. This same approximation was made in the derivation of Eq. (22), leading to the scaling  $J_{ij} \sim (\eta\Omega)^2/\delta$ . Motion-induced spin-flip errors can therefore be mitigated by increasing both  $\delta$  [Eq. (6)] and the Raman Rabi frequency  $\Omega = g_1 g_2 / 2\Delta$  to keep the same spin-spin

interaction. However, increasing the Rabi frequency may increase spontaneous emission errors, which grow linearly with Rabi frequency for large detuning as  $\Gamma = \gamma\Omega/4\Delta$ , where the atomic linewidth  $\gamma$  is defined in Sec. I.A and  $\Delta \gg \gamma$  is assumed. Given a level of motion-induced spin-flip error  $\varepsilon$ , it can be shown that the spontaneous emission error during the interaction time  $t_{J_0} = 2\pi/J_0$  scales as  $\sqrt{N/\varepsilon}$  (Kim *et al.*, 2010).

## B. Benchmarking Ising couplings

For the Ising spin models considered in this review, it is important to validate the strength of the Ising-coupling matrix  $J_{ij}$  of Eqs. (20)–(22) and effective magnetic fields in Eq. (3). For small numbers of spins, it is possible to directly extract the Ising couplings and fields by preparing the spins in a  $\sigma_z$  eigenstate and subjecting them to the  $\sigma_\theta$  Ising interactions or field terms. The resulting oscillations in population are given by the energies of the occupied states, so performing a Fourier transform on these oscillations directly provides the energy differences.

An example of directly measured Ising oscillations and their resulting Fourier transform is shown in Figs. 5(a) and 5(b) for  $N = 3$  spins. The extracted interaction strengths are shown in Fig. 5(c). This technique is effective in the context of both continuous (Kim *et al.*, 2011) and digital (Lanyon *et al.*, 2011) simulations of Ising models. A similar method has been used to extract the strengths of magnetically induced spin-spin couplings (Khromova *et al.*, 2012; Piltz *et al.*, 2016). Neither technique scales well to more than a few spins owing to the difficulty in extracting many closely spaced frequencies in the spin oscillations.

Individual Ising couplings within a given spin chain can be measured using an auxiliary state of the ions, even for large numbers of spins. Because the Ising couplings depend on the

vibrational mode spectrum, all ions must be physically present in the trap to obtain a meaningful result, but the spectrum of the population oscillations illustrated in Fig. 5 are difficult to obtain if all spins participate in the many-body dynamics. An alternative approach is to perform a separate measurement for each individual Ising coupling by “hiding” all ions except the pair of interest into an auxiliary internal state that does not experience the spin-dependent force giving rise to Ising couplings. In this manner, the frequency with which the ions of interest  $i$  and  $j$  oscillate between correlated states  $|00\rangle$  and  $|11\rangle$  allows for the determination of the Ising matrix  $J_{ij}$  (Jurcevic *et al.*, 2014). For large collections of spins with long-range interactions, benchmarking of weak Ising interactions can be accomplished by measuring the global precession of the spins. Here the spins are each prepared in an identical state that is tipped away from the Bloch sphere axis of the Ising interaction and the resulting dynamics of the global Ising interaction can be recorded. Figure 6 shows measurements of this type of benchmarking in a collection of more than 200 trapped-ion spins (Britton *et al.*, 2012), which agrees well with mean-field theory. For sufficiently strong Ising interactions, as shown in this experiment, the mean-field approximation breaks down, indicating the entanglement between the spins.

Other spectroscopic techniques for probing the energy spectrum of the bare Ising Hamiltonian are also possible (Senko *et al.*, 2014). For instance, in the transverse Ising model of Eq. (25), modulating the effective field  $B_y(t)$  at a frequency commensurate with an energy difference in the full spin Hamiltonian will drive transitions between the two differing states. Specifically, taking  $B_y(t) = B_0 + B_p \sin(\omega_{\text{mod}}t)$  with  $B_p \ll J$ , the frequency  $\omega_{\text{mod}}$  at which such transitions occur is directly related to the Ising couplings  $J_{ij}$  (Senko *et al.*, 2014). Figures 7(a) and 7(b) illustrate examples where the Ising

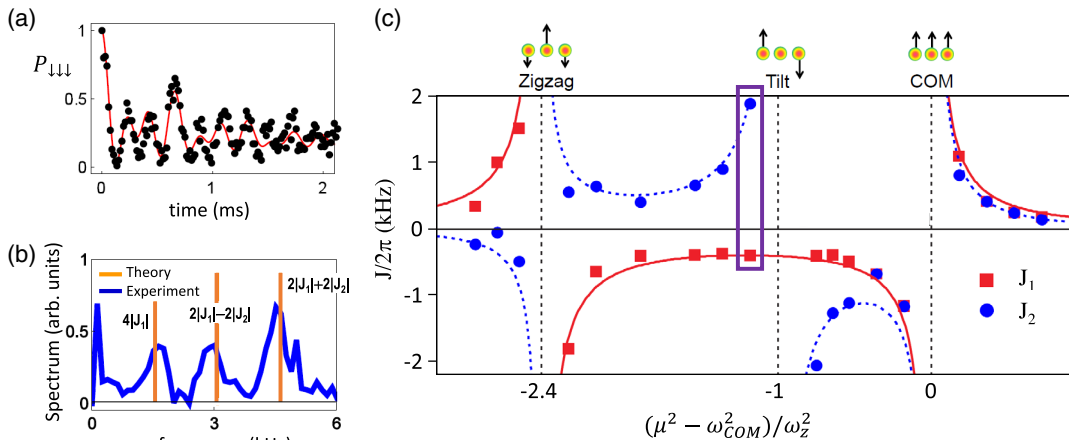


FIG. 5. Direct measurement of Ising nearest-neighbor ( $J_1$ ) and next-nearest-neighbor ( $J_2$ ) interactions for  $N = 3$  trapped-ion spins. (a) Measured time evolution of the probability of state  $|\downarrow\downarrow\downarrow\rangle$  subject to global Ising interactions, with the spins initialized in the state  $|\downarrow\downarrow\rangle|\downarrow\downarrow\rangle|\downarrow\downarrow\rangle$ . The solid line is a fit to theory with an empirical exponential decay. (b) The Fourier spectrum of the oscillations in (a) exposes the frequency splittings of the Ising Hamiltonian. (c) Extracted Ising couplings  $J_1$  and  $J_2$  from the Fourier spectra as a function of the applied beat-note detuning  $\mu$ , scaled so that the c.m., tilt, and zigzag modes of transverse motion occur at  $(\mu^2 - \omega_{\text{c.m.}}^2)/\omega_z^2 = 0, -1,$  and  $-2.4$ , respectively. The squares ( $J_1$ ) and circles ( $J_2$ ) are experimentally measured couplings, and the lines are calculated from Eq. (22) with no free fit parameters. The particular measurements in (a) and (b) correspond to the scaled laser beat-note detuning  $(\mu^2 - \omega_{\text{c.m.}}^2)/\omega_z^2 = -1.2$  indicated by the points highlighted by the rectangle in (c). Adapted from Kim *et al.*, 2009.

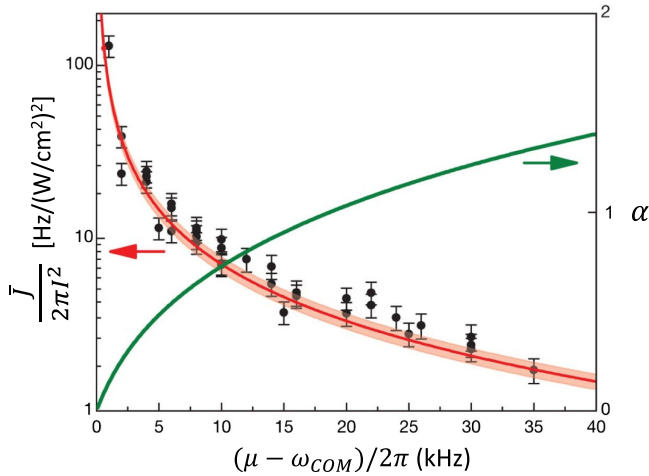


FIG. 6. Mean-field benchmarking of Ising couplings in a 2D crystal of 206(10) ions confined in a Penning trap. The spins are all initialized in a separable product state slightly tipped from the axis of a subsequently applied (weak) long-range Ising interaction. The resulting global spin precession of the ions is measured as a function of the detuning of the optical dipole force laser beams from the axial c.m. mode; see Sec. I and Fig. 3(b). Each point is generated by measuring the mean Ising coupling at a particular laser beam intensity  $I$ . The solid decaying line is the prediction of mean-field theory that accounts for couplings to all  $N$  transverse modes, with no free parameters. The line's breadth reflects experimental uncertainty in the initial tipping angle of the spins. The mean-field prediction for the average value of the power-law exponent  $\alpha$  from Eq. (23) is indicated by the expanding solid line (right axis, linear scale). For stronger Ising interactions, the mean-field approach breaks down. Adapted from Britton *et al.*, 2012.

matrix is directly measured using this technique to confirm the validity of the power-law approximation described in Eq. (23) for a handful of spins. The technique of applying a small oscillating term can be generalized to other cases such as measurement of the critical minimum gap between the ground and first excited states of the transverse-field Ising model, as shown in Fig. 7(c).

### III. EQUILIBRIUM STUDIES

Finding ground states of a nontrivial Hamiltonian is important in various disciplines across condensed matter physics, quantum chemistry, and computer science. In condensed matter physics, the rich phenomenon of complex quantum systems can be understood by finding the ground states of the corresponding many-body Hamiltonian (Kohn, 1999; Foulkes *et al.*, 2001; Schollwöck, 2005). In quantum chemistry and molecular physics, the central problem is to determine the electronic structure and the ground-state energy of atoms and molecules (Jensen, 1989). In computer science, the ground state of the complex quantum Hamiltonian can encode other computational problems such as satisfiability and optimization (Kolsgaard *et al.*, 2001; Lloyd, 2008; Albash and Lidar, 2018).

The computational tasks of finding the ground state of nontrivial Hamiltonians are classically demanding because of the exponentially increasing Hilbert space of the Hamiltonian. A quantum simulator is expected to provide a solution beyond the limitations of classical computation. Recently various theoretical schemes for the ground-state problem have been proposed and proof-of-principle experimental demonstrations

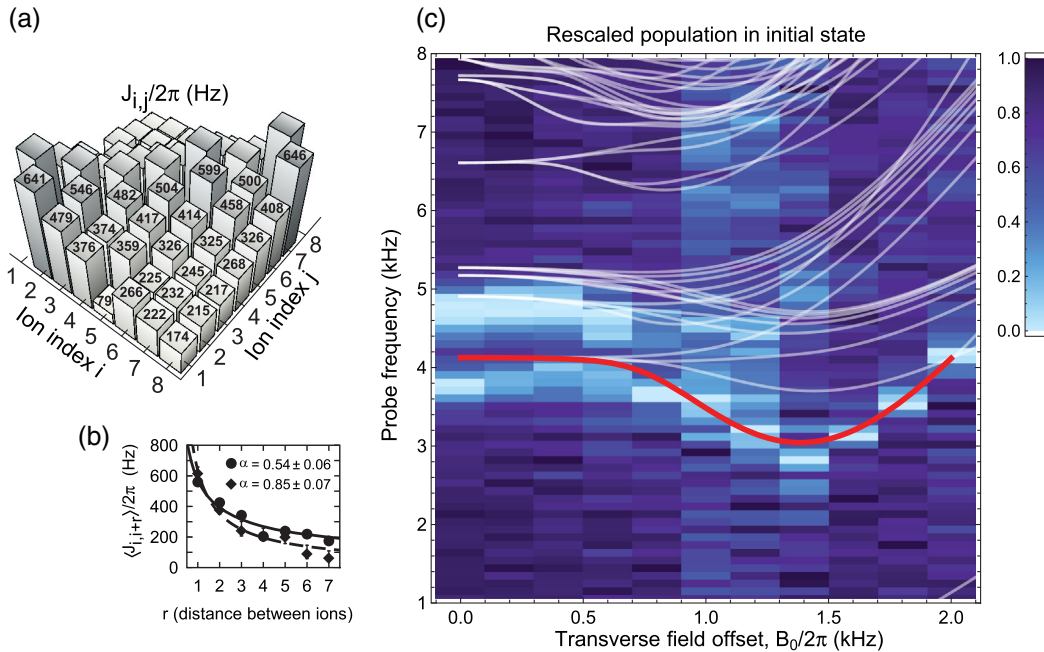


FIG. 7. (a) All elements of an Ising-coupling matrix measured with a spectroscopic probe in the form of a modulated transverse field. (b) Measurements of two sets of Ising-coupling matrices demonstrating two different effective interaction ranges across the chain, with the solid lines the best fits to inverse power-law form expected in Eq. (23). (c) Rescaled populations in the approximate ground state vs a static transverse-field offset  $B_0$  and the modulation frequency of a small additional transverse field. Calculated energy levels based on measurements of trap and laser parameters are overlaid as thin white lines, and the lowest coupled excited state is overlaid as the thick lowest line, showing the critical gap near  $B_0/2\pi = 1.4$  kHz. The energy of the ground state is always taken to be zero. From Senko *et al.*, 2014.

have been performed, including adiabatic preparation (Friedenauer *et al.*, 2008; Edwards *et al.*, 2010; Kim *et al.*, 2010, 2011; Islam *et al.*, 2011, 2013; Richerme, Senko, Korenblit *et al.*, 2013), direct cooling by bath engineering (Barreiro *et al.*, 2011; Lin *et al.*, 2013), and algorithmic cooling schemes (Baugh *et al.*, 2005; Xu *et al.*, 2014; Zhang *et al.*, 2020). In the case of the adiabatic method, it has been shown to be closely related to adiabatic quantum computation, which has proven to be equivalent to a universal quantum computer (Albash and Lidar, 2018).

We focus on the adiabatic preparation of the ground state of quantum spin models with trapped atomic ion spins, including a description of the general scheme of the experimental procedure and various adiabatic ramping protocols. Following a discussion of the adiabatic protocol applied to varying numbers of trapped-ion spins, we consider how this protocol can be optimized and applied to broader classes of spin models and discuss the case of a spin-1 system. These quantum spin models show the essences of the adiabatic quantum simulation with wide applications. Moreover, these quantum spin models can describe a large class of many-body quantum physics in condensed matter such as quantum magnetism (Moessner and Ramirez, 2006), spin glasses (Binder and Young, 1986), and spin liquids (Balents, 2010). The solutions of certain spin Hamiltonians are also connected to many other computational problems, including optimization problems, when the system is extended to two dimensions (Albash and Lidar, 2018).

### A. Adiabatic ground-state preparation

Adiabatic ground-state preparation is analogous to that of adiabatic quantum computation (Farhi *et al.*, 2000; Albash and Lidar, 2018): a quantum system is initialized to the ground state of a trivial Hamiltonian  $H_{\text{triv}}$ . Next the Hamiltonian is adiabatically deformed into the Hamiltonian of interest  $H_{\text{prob}}$ , whose ground state encodes the solution of a problem that has been mapped to this final Hamiltonian. The adiabatic evolution is generated by

$$H(s) = (1 - s)H_{\text{triv}} + sH_{\text{prob}}, \quad (27)$$

where  $s = s(t)$  is a time-dependent parameter changing from 0 to 1 during the time interval from  $t = 0$  to  $t = t_f$ . In the context of trapped-ion spin models, the trivial spin Hamiltonian can be an effective magnetic field, as described by Eq. (3), and the Hamiltonian of interest can be a fully connected transverse Ising model of Eq. (25). The determination of ground states of the long-range transverse-field Ising model cannot always be predicted, even with just a few dozen spins (Sandvik, 2010).

Although the fidelity of remaining in the ground state of Eq. (27) can always be improved by evolving more slowly, a practical upper limit on the transition time is enforced by the finite coherence time of the chosen experimental platform. Given a fixed transition time, it is possible to further optimize the preparation fidelity by adjusting the transition rate based on the local energy gap to the nearest excited state (Richerme, Senko, Smith *et al.*, 2013). Such ‘‘local adiabatic evolution’’ can be used for improved preparation and determination of

many-body ground states in a trapped-ion quantum simulator. Compared to other adiabatic methods, local adiabatic evolution (Roland and Cerf, 2002) yields the highest probability of maintaining the ground state in a system that is made to evolve from an initial Hamiltonian to the Hamiltonian of interest. Compared to optimal control methods (Krotov, 1996; Khaneja *et al.*, 2005), local adiabatic evolution may require knowledge of only the lowest  $\sim N$  eigenstates of the Hamiltonian rather than all  $2^N$  values. These methods have been used in both linear Paul traps (Richerme, Senko, Smith *et al.*, 2013) and Penning traps (Safavi-Naini *et al.*, 2018) to demonstrate optimized ground-state preparation as well as a method to find the ground-state spin ordering, even when the evolution is nonadiabatic.

For example, to find the ground state of a fully connected Ising Hamiltonian in Eq. (25) via an adiabatic protocol, the spins can be initialized to point along the transverse magnetic field direction with  $B_y \gg \max(J_{ij})$ . This initial state is, to good approximation, the instantaneous ground state of the full equation (25). After initialization, the time-dependent transverse field  $B_y(t)$  can then be ramped adiabatically from  $B_y(t = 0) = B_0$  to  $B_y(t = t_f) = 0$ , ensuring that the system remains in its instantaneous ground state during its evolution, as depicted in Fig. 8. At the conclusion of the ramp, the ground-state spin ordering of the Ising Hamiltonian [the first term in Eq. (25)] may be either directly read out or used as a starting point for further experiments.

### 1. Adiabatic ramp profiles

Figure 9 shows the energy level spectrum for the Hamiltonian in Eq. (25) for  $N = 6$  spins. Since the Hamiltonian obeys  $Z_2$  symmetry (Sachdev, 2011) (as well as parity symmetry in the experiments), the ground state  $|g\rangle$  is coupled to only a subset of the excited energy eigenstates. The first coupled excited state, shown in red in Fig. 9, is the lowest energy excited state  $|e\rangle$  for which  $\langle e|\sigma_y|g\rangle \neq 0$ . This state displays a general property seen in most adiabatic quantum simulations, namely, the existence of a critical gap  $\Delta_c$  that is central to parametrizing the adiabaticity of a given ramp. Many different ramp profiles allow one to transform from the initial Hamiltonian to the Ising Hamiltonian, each with different implications for adiabaticity and ground-state preparation. Three possibilities are discussed next.

*Linear ramps.*—For a linear ramp, the time-dependent transverse field  $B_y$  in Eq. (25) takes the form  $B_y^{\text{lin}}(t) = B_0(1 - t/t_f)$ , with a ramp profile shown in Fig. 10(a). To determine whether or not such a ramp is adiabatic, it can be compared to the adiabatic criterion (Messiah, 1962)

$$\left| \frac{\dot{B}_y(t)\epsilon}{\Delta_c^2} \right| \ll 1, \quad (28)$$

where  $\dot{B}_y(t)$  is the rate at which the transverse field is changed and  $\epsilon = \max[\langle e|dH/dB_y|g\rangle]$  is a number of the order of unity that parametrizes the coupling strength between the ground state  $|g\rangle$  and the first coupled excited state  $|e\rangle$ . Equation (28) highlights that fast ramps and small critical gaps can greatly decrease adiabaticity.

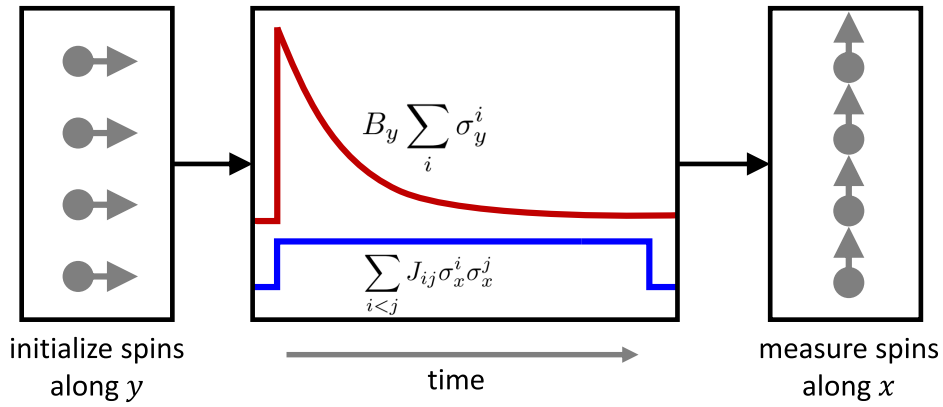


FIG. 8. After preparing the spins in the ground state of a  $y$ -polarized field  $B_y$ , the spins evolve subject to a long-range transverse Ising model described by Eq. (25), with the condition  $B_y(t=0) \gg J_{ij}$ . During the evolution, the strength of the field (upper decaying curve) is reduced to zero or an intermediate value compared to the Ising couplings (lower constant curve). Finally, the spins are measured along any axis of the Bloch sphere. [In much of the work reported later, the measurements are taken to be along the Ising-coupling ( $x$ ) direction of the Bloch sphere for each ion.] If the evolution were adiabatic, the resulting state should have remained in the ground state of the Hamiltonian throughout. Adapted from [Islam \*et al.\*, 2011](#).

To satisfy the adiabatic criterion, a linear ramp must proceed slowly enough that the total time  $t_f \gg B_0/\Delta_c^2$ . For the  $N = 6$  Ising Hamiltonian shown in Fig. 9,  $B_0 = 3.9$  kHz and  $\Delta_c = 0.29$  kHz, giving the adiabaticity requirement  $t_f \gg 46$  ms. This time is long compared to the typical coherence time of ion-trap quantum simulation experiments. It is therefore desirable to seek alternative ways to decrease  $B(t)$  more quickly while maintaining adiabaticity.

**Exponential ramps.**—Decreasing the transverse field exponentially according to  $B_y^{\text{exp}}(t) = B_0 \exp(-t/\tau)$ , with  $t_f = 6\tau$ , can yield a significantly more adiabatic evolution than linear ramps for the same  $t_f$ . Figure 9 shows that the instantaneous gap  $\Delta$  between the ground and first coupled excited state is large at the beginning of the ramp and small only when  $B$  approaches 0. Exponential ramps exploit this gap structure by quickly changing the field at first, then gradually slowing the rate of change as  $t \rightarrow t_f$ . Such ramps have been used to produce ground states in several of the previously discussed

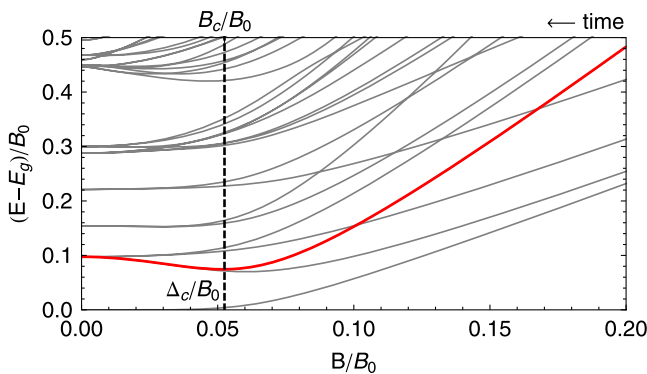


FIG. 9. Low-lying energy eigenvalues of Eq. (25) for  $N = 6$ , with the ground-state energy  $E_g$  set to 0,  $B_0 = 5J_{\text{max}}$ , and the long-range  $J_{ij}$  couplings determined from experimental conditions (see the text). The bold line indicates the first coupled excited state, the minimum of which determines the critical field  $B_c$  and the critical gap  $\Delta_c$ . From [Richerme, Senko, Smith \*et al.\*, 2013](#).

experiments, such as those given by [Kim \*et al.\* \(2010\)](#) and [Islam \*et al.\* \(2011, 2013\)](#).

At the critical point of the Hamiltonian shown in Fig. 9,  $|\dot{B}_{\text{exp}}(t)| = 0.3B_0/t_f$ . The adiabaticity criterion of Eq. (28) then requires  $t_f \gg 14.5$  ms, a factor of 3 less time than the requirement found for linear evolution. Note that the adiabaticity gains of exponential ramps can be realized whenever the critical gap occurs toward the end of the ramp ( $B_c/B_0 < \tau/t_f$ ), which is generally the case for the transverse Ising Hamiltonian of Eq. (25).

**Local adiabatic ramps.**—Local adiabatic ramps seek to keep the adiabaticity fixed at all points along the evolution by adjusting  $\dot{B}_y(t)$  based on the instantaneous gap  $\Delta[B_y(t)]$  that varies with the field profile  $B_y(t)$  ([Roland and Cerf, 2002](#); [Quan and Zurek, 2010](#)). If the adiabaticity parameter is defined as

$$\gamma = \left| \frac{\Delta[B_y(t)]^2}{\dot{B}_y(t)} \right|, \quad (29)$$

then a local adiabatic ramp would follow the profile  $B_y(t)$  that solves the differential Eq. (29) with  $\gamma$  fixed. Adiabaticity then requires  $\gamma \gg 1$ .

To solve Eq. (29), it is necessary to know  $\Delta(t)$  everywhere along the evolution. This requires knowledge of the first coupled excited state of the  $N$ -spin Hamiltonian of Eq. (25), which is always the first excited state at  $B_y = 0$  and the  $(N + 1)$ st excited state at large  $B_y$ . Determining the local adiabatic evolution profile therefore relies on calculation of only the lowest  $\sim N$  eigenvalues, which is much more computationally approachable than direct diagonalization of a  $2^N \times 2^N$  matrix ([Lanczos, 1950](#)).

For a local adiabatic ramp, the total evolution time  $t_f$  may be calculated by integrating Eq. (29). Since  $\dot{B}_y(t)$  is negative throughout the evolution,

$$t_f = \gamma \int_0^{B_0} \frac{dB}{\Delta^2(B)}, \quad (30)$$

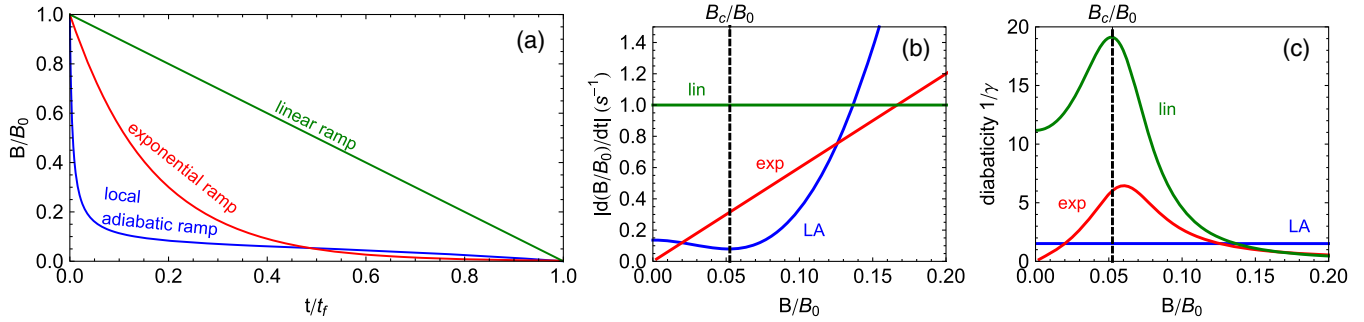


FIG. 10. (a) Local adiabatic ramp profile calculated for the energy levels in Fig. 9, along with a linear ramp and an exponential ramp with decay constant  $\tau = t_f/6$ . (b) The slope of the local adiabatic (LA) ramp is minimized at the critical field value  $B_c$ , and is smaller than the slopes of the exponential and linear ramps at the critical point. (c) The inverse of the adiabaticity parameter  $\gamma$  (see the text) is peaked near the critical point for exponential and linear ramps but constant for the local adiabatic profile. Adapted from Richerme, Senko, Smith *et al.*, 2013.

which shows a linear relationship between the total time  $t_f$  and the adiabaticity parameter  $\gamma$ . Satisfying the adiabaticity condition  $\gamma \gg 1$  for the Hamiltonian in Fig. 9 implies  $t_f \gg 3.6$  ms, a factor of 4 and 12 less time than exponential and linear ramps, respectively. The fact that local adiabatic evolution can lead to faster ramps while satisfying adiabaticity was well explored by Roland and Cerf (2002), who showed that local adiabatic ramps could recover the quadratic speedup of Grover’s quantum search algorithm (Nielsen and Chuang, 2000). In contrast, it was found that linear ramps offer no improvement over classical search algorithms (Farhi *et al.*, 2000).

Figure 10(a) compares linear, exponential, and local adiabatic ramp profiles for the Hamiltonian shown in Fig. 9. The local adiabatic ramp spends much of its time evolution in the vicinity of the critical point, since the transverse field changes slowly on account of the small instantaneous gap. This is further illustrated in Fig. 10(b), which shows that at the critical point the slope of the local adiabatic ramp is minimized and smaller than slopes of the exponential or linear ramps. As a result, the inverse adiabaticity  $1/\gamma$  peaks near the critical point for exponential and linear ramps, greatly increasing the probability of nonadiabatic transitions away from the ground state; see Fig. 10(c). By design, the local adiabatic ramp maintains constant adiabaticity for all values of  $B$  and does not suffer from large nonadiabaticities near  $B_c$ .

## 2. General adiabatic simulation issues

To determine the effects of a chosen adiabatic ramp protocol, the probability of creating the ground state can be measured following any chosen ramp profile of identical times. Richerme, Senko, Smith *et al.* (2013) used  $N = 6$  ions and chose the trap voltages and the laser detuning  $\mu$  to give AFM spin-spin interactions of the form  $J_{ij} \approx (0.77 \text{ kHz})/|i - j|$ . These long-range AFM interactions lead to a fully connected, frustrated system, as all couplings cannot be simultaneously satisfied. Nevertheless, the ground state of this system reduces to an equal superposition of the two Néel-ordered AFM states  $(|\uparrow\downarrow\uparrow\downarrow\uparrow\downarrow\rangle + |\uparrow\downarrow\uparrow\downarrow\uparrow\downarrow\rangle)/\sqrt{2}$ .

The data in Fig. 11 show how the AFM ground-state probability grows during a single 2.4 ms linear, exponential,

or local adiabatic ramp. Each data point is the result of 4000 repetitions of the same experiment, with error bars that account for statistical uncertainty as well as estimated drifts in the Ising-coupling strengths. In agreement with the previous arguments, the data show that local adiabatic ramps prepare the ground state with higher fidelity than exponential or linear ramps. The ground-state population grows quickly under local adiabatic evolution since the transverse field  $B(t)$  is reduced quickly at first. In contrast, the linear ramp does not approach the paramagnetic-to-AFM phase transition until  $\sim 2$  ms, and the AFM probability is suppressed until this time.

The solid lines in Fig. 11 plot the theoretical prediction of the ground-state probability with no free parameters. In each case, the Schrödinger equation is numerically integrated using Hamiltonian (25), the desired  $B(t)$ , and the initial state  $|\psi(0)\rangle = |\downarrow\downarrow\downarrow\dots\rangle_y$ . At the end of the ramp, the overlap between the final state  $|\psi(t_f)\rangle$  and the AFM ground state  $(|\uparrow\downarrow\uparrow\dots\rangle + |\uparrow\downarrow\uparrow\dots\rangle)/\sqrt{2}$  is calculated to extract the probability of the ground-state spin configuration. Effects of decoherence-induced decay in the ground-state probability are included by multiplying the calculated probability at time  $t$

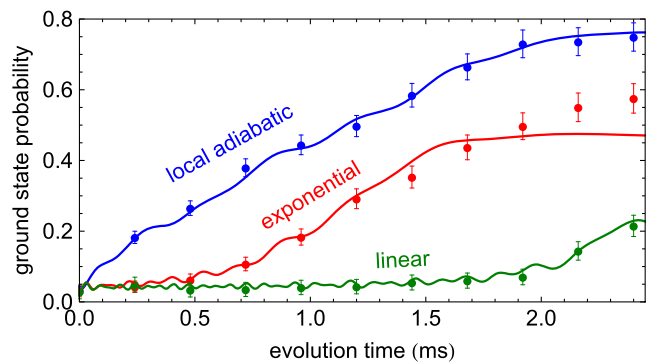


FIG. 11. Probability of preparing the AFM ground state for various times during  $t_f = 2.4$  ms simulations with three different ramp profiles. The linear ramp takes  $\sim 2.3$  ms to reach the critical point, while the local adiabatic and exponential ramps need only 1.2 ms. Locally adiabatic ramps yield the highest preparation fidelity at all times. Adapted from Richerme, Senko, Smith *et al.*, 2013.



by  $\exp(-t/t_d)$ , where  $t_d$  is the measured  $1/e$  coherence time of the spin-spin interactions. The key to all adiabatic protocols is that the ramp rate must remain slow when compared to the critical energy gap, as shown in Eq. (28). However, determining the scaling of the critical gap with system size is itself a difficult problem in the general case (Albash and Lidar, 2018). For simple problems, such as the ground state of a Lipkin-Meshkov-Glick model, the gap is known to shrink only polynomially for large  $N$  (Caneva, Fazio, and Santoro, 2008). For more complex problems, such as those in the  $NP$ -complexity class, the gap may close exponentially quickly with increasing system size (Das and Chakrabarti, 2008; Morita and Nishimori, 2008). In these cases, or in cases for which the gap scaling is unknown, experimental implementations require exponentially longer ramp times to ensure that adiabaticity is maintained as the problem size grows.

One obvious question is whether quantum adiabatic protocols are useful for solving complex computation or quantum many-body type problems. There are some reasons to be hopeful. For certain problems, such as the Grover search algorithm, the use of local adiabatic ramp profiles has been shown to provide the same quadratic quantum advantage as found in the circuit model (Roland and Cerf, 2002). For other problems, such as finding the ground state of a transverse-field Ising model, adiabatic quantum protocols can provide a polynomial speedup over simulated annealing (Kadowaki and Nishimori, 1998). Although exponential speedups are more elusive, finding such examples is nevertheless an active area of research.

While adiabatic simulation protocol allows for the preparation of the ground state of nontrivial spin models, maintaining the adiabatic condition [Eq. (28)] for a large system within the constraint of an experimentally realistic coherence time will be challenging. Alternate protocols have been explored to bypass the strict requirements of adiabaticity while achieving high ground-state probability. For example, a “bang-bang” control of the Hamiltonian has been suggested (Viola and Lloyd, 1998; Balasubramanian *et al.*, 2018) where the initial trivial Hamiltonian can be quenched to an

intermediate Hamiltonian, followed by a final quench to the problem Hamiltonian. In another approach, a classical-quantum hybrid protocol [the quantum approximate optimization algorithm (QAOA) (Farhi, Goldstone, and Gutmann, 2014)] theoretically enables an ultrafast creation of ground states (Ho, Jonay, and Hsieh, 2019). Implementations of this method are discussed in detail in Sec. V.B.2. Here we restrict our discussions to adiabatic simulation protocols.

## B. Experimental progress in adiabatic quantum simulation

### 1. Transverse Ising model with a small number of spins

The adiabatic preparation of the ground state for the transverse Ising model was first demonstrated with two trapped-ion spins, as shown in Fig. 12 (Friedenauer *et al.*, 2008; Schneider, Porras, and Schaetz, 2012), followed by experiments with three spins (Kim *et al.*, 2009, 2010, 2011; Edwards *et al.*, 2010; Khromova *et al.*, 2012). These entry experiments demonstrated the adiabatic evolution from paramagnetic initial state to magnetically ordered ground state and allowed tests of adiabaticity (Edwards *et al.*, 2010) and direct measures of entanglement in the ground state (Kim *et al.*, 2010, 2011). The three-spin system, moreover, supports spin frustration, or a competition between the nearest and next-nearest couplings in the case of AFM ground states. By tuning the system to have either FM or AFM ground states, two different types of magnetic order were indeed measured, paralleling the two different classes of entanglement known to exist with exactly three spins (Acín *et al.*, 2001).

For the case of three Ising spins, the transverse Ising Hamiltonian (25) is reduced to

$$H_3 = J_1 \left( \sigma_x^{(1)} \sigma_x^{(2)} + \sigma_x^{(2)} \sigma_x^{(3)} \right) + J_2 \sigma_x^{(3)} \sigma_x^{(1)} + B_y(t) \left( \sigma_y^{(1)} + \sigma_y^{(2)} + \sigma_y^{(3)} \right), \quad (31)$$

where the transverse field and the Ising interaction are chosen to act along the  $y$  axis and  $x$  axis, respectively. This is the simplest Hamiltonian that can exhibit frustration in the

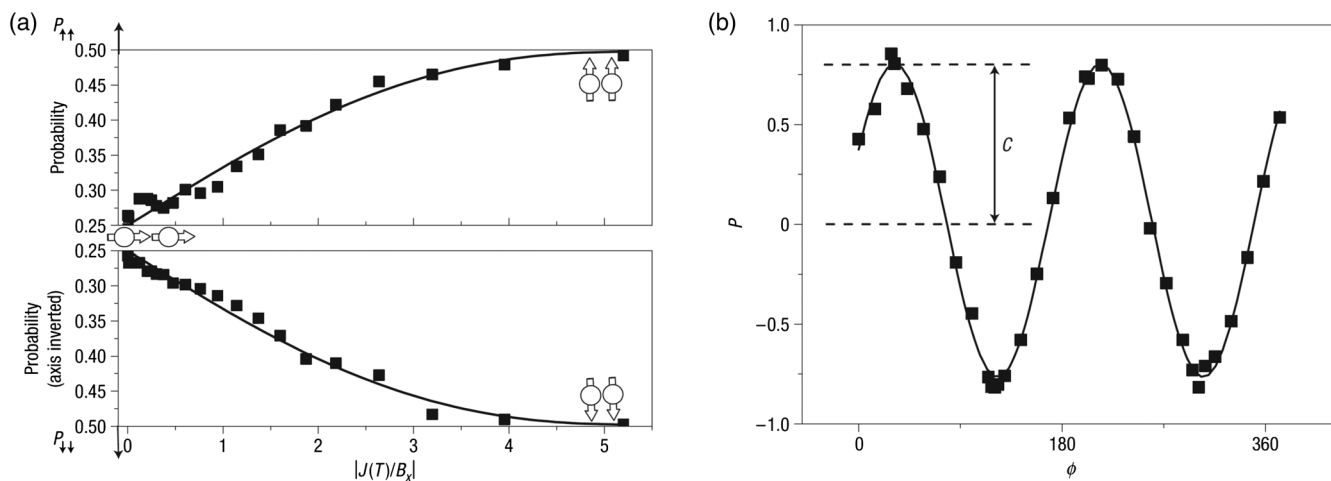


FIG. 12. (a) Observed adiabatic evolution of two trapped-ion spins from a paramagnetic state to a ferromagnetic (FM) state. (b) The observed parity oscillation signal of the resulting FM state upon a subsequent rotation of both spins reveals the amount of entanglement in the ground state. From Friedenauer *et al.*, 2008.

ground state due to a compromise between the various Ising couplings.

As seen in Eq. (22), the sign and the strength of the Ising couplings  $J_{ij}$  can be controlled by the proper choice of the driving field detuning  $\delta_m$  from the motional modes. For three spins, the expected and measured nearest-neighbor (NN) interactions  $J_1 \equiv J_{1,2} = J_{2,3}$  and the next-nearest-neighbor (NNN) interaction  $J_2 \equiv J_{1,3}$  are shown in Fig. 5. For certain ranges of the drive field detuning, both NN and NNN couplings have AFM interactions ( $J_1, J_2 > 0$ ), and for other domains both show FM interactions ( $J_1, J_2 < 0$ ).

Figure 13(a) shows the time evolution for the Hamiltonian frustrated with nearly uniform AFM couplings and gives almost equal probabilities for the six AFM states  $|\downarrow\downarrow\downarrow\rangle$ ,  $|\uparrow\uparrow\uparrow\rangle$ ,  $|\downarrow\downarrow\uparrow\rangle$ ,  $|\uparrow\uparrow\downarrow\rangle$ ,  $|\downarrow\uparrow\downarrow\rangle$ , and  $|\uparrow\downarrow\uparrow\rangle$  (labeled in the x

basis of the Bloch sphere and accounting for 3/4 of all possible spin states) at  $B_y \approx 0$ . Because  $J_2 < 0.8J_1$  for these data, a population imbalance also develops between symmetric ( $|\downarrow\downarrow\downarrow\rangle$  and  $|\uparrow\uparrow\uparrow\rangle$ ) and asymmetric ( $|\downarrow\downarrow\uparrow\rangle$ ,  $|\uparrow\uparrow\downarrow\rangle$ ,  $|\downarrow\uparrow\downarrow\rangle$ , and  $|\uparrow\downarrow\uparrow\rangle$ ) AFM states. Figure 13(b) shows the evolution to the two ferromagnetic states ( $|\downarrow\downarrow\downarrow\rangle$  and  $|\uparrow\uparrow\uparrow\rangle$ ) as  $B_y \rightarrow 0$ , where all interactions are FM.

The adiabatic evolution of the ground state of Hamiltonian (31) from  $B_y \gg J_{\text{rms}}$  to  $B_y \ll J_{\text{rms}}$  should result in an equal superposition of all ground states and therefore be entangled. For instance, for the isotropic AFM case, the ground state is expected to be  $|\downarrow\downarrow\downarrow\rangle + |\uparrow\uparrow\uparrow\rangle + |\downarrow\downarrow\uparrow\rangle - |\uparrow\uparrow\downarrow\rangle - |\downarrow\uparrow\downarrow\rangle - |\uparrow\downarrow\uparrow\rangle$ . For the FM case, the ground state is a Greenberger-Horne-Zeilinger (GHZ) state  $|\downarrow\downarrow\downarrow\rangle - |\uparrow\uparrow\uparrow\rangle$ . The entanglement in the system at each point in the adiabatic

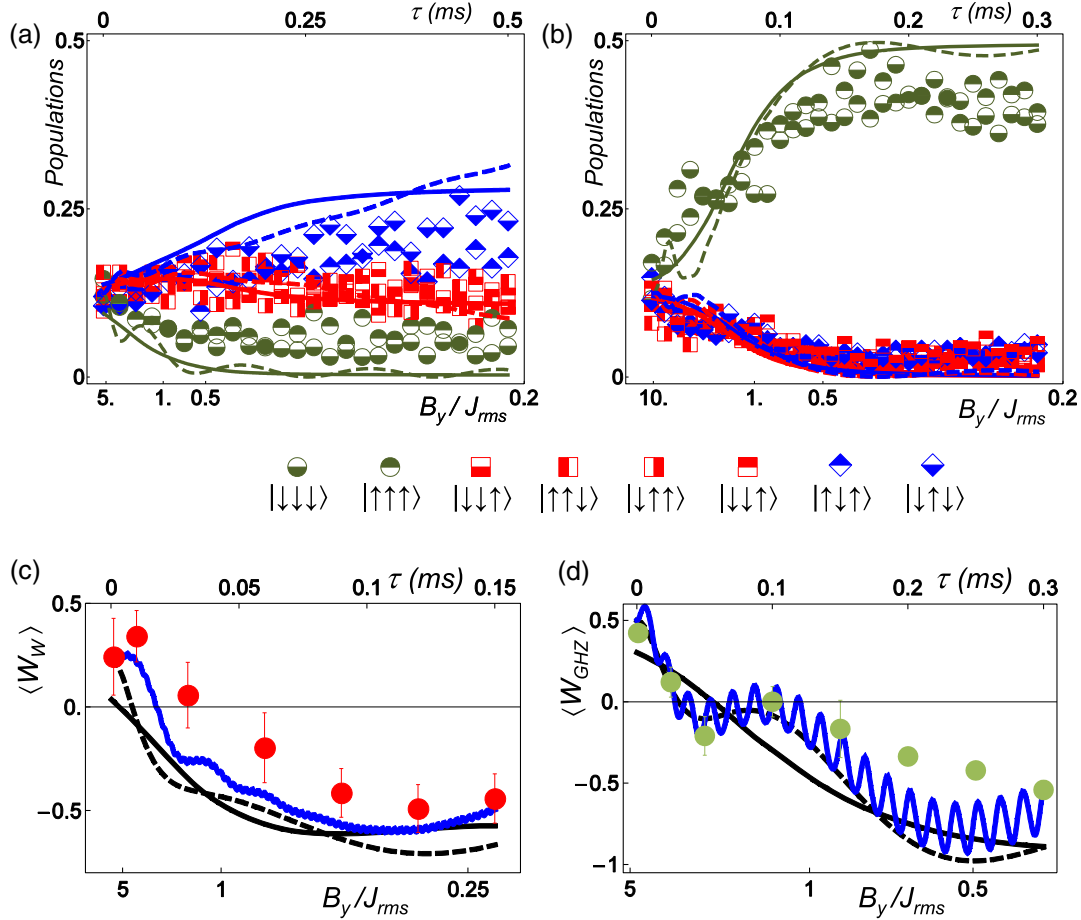


FIG. 13. Evolution of each of the eight spin states, measured with a CCD camera, plotted as  $B_y/J_{\text{rms}}$  is ramped down in time. The dotted lines correspond to the populations in the exact ground state and the solid lines represent the theoretical evolution expected from the actual ramp. (a) All interactions are AFM. The FM-ordered states vanish and the six AFM states are all populated as  $B_y \rightarrow 0$ . Because  $J_2 \approx 0.8J_1$ , a population imbalance also develops between symmetric and asymmetric AFM. (b) All interactions are FM, with evolution to the two ferromagnetic states as  $B_y \rightarrow 0$ . (c) Entanglement generation for the case of an all AFM interaction, where the symmetric W-state witness  $W_W$  is used. The entanglement emerges for  $B_y/J_{\text{rms}} < 1.1$ . (d) Entanglement generation for the all FM interactions, where the GHZ witness  $W_{\text{GHZ}}$  is used. The entanglement occurs when  $|B_y|/J_{\text{rms}} < 1$ . In both (c) and (d) the error bars represent the spread of the measured expectation values for the witness, likely originating from the fluctuations of experimental conditions. The solid black lines are theoretical witness values for the exact expected ground states, and the black dashed lines describe theoretically expected values at the actual ramps of the transverse field  $B_y$ . The blue (gray) lines reveal the oscillation and suppression of the entanglement due to the remaining spin-motion couplings, showing better agreement with the experimental results. Adapted from Kim *et al.*, 2011.

evolution can be characterized by measuring particular entanglement witness operators (Gühne and Tóth, 2009). When the expectation value of such an operator is negative, this indicates entanglement of a particular type defined by the witness operator. For the AFM frustrated case shown in Fig. 13(c), the expectation of the symmetric W-state witness  $W_W = (4 + \sqrt{5})\hat{I} - 2(\hat{\mathcal{J}}_x^2 + \hat{\mathcal{J}}_y^2)$  is measured (Gühne and Tóth, 2009). For the FM case shown in Fig. 13(d), the expectation of the symmetric GHZ witness operator  $W_{\text{GHZ}} = 9\hat{I}/4 - \hat{\mathcal{J}}_x^2 - \sigma_y^{(1)}\sigma_y^{(2)}\sigma_y^{(3)}$  (Sackett *et al.*, 2000; Gühne and Tóth, 2009) is measured, where  $\hat{I}$  is the identity operator and  $\hat{\mathcal{J}}_i \equiv (1/2)(\sigma_i^{(1)} + \sigma_i^{(2)} + \sigma_i^{(3)})$  is proportional to the  $l$ th projection of the total effective angular momentum of the three spins. In both cases, as shown in Figs. 13(c) and 13(d), entanglement of the corresponding form is observed during the adiabatic evolution.

## 2. Onset of quantum many-body effects with increasing system size

The ground state in the transverse-field Ising model [Eq. (25)] undergoes a crossover between polarized or paramagnetic and magnetically ordered spin states, as the relative strengths of the transverse field  $B_y$  and the Ising interactions  $J_{ij}$  are varied. For  $|B_y/J_{ij}| \gg 1$ , the ground state has the spins independently polarized (paramagnetic phase). For  $|B_y/J_{ij}| \ll 1$ , the ground state is magnetically ordered for  $|B_y/J_{ij}| \ll 1$ , with ferromagnetic order for  $J_{ij} < 0$  in Eq. (25). A second-order quantum phase transition is predicted for this model in the thermodynamic limit (Sachdev, 2011) when the magnitude of the transverse field is comparable to the interaction strength. The presence or absence of a spin order can be quantified by adopting a suitable order parameter. For example, the average absolute magnetization per site along the Ising direction

$$m_x = \frac{1}{N} \sum_{s=0}^N |N - 2s| P(s) \quad (32)$$

differentiates between a ferromagnetic state and paramagnetic state. Here  $P(s)$  is the probability of finding  $s$  spins in the  $|\uparrow\rangle$  state ( $s = 0, 1, 2, \dots, N$ ) along  $x$ . To remove a finite size effect due to the difference between binomial and Gaussian distributions, a scaled order parameter  $\bar{m}_x = (m_{x,N}^0 - m_x)/(m_{x,N}^0 - 1)$  can be adopted. Here  $m_{x,N}^0 = (1/N2^N) \sum_{s=0}^N \binom{N}{s} |N - 2s|$  is the average absolute magnetization of the paramagnetic state. This scaled order parameter assumes a value of  $\bar{m}_x = 1$  in the ideal ferromagnetic state, and a value of  $\bar{m}_x \approx 0$  in the paramagnetic state. A finite system does not support a phase transition but shows a smooth crossover from the paramagnetic to the spin-ordered phases that becomes sharper as the system size is increased. Higher-order moments of the distribution of measured spins may be more suitable to extract the phase transition point from experiments performed on finite system sizes. For instance, the fourth magnetization moment is known as the Binder cumulant

$$g = \frac{\sum_{s=0}^N (N - 2s)^4 P(s)}{[\sum_{s=0}^N (N - 2s)^2 P(s)]^2}. \quad (33)$$

The Binder cumulant can also be scaled to remove the finite size effect, as before, by defining  $\bar{g} = (g_N^0 - g)/(g_N^0 - 1)$ , where  $g_N^0 = 3 - 2/N$  is the Binder cumulant for the paramagnetic phase.

Figure 14 shows measurements of the mean magnetization and Binder cumulant in a transverse Ising system ranging from  $N = 2$  to  $N = 9$  atomic ion spins (Islam *et al.*, 2011). The observed sharpening of the crossover from paramagnetic-to-ferromagnetic spin order with system size (Fig. 14) is consistent with an onset of the quantum phase transition. In Fig. 14(a), theoretical values of both order parameters are shown for up to  $N = 100$  spins in an all-to-all coupled ferromagnetic transverse Ising model, with measurements and comparison to theory given in Figs. 14(b)–14(d). Both metrics have been scaled to take into account finite size effects (Islam *et al.*, 2011). Ferromagnetic spin order was also observed in adiabatic quantum simulation experiments with up to  $N = 16$  ions by directly measuring a bimodal distribution of magnetization (Islam *et al.*, 2013).

AFM ground states of the transverse-field Ising model [Eq. (25) with  $J_{ij} > 0$ ] are more difficult to prepare because the long-range AFM interactions lead to competing pairwise spin order, or frustration, as detailed with  $N = 3$  spins (Kim *et al.*, 2010) in Sec. III.B.1. Intuitively, the longer the range of AFM interactions, the less energy it takes to create spin-flip excitations. Thus the critical field required to destroy the AFM spin order is less than that with a relatively short-range interaction. The “critical gap” in the many-body energy spectra also decreases with increasing range of the AFM couplings (Fig. 15). The reduction of the critical gap with increased range of interaction was experimentally probed in a quantum simulation of the transverse-field Ising model [Eq. (25)] with the interaction profile following an approximate AFM power law [Eq. (23)] for  $N = 10$  spins (Islam *et al.*, 2013). The ratio of the transverse field to the Ising couplings was varied quasiadiabatically from a high transverse field to a final value of  $B/J_0 = 0.01$ . As the interaction range was increased and the critical gap closed, more excitations were created, resulting in a reduction in the ground-state order. This was observed through a decrease in the measured structure function

$$S(k) = \frac{1}{N-1} \left| \sum_{r=1}^{N-1} C(r) e^{ikr} \right|, \quad (34)$$

where the average correlation of spins along the Ising direction  $x$  and separated by  $r$  sites is

$$C(r) = \frac{1}{N-r} \sum_{m=1}^{N-r} \left( \langle \sigma_x^{(m)} \sigma_x^{(m+r)} \rangle - \langle \sigma_x^{(m)} \rangle \langle \sigma_x^{(m+r)} \rangle \right). \quad (35)$$

The measured structure function for  $N = 10$  spins [Fig. 15(a)] shows a decline at  $k = \pi$  as the interaction range is made longer, thus quantifying the degradations of nearest-neighbor antiferromagnetic spin order as the ground-state gap shrinks.

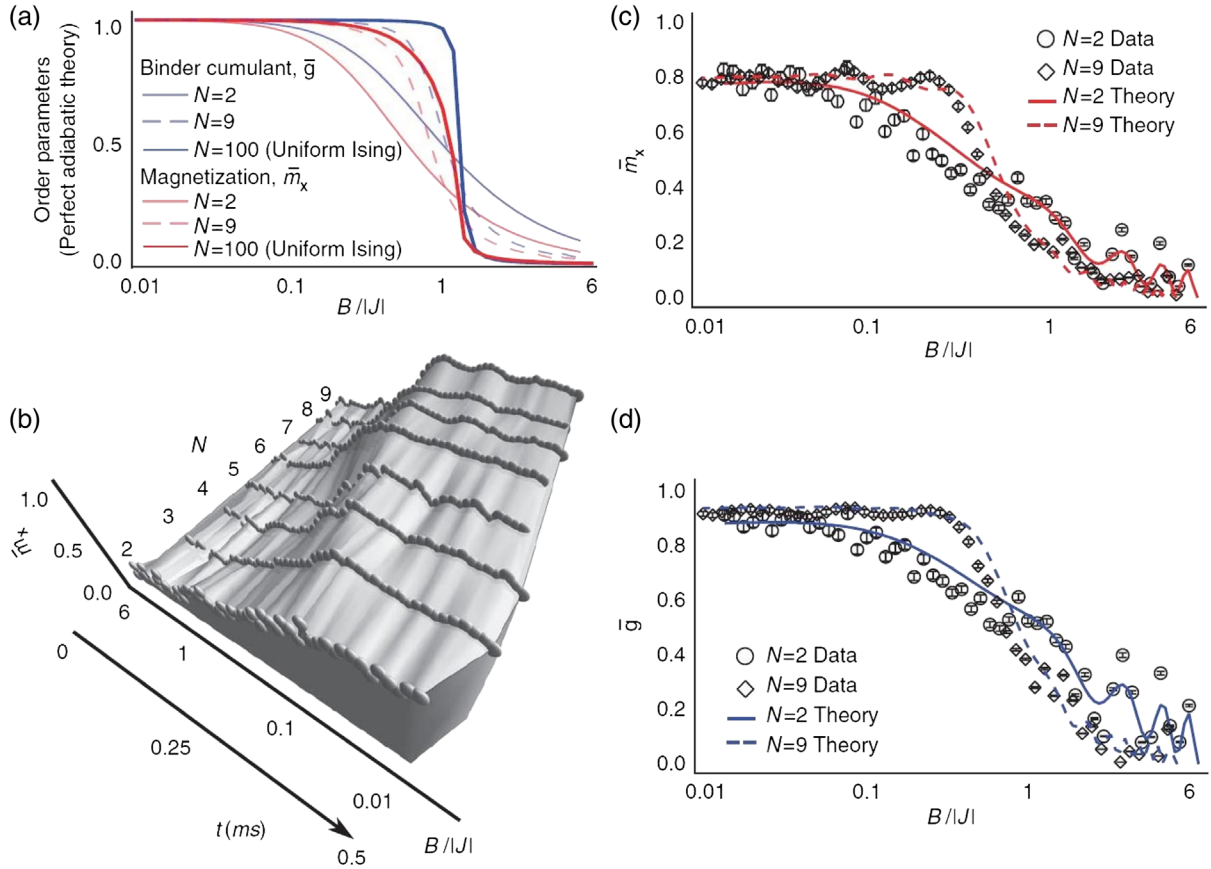


FIG. 14. Paramagnetic-to-ferromagnetic crossover in a small collection of trapped-ion spins. (a) Theoretical values of order parameters vs ratio of transverse field to average Ising coupling  $B/|J|$  for  $N = 2$  and 9 spins with nonuniform Ising couplings following the experiment given by Islam *et al.* (2011) and assuming perfect adiabatic time evolution. The order parameters, the Binder cumulant, and the magnetization are calculated by directly diagonalizing the relevant Hamiltonian [Eq. (25)]. Order parameters are also calculated for a moderately large system ( $N = 100$ ) with uniform Ising couplings to show the difference between these order parameters. (b) Measured magnetization vs  $B/|J|$  (and simulation time) plotted for  $N = 2 - 9$  spins, and scaled to the number of spins. As  $B/|J|$  is lowered, the spins undergo a crossover from a paramagnetic to a ferromagnetic phase. The crossover curves sharpen as the system size is increased from  $N = 2$  to 9, prefacing a phase transition in the limit of infinite system size. The oscillations in the data arise from the imperfect initial state preparation and nonadiabaticity due to finite ramping time. Measured (c) magnetization and (d) Binder cumulant vs  $B/|J|$  for  $N = 2$  (circles) and 9 spins (diamonds) with representative detection error bars. The data deviate from unity at  $B/|J| = 0$  owing to decoherence driven by the Raman transitions creating the Ising couplings. The theoretical curves (solid line for  $N = 2$  and dashed line for  $N = 9$  spins) are calculated by averaging over 10 000 quantum trajectories. From Islam *et al.*, 2011.

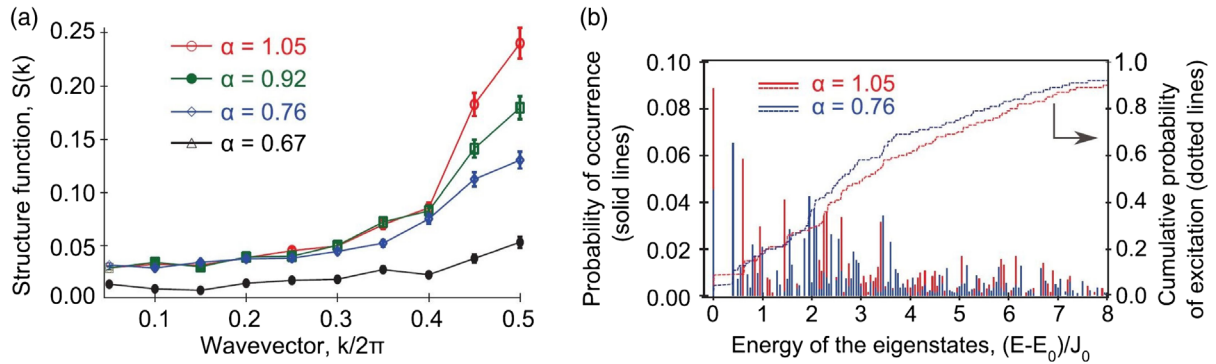


FIG. 15. (a) Structure function  $S(k)$  for various ranges of AFM interactions, for  $B/J_0 = 0.01$  in a system of  $N = 10$  spins. The increased level of frustration for the longer-range interactions reduces the observed antiferromagnetic spin order. The detection errors may be larger than shown here for the longest range of interactions, owing to spatial cross talk from their closer spacing. (b) Distribution of observed states in the spin system, sorted according to their energy  $E_i$  (with  $E_0$  denoting the ground-state energy) calculated exactly from Eq. (25) with  $B = 0$ . Data are presented for two ranges (red for  $\alpha = 1.05$  and blue for  $\alpha = 0.76$ ). The dashed lines indicate the cumulative energy distribution functions for these two ranges. Adapted from Islam *et al.*, 2013.

### 3. Ground-state identification

The ground-state spin ordering may still be determined experimentally even when the ramp is nonadiabatic. The key to ground-state identification is to examine the probability distribution of all spin configurations at the conclusion of the ramp and select the most prevalent state in the final eigenbasis. Consider an experiment where the spins are initialized into  $|\downarrow\downarrow\downarrow\dots\rangle_y$  (as usual) and the transverse field  $B(t)$  is instantly switched from  $B = B_0$  to  $B = 0$ . Measurement along the  $x$  direction would yield an equal superposition of all spin states; in this instance, the ground state is just as probable as any other state. If the transverse field  $B(t)$  is instead ramped at a fast but finite rate, the quantum simulation is slightly more adiabatic than the instantaneous case, and the ground state becomes slightly more prevalent than any other state. When  $B(t)$  is ramped slowly enough, the ground-state population is nearly 100% and dominates over that of any other state.

A close analogy may be drawn with a Landau-Zener process (Zener, 1932) in a two-level system composed of the ground and first coupled excited states. Adiabatic ramps correspond to half of a Landau-Zener process, in which  $B(t)$  starts with  $B \gg J$  and ends at  $B = 0$ . One can write an analytic expression to calculate the transition probability for this half-Landau-Zener evolution (Damski and Zurek, 2006), which has a maximum value of 0.5 for an instantaneous ramp. Any fast but finite ramp will give a transition probability  $< 0.5$ , so the ground state will always be more prevalent than the excited state.

The technique of identifying the most prevalent state as the ground state is subject to some limitations. First, the initial state (before the ramp) should be a uniform superposition of all spin states in the measurement basis, a condition satisfied by preparing the state  $|\downarrow\downarrow\downarrow\dots\rangle_y$  and measuring along  $\hat{x}$ . If some spin states are more prevalent than the ground state initially, then some nonzero ramp time will be necessary before the ground-state probabilities “catch up” and surpass these initially prevalent states. Second, the ramp must not cross any first-order transitions between ordered phases, as nonadiabatic ramps may not allow sufficient evolution time toward the new ground-state order. In addition, the initial and final states must share the same symmetry properties.

Finally, a good determination of the ground state requires that the difference between the measured ground-state probability  $P_g$  and the next excited state probability  $P_e$  be large relative to the experimental uncertainty, which is fundamentally limited by quantum projection noise  $\sim 1/\sqrt{n}$  after  $n$  repetitions of the experiment (Itano *et al.*, 1993). This implies that the most prevalent ground state can be determined reliably after repeating the measurement  $n > (P_g^2 + P_e^2)/(P_g - P_e)^2$  times. Assuming an exponential distribution of populated states during the ramp (as may be expected from Landau-Zener-like transitions), the number of required runs should then scale as  $n \sim (\bar{E}/\Delta)^2$  in the limit  $\bar{E} \gg \Delta$ , where  $\bar{E}$  is the mean energy imparted to the spins during the ramp and  $\Delta$  is the energy splitting between the ground and first coupled excited state.

If the gap shrinks exponentially with the number of spins  $N$  (i.e.,  $\Delta \sim e^{-N}$ ), ground-state identification thus requires an

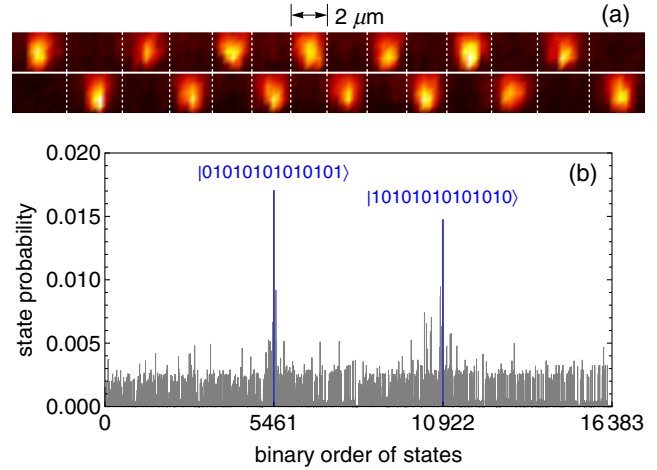


FIG. 16. (a) Fluorescence images of both AFM ground states prepared for  $N = 14$  trapped-ion spins, with bright =  $|\uparrow\rangle$  and dark =  $|\downarrow\rangle$  along the  $x$  direction of the Bloch sphere of each spin. (b) State probabilities of all  $2^{14} = 16384$  spin configurations for a 14-ion system following a local adiabatic ramp, ordered by binary index of the states (i.e.,  $|\downarrow\downarrow\downarrow\dots\downarrow\rangle = 0$  and  $|\uparrow\uparrow\dots\uparrow\rangle = 16383$ ). The Néel-ordered ground states 5461 and 10922 are unambiguously the most prevalent, despite a total probability of only 3%. From Richerme, Senko, Smith *et al.*, 2013.

exponential number of measurements  $n$  in the simulation. However, in cases where the gap shrinks like a power law ( $\Delta \sim N^{-\alpha}$ ), the most prevalent state can be ascertained in a time that scales polynomially with the number of spins. Regardless of the scaling, techniques that improve the ground-state probability (such as local adiabatic evolution) can greatly increase the contrast of the most prevalent state and reduce the number of necessary repetitions.

Figure 16 shows a direct identification of the ground-state AFM order of  $N = 14$  trapped-ion spins by imaging the most prevalent state created after a ramp. Each box in Fig. 16(a) contains an ion that scatters many photons when in the state  $|\uparrow\rangle$  and essentially no photons when in the state  $|\downarrow\rangle$ .

Figure 16(b) demonstrates the resiliency of the most prevalent state selection to ramps that are far from adiabatic. Identification of the ground state is clear, even though the total ground-state probability is only  $\sim 3\%$ . The requirement to satisfy the adiabatic criterion is replaced only by the requirement that the most prevalent state probabilities are accurately resolvable compared to those of any other state. While the method should remain robust for even larger  $N$ , ramps that are more adiabatic (by using longer ramp times or stronger spin-spin couplings) will decrease the number of experimental repetitions needed to resolve the state probabilities.

### 4. Classical Ising model

Adiabatic protocols can also be used to create the ground states of a classical spin model, catalyzed by quantum fluctuations. Consider the following system described by the transverse Ising model of Eq. (25) accompanied by a longitudinal field  $B_x$ :

$$H = \sum_{i<j} J_{ij} \sigma_x^i \sigma_x^j + B_x \sum_i \sigma_x^i + B_y(t) \sum_i \sigma_y^i. \quad (36)$$

When the transverse field  $B_y$  is set equal to 0 and the longitudinal field  $B_x$  is varied, this Hamiltonian exhibits many distinct ground-state phases separated by first-order classical phase transitions. Yet even for just a few spins the various ground states at different  $B_x$  are classically inaccessible in a physical system at or near zero temperature due to the absence of thermal fluctuations to drive the phase transitions (Sachdev, 2011). Quantum fluctuations are therefore required to reach these various ground states in a physical system.

Such quantum fluctuations can be introduced to the system by applying a transverse magnetic field, which does not commute with the longitudinal-field Ising Hamiltonian. Using  $N = 6$  or 10 spins, this technique has been used to experimentally identify the locations of the multiple classical phase transitions and to preferentially populate each of the classical ground states that arise for varying strengths of the longitudinal field (Richerme, Senko, Korenblit *et al.*, 2013). The ground-state spin ordering reveals a Wigner-crystal spin structure (Wigner, 1934) that maps to particular energy minimization problems (Katayama and Narihisa, 2001) and shows the first steps of the complete “devil’s staircase” (Bak and Bruinsma, 1982) expected to emerge in the  $N \rightarrow \infty$  limit.

Figure 17(a) shows the energy eigenvalues of the Hamiltonian given in Eq. (36) with  $B_y = 0$  for a system of

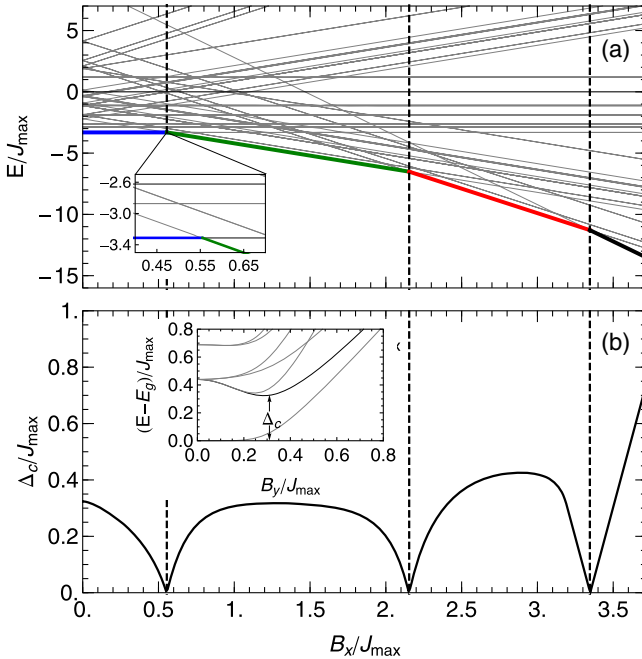


FIG. 17. (a) Low-lying energy eigenvalues of Eq. (36) for  $B_y = 0$  for  $N = 6$  spins, with the long-range  $J_{ij}$  couplings determined from experimental conditions (see the text). Inset: level crossings indicate the presence of first-order phase transitions in the ground state. (b) The critical gap  $\Delta_c$  shrinks to zero at the three phase transitions (vertical dashed lines). Inset: low-lying energy levels of Eq. (36) with  $B_x = 0$ . From Richerme, Senko, Korenblit *et al.*, 2013.

six spins. The ground state passes through three level crossings as  $B_x$  is increased from 0, indicating three classical first-order phase transitions separating four distinct spin phases. For each  $B_x$ , there is a critical point at some finite  $B_y$  characterized by a critical gap  $\Delta_c$  [inset of Fig. 17(b)]. When  $B_x$  is near a classical phase transition, the near energy degeneracy of spin orderings shrinks the critical gap, as shown in Fig. 17(b).

Long-range interactions give rise to many more ground-state spin phases than does a local Ising model. Consider an  $N$ -spin nearest-neighbor AFM model (Ising coupling  $J$ ) and a ground-state ordering  $|\dots\downarrow\uparrow\downarrow\uparrow\downarrow\uparrow\dots\rangle$ . An excited state at longitudinal field  $B_x = 0$  may have an additional spin polarized along  $|\downarrow\rangle$ , by making either a kink of type  $|\dots\downarrow\uparrow\downarrow\uparrow\downarrow\downarrow\dots\rangle$  or a spin defect of type  $|\dots\downarrow\uparrow\downarrow\downarrow\downarrow\uparrow\dots\rangle$ . The interaction energy gain of making  $n$  kinks is  $2nJ$ , while the field energy loss is  $2nB_x$ . At  $B_x/J = 1$ , multiple energy levels intersect to give a first-order phase transition. Similarly, the energy gain of making  $n$  spin defects is  $4nJ$  and the loss is  $2nB_x$ , so a second phase transition occurs at  $B_x/J = 2$ . Only three different ground-state spin phases are observable as  $B_x$  is varied from  $0 \rightarrow \infty$ , independent of  $N$ , and there is a large degeneracy of spin eigenstates at the phase transitions. The presence of long-range interactions lifts this degeneracy and admits  $[N/2] + 1$  distinct spin phases with  $\{0, 1, \dots, [N/2]\}$  spins in state  $|\uparrow\rangle$ , where  $[N/2]$  is the integer part of  $N/2$ .

To create the various spin phases, the experiment of Richerme, Senko, Korenblit *et al.* (2013) begins by optically pumping the effective spins to the state  $|\downarrow\downarrow\downarrow\dots\rangle_z$ . The spins are then coherently rotated into the equatorial plane of the Bloch sphere so that they point along  $\vec{B} = B_x\hat{x} + B_y(0)\hat{y}$ , with  $B_x$  varied between different simulations. The Hamiltonian of Eq. (36) is then switched on at  $t = 0$  with the chosen value of  $B_x$  and  $B_y(0) = 5J_{\max}$ . The transverse field (which provides the quantum fluctuations) is ramped down to  $B_y \approx 0$  exponentially with a time constant of 600  $\mu\text{s}$  and a total time of 3 ms, which sacrifices adiabaticity in order to avoid decoherence effects. At  $t = 3$  ms, the Hamiltonian is switched off and the  $x$  component of each spin is measured by applying a global  $\pi/2$  rotation about the  $\hat{y}$  axis, illuminating the ions with resonant light, and imaging the spin-dependent fluorescence using an intensified CCD camera. Experiments are repeated 4000 times to determine the probability of each possible spin configuration.

The order parameter of net magnetization along  $x$ ,  $M_x = N_{\uparrow x} - N_{\downarrow x}$ , can then be investigated as a function of longitudinal-field strength. The magnetization of the ground-state spin ordering of Eq. (36) is expected to yield a staircase with sharp steps at the phase transitions [the red line in Fig. 18(a)] when  $B_y = 0$  (Bak and Bruinsma, 1982). The experimental data [the blue points in Fig. 18(a)] show an averaged magnetization with heavily broadened steps due largely to the nonadiabatic exponential ramp of the transverse field. The deviation from sharp staircaselike behavior is predicted by numerical simulations [the solid blue line in Fig. 18(a)], which account for the implemented experimental parameters and ramp profiles. Differences between theory and experiment are largest near the phase transitions, where excitations are easier to make due to the shrinking critical gap [Fig. 17(b)].

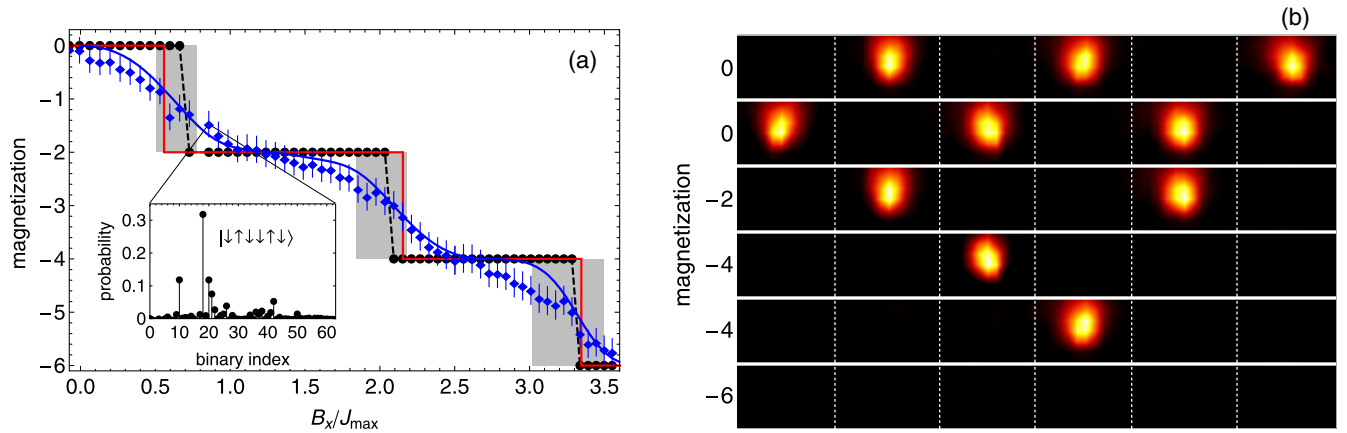


FIG. 18. (a) Magnetization ( $M_x = N_\uparrow - N_\downarrow$ ) of six ions for increasing axial field strength. Solid staircase line, magnetization of the calculated ground state, with the step locations indicating the first-order phase transitions; diamond points, average magnetization of 4000 experiments for various  $B_x$ ; solid smooth line, magnetization calculated by numerical simulation using experimental parameters; black dashed line, magnetization of the most probable state (see inset) found at each  $B_x$  value. Gray bands indicate the experimental uncertainty in  $B_x/J_{\max}$  at each observed phase transition. (b) Fluorescence images of the six ions with bright =  $|\uparrow\rangle$  and dark =  $|\downarrow\rangle$  along the  $x$  direction of the Bloch sphere of each spin, showing the ground states found at each step in (a):  $|\downarrow\uparrow\downarrow\uparrow\downarrow\rangle$  and  $|\uparrow\downarrow\uparrow\downarrow\uparrow\rangle$  ( $M_x = 0$ ),  $|\uparrow\downarrow\uparrow\downarrow\uparrow\rangle$  ( $M_x = -2$ ),  $|\downarrow\downarrow\uparrow\downarrow\downarrow\rangle$  and  $|\downarrow\downarrow\uparrow\downarrow\downarrow\rangle$  ( $M_x = -4$ ), and  $|\downarrow\downarrow\downarrow\downarrow\downarrow\rangle$  ( $M_x = -6$ ). Adapted from Richerme, Senko, Korenblit *et al.*, 2013.

The ground-state spin configuration at each value of  $B_x$  can be extracted by looking at the probability distribution of all spin states and selecting the most prevalent state [inset of Fig. 18(a)] (Richerme, Senko, Smith *et al.*, 2013). The magnetization of the spin states found by this method [the black points in Fig. 18(a)] recover the predicted staircase structure. The steps in the experimental curve agree with the calculated phase transition locations to within experimental error [the gray bands in Fig. 18(a)], which accounts for the statistical uncertainty due to quantum projection noise and estimated drifts in the strengths of  $J_{ij}$ ,  $B_x$ , and  $B_y$ .

Figure 18(b) shows approximately 1000 averaged camera images of the most probable spin configuration observed at each plateau in Fig. 18(a). Each box contains an ion that scatters many photons when in the state  $|\uparrow\rangle$  and essentially no photons when in the state  $|\downarrow\rangle$  along the  $x$  axis of the Bloch sphere. The observed spin orderings in Fig. 18(b) match the calculated ground states at each magnetization, validating the technique of using quantum fluctuations to preferentially create these classically inaccessible ground states. (For magnetizations  $M_x = 0$  and  $M_x = -4$ , two ground-state orderings are observed due to the left-right symmetry of the spin-spin interactions.)

To further illustrate the necessity of using quantum fluctuations to catalyze the magnetic phase transitions, alternate ramp trajectories can be used to reach a final chosen value of  $B_x$ . Figure 19(a) shows the ground-state phase diagram of the Hamiltonian in Eq. (36), with the sharp classical phase transitions visible along the bottom axis ( $B_y/J_{\max} = 0$ ). In addition, it shows two possible trajectories through the phase diagram that start in a paramagnetic ground state (which is easy to prepare experimentally) and end at the same value of  $B_x$  with  $B_y = 0$ .

The first trajectory, in which  $B_x$  is fixed and  $B_y$  is ramped from  $5J_{\max}$  to 0, was the one used in Fig. 18 to experimentally verify the locations of the three classical phase transitions and to experimentally create the four different ground-state

phases. Along this trajectory, Fig. 19(b) plots the probability of creating each ground state as a function of  $B_x$  and finds populations of  $\sim 40\%$ – $80\%$ . A smooth crossover between the four ground-state phases was observed, with the classical phase transitions occurring at the crossing points. This arises since distinct spin eigenstates have degenerate energies at the phase transition, causing the critical gap between them to close and allowing quantum fluctuations to populate both states equally; see Fig. 17.

The second trajectory in Fig. 19(a) is purely classical, with  $B_y$  set to 0. The spins are initialized into the state  $|\downarrow\downarrow\downarrow\downarrow\downarrow\rangle$  along  $x$ , and  $B_x$  is ramped from  $5J_{\max}$  to its final value at a rate of  $5J_{\max}/3$  ms. Figure 19(c) shows that, in a classical system without thermal or quantum fluctuations, the phase transitions remain undriven and the initial state  $|\downarrow\downarrow\downarrow\downarrow\downarrow\rangle$  remains dominant for all values of  $B_x$ . The ground-state phases with magnetizations 0 and  $-2$  [blue and green in Fig. 19(c)] are separated from the initial state by several classical phase transitions and have essentially zero probability of being created.

## 5. Spin-1 simulations

As with the previously described spin-1/2 systems, spin-1 systems (spanned by the three basis kets  $|+\rangle$ ,  $|0\rangle$ , and  $|-\rangle$ ) can likewise exhibit a variety of interesting new physics and ground-state phases. As a notable example, Haldane (1983) conjectured that integer-spin Heisenberg chains with nearest-neighbor AFM interactions are gapped, in contrast to gapless half-integer spin chains. This energy gap in integer-spin systems corresponds to short-range exponentially decaying correlation functions, as opposed to long-range power-law decaying correlations in half-integer systems. It was later suggested (den Nijs and Rommelse, 1989) that this Haldane phase of the spin-1 chain is governed by a hidden order that can be characterized by a nonlocal string order parameter and

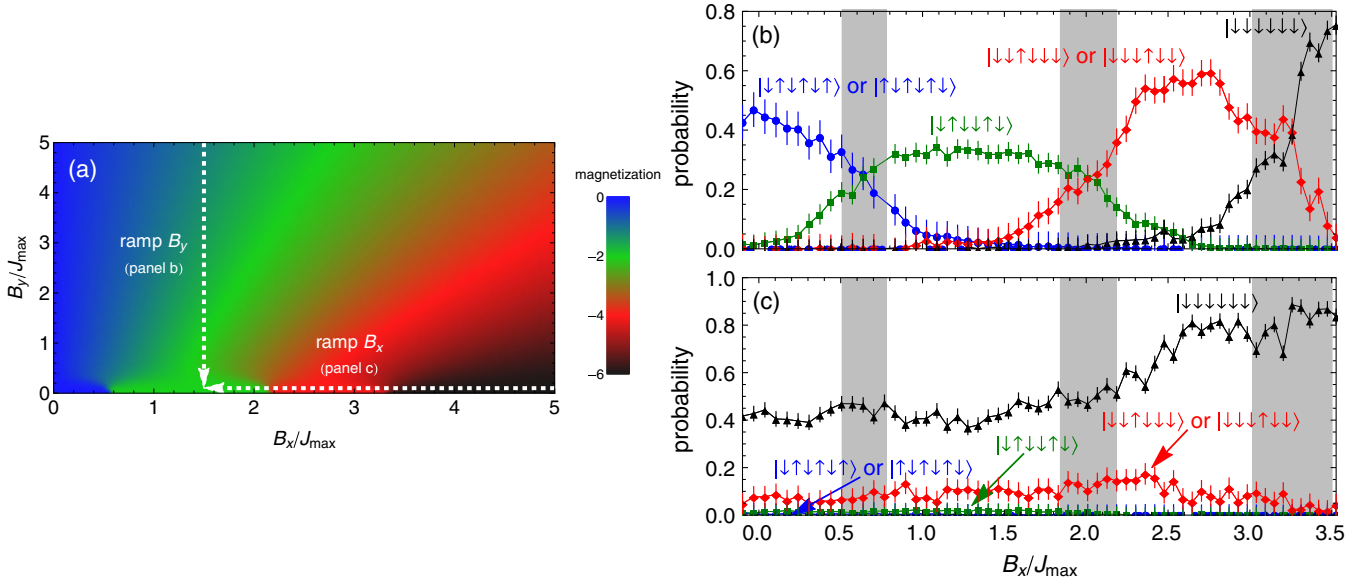


FIG. 19. (a) Ground-state phase diagram of the system, along with two different trajectories that end at the same value of  $B_x$ . (b) Probabilities of the four different ground-state spin phases when  $B_y$  is ramped in a six-ion system. Circles,  $|\uparrow\uparrow\uparrow\uparrow\uparrow\uparrow\rangle$  or  $|\uparrow\downarrow\uparrow\downarrow\uparrow\downarrow\rangle$ ; squares,  $|\downarrow\uparrow\downarrow\uparrow\downarrow\uparrow\rangle$ ; diamonds,  $|\downarrow\downarrow\uparrow\downarrow\uparrow\downarrow\rangle$  or  $|\downarrow\downarrow\downarrow\uparrow\downarrow\uparrow\rangle$ ; triangles,  $|\downarrow\downarrow\downarrow\uparrow\downarrow\uparrow\rangle$ . Gray bands are the experimental uncertainties of the phase transition locations. (c) Probabilities of creating the four different ground states when  $B_x$  is ramped. Most of the ground states are classically inaccessible in our zero-temperature system. Adapted from Richerme, Senko, Korenblit *et al.*, 2013.

is consistent with a full breaking of a hidden  $Z_2 \times Z_2$  symmetry (Kennedy and Tasaki, 1992). The Haldane phase can also be described by a doubly degenerate entanglement spectrum (Pollmann *et al.*, 2010), hinting at a topologically protected phase in one dimension. Effective spin-1 particles can be represented by three hyperfine levels in the  $^2S_{1/2}$  ground manifold of  $^{171}\text{Yb}^+$  ions:  $|+\rangle \equiv |F=1, m_F=1\rangle$ ,  $|-\rangle \equiv |F=1, m_F=-1\rangle$ , and  $|0\rangle \equiv |F=0, m_F=0\rangle$ . The  $|0\rangle$  and  $|\pm\rangle$  states are separated by frequencies  $\omega_{\pm}$ , as shown in Fig. 20. Here  $|+\rangle$ ,  $|-\rangle$ , and  $|0\rangle$  are the eigenstates of  $S_z$  with eigenvalues  $+1, -1$ , and  $0$ , respectively;  $F$  and  $m_F$  are quantum numbers associated with the total angular momentum of the atom and its projection along the quantization axis, defined by a magnetic field of  $\sim 5$  G. Spin-1 Ising couplings can be generated analogously to the spin-1/2 case detailed in Sec. I. Laser beams are applied to the ion chain with a wave vector difference along a principal axis of transverse motion, but here driving stimulated Raman transitions between both the  $|0\rangle$  and  $|-\rangle$  states and the  $|0\rangle$  and  $|+\rangle$  states with balanced Rabi frequencies  $\Omega_i$  on ion  $i$  (Kim *et al.*, 2009). To generate spin-1 XY interactions, two beat frequencies are applied at  $\omega_- + \mu$  and  $\omega_+ - \mu$  to these respective transitions, where  $\mu - \omega_m = \delta_m$  is the detuning from the transverse motional mode  $m$  sideband, as shown in Fig. 20. Under the approximations that the beat notes are far detuned ( $|\delta_m| \gg \eta_{i,m}\Omega_i$ ) and that  $\omega_{\pm} \gg \mu \gg \Omega_i$  (the rotating-wave approximation), the resulting interaction Hamiltonian in the Lamb-Dicke regime is (Senko *et al.*, 2015)

$$H_{\text{eff}} = \sum_{i<j} \frac{J_{ij}}{4} (S_+^i S_-^j + S_-^i S_+^j) + \sum_{i,m} V_{i,m} [(2a_m^\dagger a_m + 1) S_z^i - (S_z^i)^2], \quad (37)$$

where  $S_{\pm}^i$  are the spin-1 raising and lowering operators. The pure “XY” or “flip-flop” spin-spin interaction in the first term of Eq. (37) follows the same formula as for generating spin-1/2 Ising interactions in Eq. (22) (Kim *et al.*, 2009)

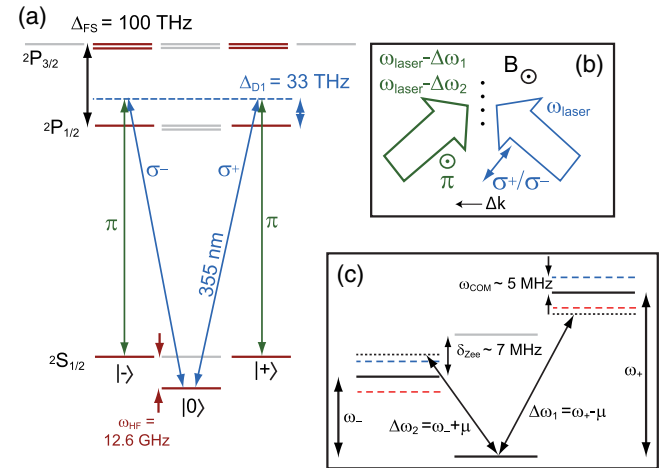


FIG. 20. (a) Level diagram for  $^{171}\text{Yb}^+$  highlighting relevant states for spin-1 physics. (b) Sketch of the experimental geometry showing the directions of the laser wave vectors and the real magnetic field relative to the ion chain. Both beams are linearly polarized, one along the  $\vec{B}$  field (providing  $\pi$  light) and one orthogonal to the  $\vec{B}$  field (providing an equal superposition of  $\sigma^+$  and  $\sigma^-$  light). Multiple beat notes are applied by imprinting multiple frequencies on one beam (in this case, the  $\pi$ -polarized beam). (c) Detailed level diagram of the  $^2S_{1/2}$  ground state showing Raman beat notes in relation to Zeeman splittings and motional sidebands for the center-of-mass mode. Level splittings are not drawn to scale. From Senko *et al.*, 2015.



$$J_{ij} = \Omega_i \Omega_j \sum_m \frac{\eta_{i,m} \eta_{j,m}}{2\delta_m}. \quad (38)$$

As in the case for spin-1/2 interactions, when  $\delta_m > 0$  is larger than transverse mode frequencies,  $J_{ij}$  falls off with distance approximately with a power-law form from Eq. (23), where nearest-neighbor Ising coupling  $J_0$  is typically of the order of  $\approx 1$  kHz and  $\alpha$  can be tuned between 0 and 3 as previously discussed (Porrás and Cirac, 2004; Islam *et al.*, 2013).

The second term in Eq. (37) represents additional spin-phonon terms and is parametrized by the factor  $V_{i,m} = (\eta_{i,m} \Omega_i)^2 / (8\delta_m)$ . For long-range spin-spin interactions with  $\alpha \lesssim 0.5$ , or for small numbers of ions, the  $V_{i,m}$  terms are approximately uniform across the spin chain. In these instances, the  $V_{i,m}$  coefficient can be factored out of the sum over ions in Eq. (37), leaving only global  $S_z^i$  and  $(S_z^i)^2$  terms. For shorter-range interactions or longer chain lengths, the  $V_{i,m}$  terms can be eliminated by adding an additional set of beat frequencies at  $\omega_- - \mu$  and  $\omega_+ + \mu$ , which would generate Ising-type interactions between effective spin-1 particles using the Mølmer-Sørensen gate (Mølmer and Sørensen, 1999).

As theoretically proposed by both Cohen *et al.* (2015) and Gong *et al.* (2016), the previously discussed range of spin-1 phenomena can be accessed in trapped-ion quantum spin simulators. Cohen *et al.* (2015) showed how to generate the full spin-1 XXZ Hamiltonian

$$H = \sum_{i<j} J_{ij} (S_x^i S_x^j + S_y^i S_y^j + \lambda S_z^i S_z^j) + D \sum_i (S_z^i)^2, \quad (39)$$

where the  $S_\gamma^i$  terms are the spin-1 Pauli operators on site  $i$  along the  $\gamma$  direction,  $\lambda$  is the ZZ Ising anisotropy, and  $D$  is analogous to a magnetic field  $B$  term of Eq. (3) for spin-1/2 systems. The interacting terms in Eq. (39) arise from a generalization of the Mølmer-Sørensen gate (Mølmer and Sørensen, 1999) to spin-1 systems, followed by a transformation to the interaction picture; the on-site  $D$  term can be generated by imposing frequency detunings  $D$  on all previous driving fields.

Generating the ground state of the Haldane phase (Haldane, 1983) can be realized by an adiabatic ramp procedure (Cohen *et al.*, 2015). To begin, the spin-1 system can be initialized into

a product state of  $|0\rangle$  on each site, which is the trivial ground state when  $D \gg J$ . Adiabatically reducing  $D$  will then drive the system toward the Haldane phase. As the system size increases and the critical gap between the  $D$  and Haldane phase closes, a symmetry-breaking perturbation can be implemented to circumvent the phase transition. For example, adding a site-specific term  $H_{\text{pert}} = -h \sum_i (-1)^i S_z^i$  will break all symmetries of the Haldane phase, allowing for a finite energy gap along the entire ramp path. The ground state can then be characterized using site-specific measurements to determine the spin correlation functions  $\langle S_\gamma^i S_\gamma^j \rangle$  and the string-order correlation  $\mathcal{S}_{ij}^z \equiv \langle S_z^i S_z^j \prod_{i<k<j} (-1)^{S_k^z} \rangle$ .

Since the interactions  $J_{ij}$  in Eq. (39) are long range, this can lead to both quantitative and qualitative differences in the phase diagram relative to the nearest-neighbor XXZ model (Gong *et al.*, 2016). For instance, the positions of the phase boundaries shift for long-range AFM interactions, whereas long-range FM interactions can destroy the Haldane phase and support a new continuous symmetry-broken phase. Each of these possible phases can be distinguished by comparing the measured values of the previously described spin and string-order correlation functions.

The first experimental steps toward Haldane physics in an ion-trap quantum simulator implemented the model in Eq. (39) with  $\lambda = 0$  (Senko *et al.*, 2015). To generate the ground states of this effective spin-1 XY model, for two- and four-ion spin chains, the spins were initially prepared in the state  $|00 \dots\rangle$ . This is the approximate ground state of Eq. (39) in the presence of a large  $D$  field. This field was then ramped down slowly until  $D \approx 0$ ; the resulting state populations, shown in Fig. 21, match reasonably well with the exactly calculated ground state. Detection of the spin-1 states was accomplished by imaging the spin-dependent fluorescence (Olmschenk *et al.*, 2007) onto an intensified CCD camera and observing which ions were dark, an indication of the presence of the  $|0\rangle$  state. Because both of the  $|\pm\rangle$  states appear bright during the detection process and are scattered into an incoherent mixture of the  $|F = 1\rangle$  states, such a setup does not allow discrimination among all three possible spin states in a single experiment. However, the population of either  $|+\rangle$  or  $|-\rangle$  can be measured by repeating the experiment and applying a  $\pi$  rotation to the appropriate  $|0\rangle \leftrightarrow |\pm\rangle$  transition before the

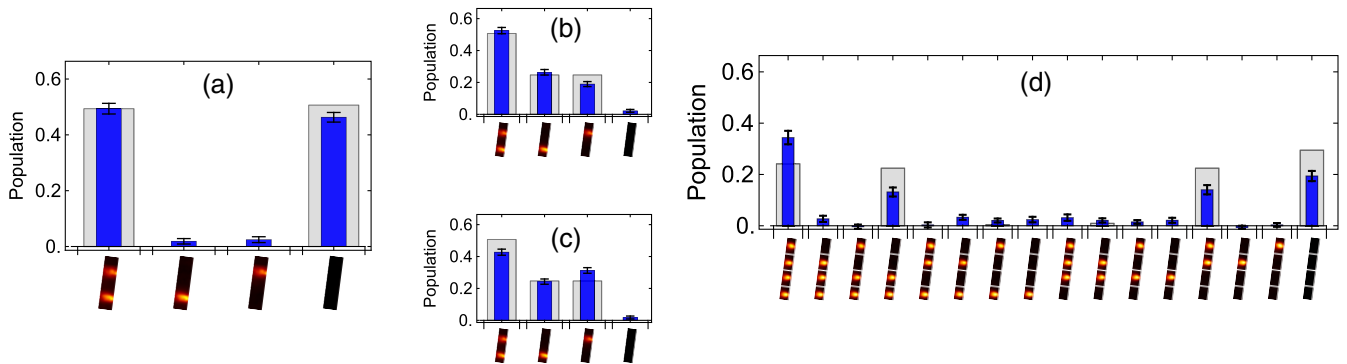


FIG. 21. Measurements of the prepared (a)–(c) two-spin and (d) four-spin states after ramping an  $S_z^2$  field (narrow blue bars) compared to the values expected for the calculated ground state (gray bars). (a)–(c) Measured populations when the dark state is set at  $|0\rangle$ ,  $|-\rangle$ , or  $|+\rangle$ , respectively. The dark state is set at  $|0\rangle$  in (d). Adapted from Senko *et al.*, 2015.

fluorescence imaging. For instance, measuring an ion in the dark state after a  $\pi$  pulse between  $|0\rangle \leftrightarrow |+\rangle$  indicates that the spin was in the  $|+\rangle$  state before detection. This binary discrimination is not a fundamental limit to future experiments, since populations could be “shelved” into atomic states that do not participate in the detection cycle (Christensen *et al.*, 2020).

Measurements of populations in the  $S_z$  basis necessarily discard phase information about components of the final state. This can be important in many spin models, including the  $XY$  model, where such measurements alone cannot discriminate between different eigenstates. For example, the ground state of an  $XY$  model with two spin-1 particles is  $|00\rangle/\sqrt{2} - (|-\rangle|+\rangle + |+\rangle|-\rangle)/2$ , while the highest excited state is  $|00\rangle/\sqrt{2} + (|-\rangle|+\rangle + |+\rangle|-\rangle)/2$ , differing only by a relative phase. Senko *et al.* (2015) verified ground-state production by employing a modified parity entanglement witness procedure (Sackett *et al.*, 2000). First, global  $\pi/2$  rotations were applied on both the  $|0\rangle \leftrightarrow |+\rangle$  and  $|0\rangle \leftrightarrow |-\rangle$  transitions, with a relative phase  $\varphi$ . Then parity  $\Pi(\varphi) = \sum_{n=0}^2 (-1)^n P_n$  of the number of spins in state  $|0\rangle$  was measured, where  $P_n$  is the probability of  $n$  spins appearing in state  $|0\rangle$ . This is expected to result in  $\Pi(\varphi) = 3/8 \pm (1/2) \cos \varphi$ , where  $+$  and  $-$  correspond to the ground and highest excited states, respectively. The data shown in Fig. 22 show the phase of the parity oscillations to be consistent with having prepared the two-spin ground state of the spin-1  $XY$  model.

#### IV. NONEQUILIBRIUM PHASES OF MATTER AND DYNAMICS

Trapped-ion simulators are well suited for studying nonequilibrium phenomena, as well as the equilibrium properties discussed in Sec. III. Nonequilibrium dynamics might even be considered more natural, since the study of equilibriumlike

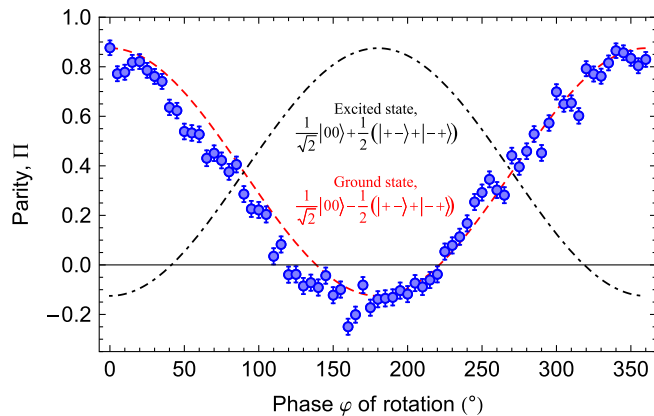


FIG. 22. Following an adiabatic ramp, the parity of the final state is measured as a function of the final rotation phase  $\varphi$  as a witness for spin-1 entanglement (see the text for rotation protocol). The dashed and dot-dashed lines represent the theoretically expected values for the ground state  $[|00\rangle/\sqrt{2} - (|-\rangle|+\rangle + |+\rangle|-\rangle)/2]$  and the highest excited state  $[|00\rangle/\sqrt{2} + (|-\rangle|+\rangle + |+\rangle|-\rangle)/2]$ , respectively. The amplitude and phase of the measured oscillation reveal that the prepared state are consistent with the expected ground state. From Senko *et al.*, 2015.

properties requires a specific protocol for preparing the corresponding ground or thermal state, unlike conventional condensed matter materials that directly thermalize through phonon interactions. The simplest nonequilibrium studies, on the other hand, can start with an initial product state and then simply evolve the system under a time-dependent Hamiltonian of interest.

Trapped-ion quantum simulators allow for the study of nonequilibrium dynamics over a broad range of both spatial and temporal resolution. The effective long-range spin-spin interactions described in Sec. I.C.2 can be modulated in time by turning the laser-ion interactions on or off. This allows nonequilibrium states to be prepared via quenches or stroboscopic application of the Ising Hamiltonian, while their subsequent dynamics are observed over timescales both shorter and longer than the natural timescale of interactions  $1/J_{ij}$ . Single spin resolution can be achieved even as the system size is scaled to many particles, allowing access to nontrivial observables such as spin-spin correlations and magnetic domain sizes. Since strongly interacting and highly frustrated Ising spin models are often employed in analytical and numerical studies of nonequilibrium quantum dynamics, the results of trapped-ion spin simulations serve as an important benchmark for these theoretical predictions.

Perhaps the most natural nonequilibrium experiments are global and local quenches. In a global quench experiment, a simple initial state evolves under a time-independent Hamiltonian. A global quench originates from situations where the simple initial state can be naturally thought of as the ground state of some simple Hamiltonian, in which case the dynamics ensues when the Hamiltonian is changed (quenched). A local quench allows for the comparison of the nonequilibrium dynamics between two initial states that differ by the application of a locally applied unitary operation. A particular example of a local quench is a situation where one of the two initial states is an eigenstate of the Hamiltonian.

Short-time spin dynamics over timescales of up to  $1/J_{ij}$  allows for investigation of the quantum information propagation across the system discussed in Sec. IV.A. Longtime dynamics well beyond  $1/J_{ij}$ , on the other hand, can indicate whether the system eventually approaches some effective steady state and, if so, how this steady state is approached. Effective thermalization is often expected, even in a closed system of spins where a subset of the spin system uses its complement as the bath (D’Alessio *et al.*, 2016). However, as discussed in Sec. IV.B, disorder can often prevent such thermalization, leading to many-body localization. Similarly, as discussed in Sec. IV.C, even in cases where the system eventually thermalizes, it is possible that dynamics dramatically slows and actual thermalization takes a long time to occur, in a phenomenon known as prethermalization.

There are many forms of inducing and probing spin dynamics in trapped-ion systems. One example is the periodic modulation of a Hamiltonian, which gives rise to stroboscopic Floquet dynamics. In Sec. IV.D, we discuss such dynamics in trapped-ion systems in two complementary contexts. The first focuses on the application of a Hamiltonian and its negative counterpart in order to measure so-called out-of-time-ordered correlation (OTOC) functions. The second focuses on the

spontaneous breaking of discrete time-translation symmetry, leading to the emergence of time crystalline order.

### A. Information propagation

Many properties of a many-body quantum system depend on how quickly quantum information can propagate in that system. Indeed, the speed of a quantum computation through an array of qubits is boosted by sending quantum information faster across the array. Similarly, fast information propagation through qubits may allow for faster preparation of highly entangled states of the array. With its tunable approximately-power-law-decaying interactions, a trapped-ion chain is an ideal test bed for studying how much such long-range interactions can speed up quantum information propagation relative to nearest-neighbor interactions and for elucidating the implications of such speedups.

To make connection with the native interactions in trapped-ion spin crystals, we assume that the interactions fall off with distance as a power law  $J_0/|i-j|^\alpha$  between ions  $i$  and  $j$ , with  $0 \leq \alpha \leq 3$ , as derived in Eq. (23) and previously discussed. For the purposes of studying the bounds on the speed of information propagation, it is convenient to express the spin Hamiltonian in the following general form:

$$H = \sum_{i < j} h_{ij} + \sum_i h_i, \quad (40)$$

where  $h_i$  is a Hamiltonian acting on spin  $i$  and where the two-spin Hamiltonian  $h_{ij}$  acting on spins  $i$  and  $j$  is subject to the bound

$$\|h_{ij}\| \leq \frac{J_0}{|i-j|^\alpha}. \quad (41)$$

Here  $\|O\|$  indicates the operator (or spectral) norm of operator  $O$  or the magnitude of its largest absolute eigenvalue. We are interested in studying how quickly quantum information can propagate when the system evolves unitarily under Eq. (40). Various notions of information propagation can be defined, depending on the problem (Tran, Chen *et al.*, 2020).

We first focus on the dynamics following a local quench (Jurcevic *et al.*, 2014). Let  $B$  be a unitary operator acting on a single site, and let  $A$  be a single-site observable acting on another site a distance  $r$  away. Let  $|\psi\rangle$  be an arbitrary initial state, and let  $A(t)$  be the Heisenberg evolution of  $A$  under the Hamiltonian  $H$  in Eq. (40). Then the effect on observable  $A$  due to the disturbance  $B$  can be defined as the difference between the expectation values of  $A(t)$  in the original state  $|\psi\rangle$  and in the quenched state  $B|\psi\rangle$ ,

$$\begin{aligned} & |\langle \psi | B^\dagger A(t) B | \psi \rangle - \langle \psi | A(t) | \psi \rangle| \\ &= |\langle \psi | B^\dagger [A(t), B] | \psi \rangle| \leq \|[A(t), B]\|. \end{aligned} \quad (42)$$

The signal after time  $t$  a distance  $r$  away is thus bounded by the unequal-time commutator  $\|[A(t), B]\|$ . Intuitively, the operator  $A(t)$  can be thought to originate on a given site at  $t=0$  (and commuting with operator  $B$  on another site at distance  $r$  away) and then spread in time until its support significantly overlaps with the support of  $B$  and thus allows for a substantial commutator  $\|[A(t), B]\|$ .

Upper bounds on  $\|[A(t), B]\|$  subject to the Hamiltonian in Eq. (40) are referred to as Lieb-Robinson-type bounds, named after the original work considering nearest-neighbor interactions ( $\alpha = \infty$ ) (Lieb and Robinson, 1972). The region in the  $r$ - $t$  plane outside of which  $\|[A(t), B]\|$  must be small is called the causal region, while its boundary is called the effective light cone. While the Hamiltonian in Eq. (40) is time independent, Lieb-Robinson bounds also hold for time-dependent  $h_{ij}$  subject to Eq. (41) and for arbitrary time-dependent  $h_i$ . A growing body of theoretical literature places upper bounds on  $\|[A(t), B]\|$  and therefore derives tighter and tighter light cones for different values of  $\alpha$  (Hastings and Koma, 2006; Lashkari *et al.*, 2013; Gong *et al.*, 2014a; Foss-Feig *et al.*, 2015; Storch, Worm, and Kastner, 2015; Matsuta, Koma, and Nakamura, 2017; Tran, Ehrenberg *et al.*, 2019; Tran, Guo *et al.*, 2019; Chen and Lucas, 2019; Guo *et al.*, 2019; Sweke, Eisert, and Kastner, 2019; Else *et al.*, 2020; Kuwahara and Saito, 2020; Tran, Chen *et al.*, 2020). At the same time, a complementary growing body of theoretical literature considers specific Hamiltonians and protocols demonstrating larger and larger causal regions (Kastner, 2011; Bachelard and Kastner, 2013; Eisert *et al.*, 2013; Hauke and Tagliacozzo, 2013; Hazzard *et al.*, 2013, 2014; Jünemann *et al.*, 2013; Knap *et al.*, 2013; Schachenmayer *et al.*, 2013; Worm *et al.*, 2013; Gong *et al.*, 2014a; Nezhadhighi and Rajabpour, 2014; Cevolani, Carleo, and Sanchez-Palencia, 2015; Rajabpour and Sotiriadis, 2015; Storch, Worm, and Kastner, 2015; Buyskikh *et al.*, 2016; Cevolani, Carleo, and Sanchez-Palencia, 2016; Maghrebi *et al.*, 2016; Van Regemortel, Sels, and Wouters, 2016; Eldredge *et al.*, 2017; Lepori, Trombettoni, and Vodola, 2017; Cevolani *et al.*, 2018; Chen, Zhou, and Xu, 2018; Frérot, Naldesi, and Roscilde, 2018; Chen and Zhou, 2019; Guo *et al.*, 2019; Kloss and Bar Lev, 2019; Luitz and Lev, 2019). These works have culminated in the establishment of provably tight (up to subpolynomial corrections) light cones for all  $\alpha > d$ , where  $d$  is the dimension of the system:  $t \gtrsim \log r$  for  $\alpha \in (d, 2d]$  (Hastings and Koma, 2006; Tran, Deshpande *et al.*, 2020),  $t \gtrsim r^{\alpha-2d}$  for  $\alpha \in (2d, 2d+1)$  (Chen and Lucas, 2019; Tran, Deshpande *et al.*, 2020), and  $t \gtrsim r$  for  $\alpha \in [2d+1, \infty)$  (Chen and Lucas, 2019; Kuwahara and Saito, 2020; Tran, Chen *et al.*, 2020).

Thanks to Eq. (42), Lieb-Robinson bounds on  $\|[A(t), B]\|$  directly constrain information propagation after local quenches. A local-quench experiment on a trapped-ion chain has realized the XY model of hopping hard-core bosons corresponding to  $h_i = 0$  and  $h_{ij} = J_{ij}/|i-j|^\alpha (\sigma_i^+ \sigma_j^- + \sigma_i^- \sigma_j^+)$  in Eq. (40) (Jurcevic *et al.*, 2014). Figure 23 shows results for a local quench on 15 spins from the experiment. After flipping up the middle spin (corresponding to  $B = \sigma_8^x$ ) in a chain of down spins, the experiment measures  $A = \sigma_i^z$  for various  $i$ . Since the number of flipped spins is conserved during the time evolution, the evolution in this restricted Hilbert space of spins is well described using the language of single-flip eigenstates called magnons.

Information propagation can also be studied in global quench experiments, where connected correlations are measured as a simple initial state (such as a product state) evolves under a given Hamiltonian. Linear light-cone-like spreading of such correlations due to a nearest-neighbor Hamiltonian

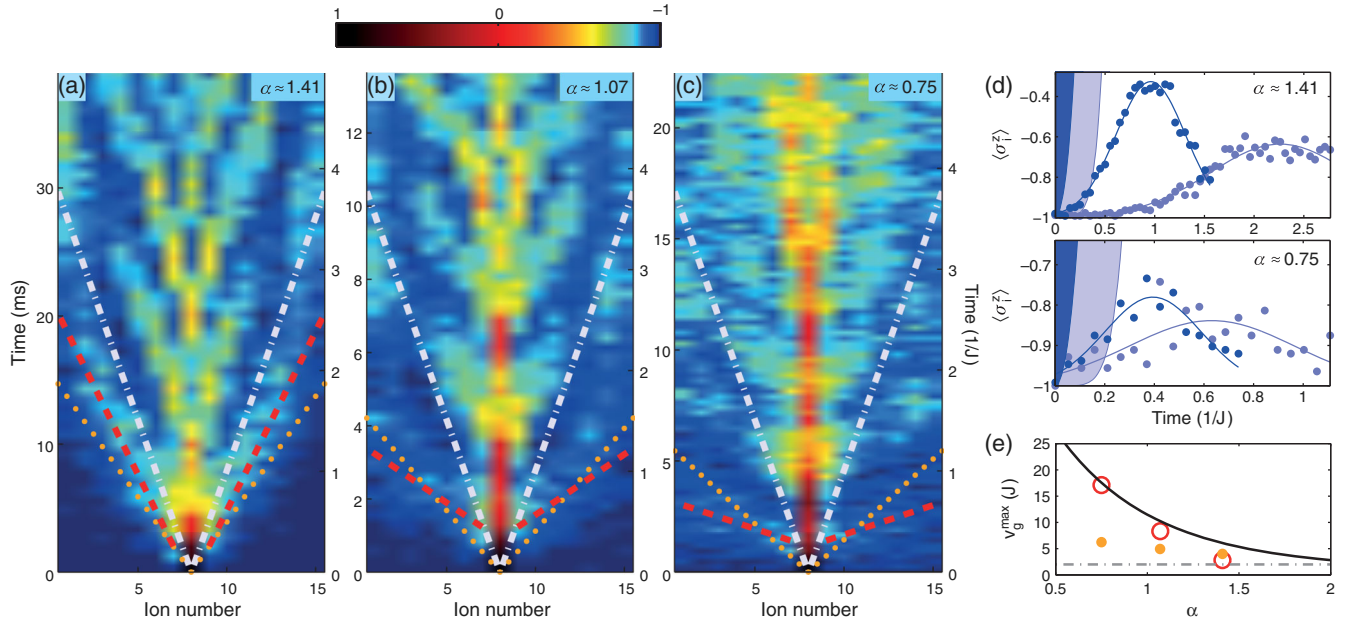


FIG. 23. (a)–(c) Measured magnetization  $\langle \sigma_i^z(t) \rangle$  (color coded) following a local quench. From (a) to (c), the interaction ranges are  $\alpha \approx 1.41, 1.07, 0.75$ . In (a), an effective light cone is evident and the dynamics is approximately described by nearest-neighbor interactions only. Red lines, fits to the observed magnon arrival times [examples shown in (d)]; white lines, light cone for averaged nearest-neighbor interactions; orange dots, fits after renormalization by the algebraic tail. (b),(c) As the interaction range is increased, the light cone disappears and nearest-neighbor models fail to capture the dynamics. (d) Magnetization of spins (ions) 6 and 13 from (a) (top panel) and (c) (bottom panel). Solid lines, Gaussian fits to measured magnon arrival. Top panel: for  $\alpha = 1.41$ , a nearest-neighbor Lieb-Robinson bound captures most of the signal (shaded region). Bottom panel: for  $\alpha = 0.75$ , the bound does not. (e) Maximum group velocity. With increasing  $\alpha$ , the measured magnon arrival velocities (solid circles) approach the group velocity of the nonrenormalized nearest-neighbor model (gray dash-dotted line). If renormalized by the algebraic tail, the nearest-neighbor group velocity increases at small  $\alpha$  (open circles), but much less than the increase of the observed magnon velocity. For small  $\alpha$ , the measured arrival times are consistent with the divergent behavior predicted for full power-law interactions (black line). Adapted from [Jurcevic \*et al.\*, 2014](#).

was first measured in neutral atoms confined in an optical lattice ([Cheneau \*et al.\*, 2012](#)). For long-range interacting systems such as trapped-ion spins, the spread of correlations may no longer be confined within a linear light cone. In particular, suppose that the system starts in an initial product state  $|\psi\rangle$  and evolves under the Hamiltonian in Eqs. (40) and (41). At time  $t = 0$ , the connected correlation function  $C_{ij}(t) = \langle O_i(t)O_j(t) \rangle - \langle O_i(t) \rangle \langle O_j(t) \rangle$  (where the operator  $O_i$  acts on site  $i$ ) vanishes since the first expectation value factorizes. As time goes on, the support of  $O_i(t)$  and  $O_j(t)$  grows, making  $C_{ij}(t)$  grow in return. For the case of short-range interactions,  $C_{ij}(t)$  is bounded in the  $r$ - $t$  plane (where  $r = |i - j|$ ) by a linear light cone similar to the corresponding light cone for the unequal-time commutator  $\|[A(t), B]\|$  ([Bravyi, Hastings, and Verstraete, 2006](#)). For general  $\alpha$ , a bound on  $\|[A(t), B]\|$  can also be used to derive a bound on  $C_{ij}(t)$  ([Gong \*et al.\*, 2014b](#); [Tran, Chen \*et al.\*, 2020](#)), but the relationship between the two light cones is not as trivial as in the nearest-neighbor ( $\alpha = \infty$ ) case. However, the physical picture is similar: the Lieb-Robinson bound constrains the spread of operators  $O_i(t)$  and  $O_j(t)$ , so if the support of  $O_i(t)$  [ $O_j(t)$ ] has not spread significantly outside of a ball of radius  $r/2$  around  $i$  ( $j$ ), then  $O_i(t)$  and  $O_j(t)$  have approximately disjoint supports, leading to small  $C_{ij}(t)$ .

Connected correlations following a global quench were measured in a chain of trapped ions ([Richerme \*et al.\*, 2014](#)).

[Richerme \*et al.\*](#)'s experiment also studied the XY model corresponding to  $h_i = 0$  and  $h_{ij} = J_{ij}/|i - j|^\alpha (\sigma_i^x \sigma_j^x + \sigma_i^z \sigma_j^z)$  in Eq. (40). Figure 24 shows data on ten ions following a global quench. Starting with an initial state of all spins pointing down (in the  $z$  basis), the experiment measures the time evolution of connected correlations  $C_{ij}(t) = \langle \sigma_i^z(t) \sigma_j^z(t) \rangle - \langle \sigma_i^z(t) \rangle \langle \sigma_j^z(t) \rangle$ . The growth of connected correlations following a global quench may also be accompanied by the growth of entanglement, as was observed experimentally by [Friis \*et al.\* \(2018\)](#).

Experiments on ultracold polar molecules ([Yan \*et al.\*, 2013](#)) and solid-state defect centers ([J. Choi \*et al.\*, 2017](#)) have not yet had the single-spin resolution necessary for studying the shape of the causal region after local or global quenches in long-range-interacting systems. On the other hand, experiments on ultracold neutral atoms interacting via Rydberg-Rydberg interactions ([Bernien \*et al.\*, 2017](#); [Zeicher \*et al.\*, 2017](#); [Guardado-Sanchez \*et al.\*, 2018](#); [Lienhard \*et al.\*, 2018](#)) should be able to access the interesting parameter regime of  $\alpha = 3$  (dipolar interactions) ([de Léséleuc \*et al.\*, 2019](#)) in one, two, and three spatial dimensions.

## B. Disorder-induced localization

Many-body localization (MBL) has become one of the most studied nonequilibrium phases of matter, receiving

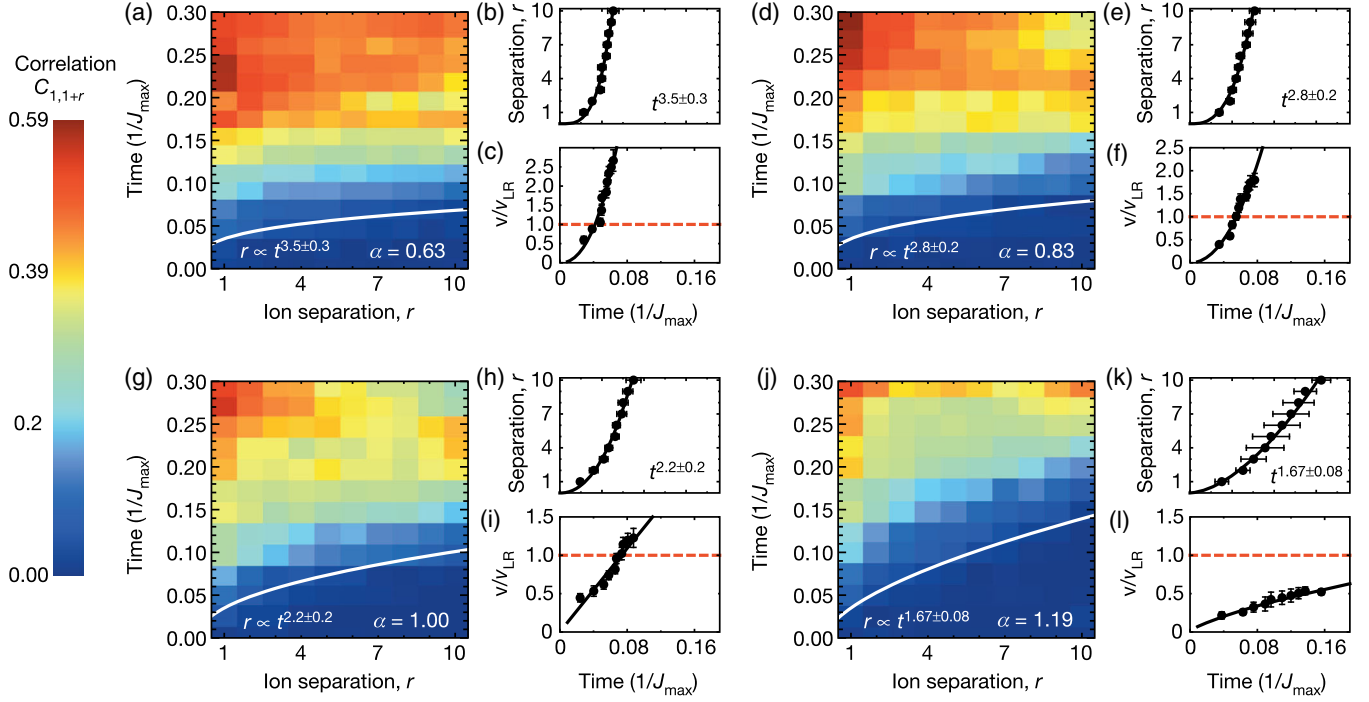


FIG. 24. (a) Spatial and time-dependent correlations, (b) extracted light-cone boundary (chosen as the contour  $C_{ij} = 0.04$ ), and (c) correlation propagation velocity following a global quench of a long-range XY model with  $\alpha = 0.63$ . The curvature of the boundary shows (b) an increasing propagation velocity, quickly exceeding (c) the short-range Lieb-Robinson velocity bound  $v_{\text{LR}}$ . Solid lines give a power-law fit to the data that slightly depends on the choice of contour  $C_{i,j}$ . Complementary plots for (d)–(f)  $\alpha = 0.83$ , (g)–(i)  $\alpha = 1.00$ , and (j)–(l)  $\alpha = 1.19$ . As the range of the interactions decreases, correlations do not propagate as quickly through the chain. (j)–(l) For the shortest-range interaction, the experiment demonstrates a faster-than-linear growth of the light-cone boundary despite having  $\alpha > 1$ . Error bars, 1 s.d. Adapted from Richerme *et al.*, 2014.

considerable scrutiny in both experiment and theory in the past decade (Oganesyan and Huse, 2007; Nandkishore and Huse, 2015; Schreiber *et al.*, 2015; Choi *et al.*, 2016; Abanin *et al.*, 2019). The localization effect is a generalization of single-particle Anderson localization, which is characterized by a cessation of quasiparticle transport in noninteracting systems subject to a random potential landscape (Anderson, 1958). In the case of MBL similar insulatorlike properties are observed even when particles are strongly interacting (Oganesyan and Huse, 2007; Nandkishore and Huse, 2015; Abanin *et al.*, 2019). When prepared with a quench, the quantum states become highly entangled many-body superpositions of excited eigenstates spanning the entire energy spectrum of the disordered system Hamiltonian. MBL can be distinguished from Anderson localization by the logarithmic growth of entanglement entropy at long times (Bardarson, Pollmann, and Moore, 2012). The distribution of eigenstates occupied in a MBL phase is decidedly non-thermal and a number of observables have been identified to characterize phase transitions between MBL and thermal states when varying the interaction strength or disorder in the Hamiltonian (Serbyn *et al.*, 2014; Luitz, Laflorencie, and Alet, 2015; Nandkishore and Huse, 2015; Abanin *et al.*, 2019).

Signatures of MBL were observed in a trapped-ion quantum simulator by both Smith *et al.* (2016) and Brydges *et al.* (2019) by engineering a locally disordered but programmable potential ( $H_D$ ) that was applied simultaneously with an

effective long-range-interacting transverse-field Hamiltonian (see Sec. I.C)

$$H_{\text{MBL}} = \sum_{i<j} J_{ij} \sigma_i^x \sigma_j^x + \frac{B}{2} \sum_i \sigma_i^z + H_D. \quad (43)$$

The disordered potential is implemented with single-site resolution across the ion chain such that

$$H_D = \sum_i D_i \sigma_i^z, \quad (44)$$

where  $D_i$  is sampled from a uniform distribution  $D_i \in [-W/2, W/2]$  with width  $W$ . For finite system sizes, this Hamiltonian exhibits features consistent with many-body localization and demonstrates a disorder-induced, long-lived memory of the system's initial conditions (Hauke and Heyl, 2015; Maksymov *et al.*, 2017). Understanding the thermodynamic stability of localization with power-law interactions remains an open problem (Burin, 2006, 2015; Yao *et al.*, 2014; Nandkishore and Sondhi, 2017).

In both experiments, the MBL state is created by initially preparing the ten-spin Néel state with staggered order ( $|\psi_0\rangle = |\downarrow\uparrow\downarrow\uparrow\downarrow\uparrow\downarrow\uparrow\downarrow\uparrow\rangle_z$ ), which is highly excited with respect to the disordered Ising Hamiltonian in Eq. (43). This Hamiltonian is rapidly quenched on and the resulting single-spin magnetization dynamics  $\langle\sigma_i^z(t)\rangle$  is measured for times of up to  $t = 10/J_0$ . The experiment is repeated under

multiple instances of disorder with Stark shifts ( $D_i$ ) applied programmatically to each ion using a rastered individual addressing laser (Lee *et al.*, 2016). This individual addressing laser is also used to create the initial Néel state using a sequence of controlled spin flips.

In the absence of disorder these initial spin states thermalize if the uniform transverse field  $B$  is sufficiently large (Deutsch, 1991; Srednicki, 1994; Rigol, Dunjko, and Olshanii, 2008). Smith *et al.* (2016) used global rotations to prepare eigenstates of both  $\sigma^x$  and  $\sigma^z$  and measure the resulting single ion magnetization projected in those directions after evolution under  $H_{\text{MBL}}$ . In the case of a thermalizing system, memory of the initial spin configuration is lost in all directions of the Bloch sphere, namely,  $\langle \sigma_i^x \rangle = \langle \sigma_i^z \rangle = 0$  at long times. Above the threshold transverse field ( $B \gtrsim 4J_0$ ) the system rapidly thermalizes to zero magnetization after relatively short time-scales ( $t < 5/J_0$ ) [Fig. 25(a)].

However, with the transverse field held fixed at  $B = 4J_0$ , the data show that applied disorder localizes the spin chain, retaining memory of the initial Néel state in measurements of the  $z$  magnetization  $\langle \sigma_i^z \rangle$  [Fig. 25(b)]. Each measurement of magnetization dynamics for disorder width  $W$  is repeated, with at least 30 different realizations of disorder that are subsequently averaged together. This is sufficient to reduce the finite depth disorder sampling error to be of the same order as other noise sources. After some initial decay and

oscillations, the magnetization of each spin settles to a steady-state value for  $J_0 t \geq 5$ . The degree of localization can be quantified using the normalized Hamming distance

$$\begin{aligned} \mathcal{D}(t) &= \frac{1}{2} - \frac{1}{2N} \sum_i \langle \sigma_i^z(t) \sigma_i^z(0) \rangle \\ &= \frac{1}{2} - \frac{1}{2N} \sum_i (-1)^i \langle \sigma_i^z(t) \rangle. \end{aligned} \quad (45)$$

This observable counts the number of spin flips from the initial state, normalized to the length of the spin chain. At long times, a randomly oriented thermal state shows  $\mathcal{D} = 0.5$ , while one that remains fully localized has  $\mathcal{D} = 0$  [Fig. 25(c)].

The average steady-state value  $\langle \mathcal{D}(t) \rangle$  for  $J_0 t \geq 5$  can serve as an order parameter to display the crossover between the localizing and thermalizing regimes. The most relevant adjustable experimental control parameters for probing the MBL phase diagram are the amplitude of disorder  $W$  and the interaction range  $\alpha$ . Increasing  $W$  pins each spin closer to its initial state and pushes the entire spin chain toward a localized regime [Fig. 25(d)]. Likewise, the localization strengthens as  $\alpha$  is increased toward shorter-range interactions [Fig. 25(e)], recovering Anderson localization via a Jordan-Wigner transformation (Jordan and Wigner, 1928) in the  $\alpha \rightarrow \infty$  limit. Numerical studies have confirmed that full localization occurs

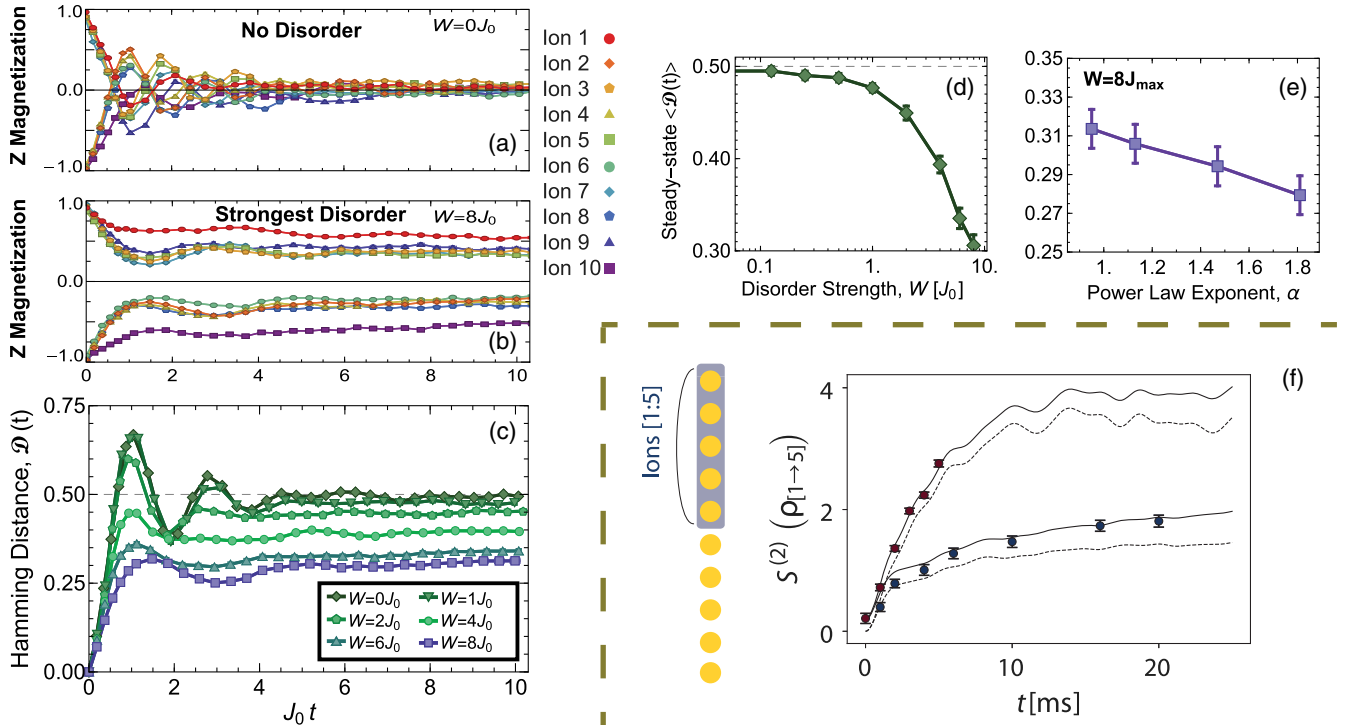


FIG. 25. Many-body localization. (a),(b) Temporal dynamics for each of the ten ions'  $z$  magnetizations  $\langle \sigma_i^z(t) \rangle$  in the case of zero disorder and strong disorder for (a) and (b), respectively. (c) The normalized Hamming distance  $\mathcal{D}(t)$  has plateaued to a steady-state value for  $J_0 t \geq 5$  at all measured disorder strengths. (d) The time-averaged steady-state value  $\langle \mathcal{D}(t) \rangle$  after the plateau shows the onset of a crossover between a thermalizing regime [ $\langle \mathcal{D}(t) \rangle = 0.5$ ] and a localizing regime [ $\langle \mathcal{D}(t) \rangle = 0$ ] as disorder increases. (e) The steady-state Hamming distance increases with longer-range interactions. (f) The half-chain entropy growth in the absence of disorder (red points) and for a disordered chain with  $W = 6J_0$  (blue points), compared with numerical simulations of unitary dynamics (dotted lines) and including known sources of decoherence (solid lines). (a)–(e) Adapted from Smith *et al.*, 2016. (f) Adapted from Brydges *et al.*, 2019.

within experimentally accessible disorder strengths and interaction ranges (Wu and Das Sarma, 2016).

The slow growth of entanglement entropy ( $S$ ) has long been understood as a distinguishing feature of localization (Bardarson, Pollmann, and Moore, 2012). A short-range interacting MBL state should exhibit a slower entanglement growth rate than interacting quantum states without disorder, where entanglement spreads ballistically. The dynamics of the entanglement entropy are also quite different for noninteracting Anderson localized systems, where the entanglement saturates at short times once the system's dynamics have reached the localization length (Abanin *et al.*, 2019). In a trapped-ion quantum simulator with algebraically decaying interactions the entanglement entropy of an MBL state should also grow algebraically ( $S \sim t^q$ ), but with  $q < 1$  the dynamics are still distinct from those of nonlocalized or Anderson localized systems (Pino, 2014).

It is generally difficult to measure entanglement entropy in quantum simulators due to the exponential system-size scaling of the number of measurements required for full state tomography. Smith *et al.* (2016) used the observed slow growth in quantum-Fisher information as a proxy for half-chain entanglement entropy, motivated by a similar scaling with disorder and interaction strength as observed in numerical simulations. A more direct measurement was made by Brydges *et al.* (2019), who developed a technique to probe the second-order half-chain Rényi entanglement entropy in their ten-ion quantum simulator [ $S^{(2)}(\rho_{[1 \rightarrow 5]})$ ] using randomized measurements. They found the entanglement growth to be significantly suppressed in the presence of strong disorder, which was in good agreement with numerical predictions [Fig. 25(f)].

Anderson localization can be explored using the same long-range disordered Hamiltonian, even though it is not strictly noninteracting, by observing the dynamics of a single-spin excitation in the ion chain. For example, Maier *et al.* (2019) observed the transport efficiency of a spin excitation from the initial site  $i = 3$  to the target site  $i = 8$  as a function of time in a ten-ion spin chain [Fig. 26(a)]. The evolution of this single-spin excitation can be described by an XY model Hamiltonian

$$H = \sum_{i \neq j} J_{ij} (\sigma_i^+ \sigma_j^- + \sigma_i^- \sigma_j^+) + \sum_i [B_i + W_i(t)] \sigma_i^z, \quad (46)$$

where the disorder field contains single-site static ( $B_i$ ) and time-dependent [ $W_i(t)$ ] components [Fig. 26(b)]. In the absence of disorder, the XY interaction term in this Hamiltonian conserves the total magnetization of the system, allowing a single-spin excitation to hop around the chain. The transport efficiency on site  $i = 8$  is then quantified by integrating the instantaneous probability of the excitation appearing on spin 8,

$$\eta_8 \equiv \int_0^{t_{\max}} \frac{\langle \sigma_8^z(t) \rangle + 1}{2} dt, \quad (47)$$

over the full duration of the experiment  $t_{\max}$ .

The transport efficiency is reduced in the presence of strong static disorder ( $B_{\max} > J_0$ ), consistent with Anderson localization of the initial spin excitation (Fig. 26, main panel).

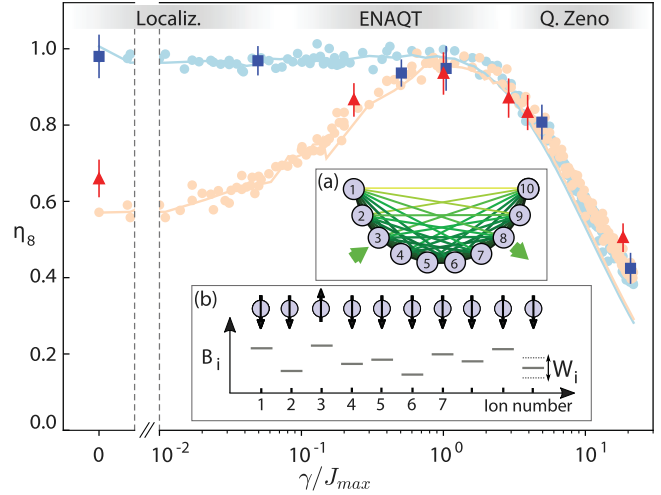


FIG. 26. Breakdown of Anderson localization. Main panel: transport efficiency  $\eta_8$  to the target (ion 8) under different strengths of static disorder (blue,  $B_{\max} = 0.5J_0$ ; red,  $B_{\max} = 2.5J_0$ ) and Markovian-like dephasing with rate  $\gamma$ . Experimental points (shown as dark squares and triangles) result from averaging over 20–40 random realizations of disorder and noise, with 25 experimental repetitions each. The regimes of localization, ENAQT (Rebentrost *et al.*, 2009), and the quantum Zeno effect are indicated in gray. The data agree well with theoretical simulations of the coin-tossing random process (light bullets) realized in the experiment, while simulations with ideal Markovian white noise (lines) underestimate ENAQT at large  $\gamma$ . (a) Sketch of the transport network. The ions experience a long-range coupling, with darker and thicker connections indicating higher coupling strengths. The green arrows denote the source (3) and the target (8) for the excitation in the ion network. (b) Sketch of the ion chain representing interacting spin-1/2 particles as circles, with the spin states denoted by arrows. The ions are subject to random static and dynamic on-site excitation energies, indicated by  $B_i$  and  $W_i(t)$ . From Maier *et al.*, 2019.

However, adding temporal variations in the form of white dephasing noise in  $W_i(t)$  destroys the localization, a phenomenon known as environment-assisted quantum transport (ENAQT) (Rebentrost *et al.*, 2009). The spectral density of the Markovian-like noise [ $S(\omega) \propto W_{\max}^2$ ] in  $W_i(t)$  determines the rate of dephasing  $\gamma = S(\omega)$ . This experiment can access regimes where transport is inhibited by either Anderson localization ( $\gamma < J_0$ ) or the quantum Zeno effect ( $\gamma > J_0$ ). In the ENAQT regime, when  $\gamma \approx J_0$  the temporal noise modifies the destructive interference necessary for Anderson localization and transport is revived. Section IV.D further explores experiments studying trapped-ion spin dynamics under the influence of both static disorder and a periodically time-varying Hamiltonian.

Many-body localization is a unique case in which a closed quantum system remains nonergodic and localized even up to infinite times. The trapped-ion quantum simulations given by Smith *et al.* (2016) and Brydges *et al.* (2019) were limited by finite experimental coherence times to only one decade in  $J_0 t$ . This makes it difficult for these experiments to quantify how long lived the magnetization or slow the entanglement growth might be. Other experiments that have studied MBL using

cold neutral atoms can achieve several orders of magnitude longer evolution time relative to their interaction timescale. For example, MBL can be realized using cold fermions in quasirandom 1D optical lattices (Schreiber *et al.*, 2015; Lüschen, Bordia, Scherg *et al.*, 2017; Kohlert *et al.*, 2019; Lukin *et al.*, 2019), verifying MBL-like behavior in a variety of Hubbard Hamiltonians. This system has also been used to confirm the breakdown of MBL in open quantum systems (Bordia *et al.*, 2016; Lüschen, Bordia, Hodgman *et al.*, 2017). Moreover, experiments have started to probe whether MBL can exist in systems with dimensionality  $> 1$  (Kondov *et al.*, 2015; Choi *et al.*, 2016; Bordia *et al.*, 2017), where the stability of MBL is still an open question (De Roeck and Imbrie, 2017). Other experimental platforms have used novel metrics to probe many-body localization, including many-body spectroscopy (Roushan *et al.*, 2017), measurement of out-of-time-order correlators (Wei, Ramanathan, and Cappellaro, 2018) (see Sec. IV.D), and performance of full state tomography to compute entanglement entropy (Xu *et al.*, 2018).

### C. Prethermalization

Hamiltonians that support MBL are believed to be non-ergodic, even after evolution times that are exponentially long in system size (Nandkishore and Huse, 2015). There are also systems that are nonergodic for a shorter amount of time (but often still much longer than the coherence time of typical quantum simulation experiments) before eventually thermalizing. These systems are not usually disordered and can be described by models of weakly interacting (quasi)particles, such as 1D Bose gases (Kinoshita, Wenger, and Weiss, 2006; Gring *et al.*, 2012; Langen *et al.*, 2015). The generic behavior of such a system is called prethermalization, meaning that the system relaxes to a quasistationary state other than the thermal state before thermalizing eventually. The prethermal quasistationary state is usually believed to be described by a generalized Gibbs ensemble (GGE) (Rigol *et al.*, 2007) that corresponds to the model of quasiparticles without the weak interactions. Such a state will have a partial memory of the initial state, because the quasiparticle occupation numbers are conserved if interactions are ignored. At sufficiently long times, the weak interactions are expected to break the integrability of the system and lead to thermalization in the end. This picture of prethermalization has been well studied in both theory (Berges, Borsányi, and Wetterich, 2004; Manmana *et al.*, 2007; Polkovnikov *et al.*, 2011) and experiment (Gring *et al.*, 2012; Langen *et al.*, 2015).

In a programmable ion-trap quantum simulator, owing to long-range spin interactions new types of prethermalization can occur with prethermal states not described by a standard GGE. A sample study was first proposed theoretically (Gong and Duan, 2013) and later demonstrated experimentally (Neyenhuis *et al.*, 2017). The central idea is that, with sufficiently long-range interactions, a nondisordered and homogeneous system can have a strong emergent inhomogeneity due to the open boundary condition of an experimental spin chain. This emergent inhomogeneity can lead to trapping of quasiparticles before the system relaxes to the GGE. As both kinetic energy and weak interactions can delocalize

trapped quasiparticles, the dynamics of the system can reveal a rich interplay between quantum tunneling and interaction effects, leading to new types of relaxation beyond conventional prethermalization.

The model studied by Gong and Duan (2013) and Neyenhuis *et al.* (2017) is the same transverse-field Ising model described by Eq. (25). With long-range interactions,  $H_{TI}$  is generally nonintegrable, in contrast to the nearest-neighbor case, where the 1D model is integrable through a Jordan-Wigner transformation (Sachdev, 2011), so thermalization is anticipated in the longtime limit according to the eigenstate thermalization hypothesis (Rigol, Dunjko, and Olshanii, 2008). To better understand the dynamics of such a prethermal Hamiltonian, we can map each spin excitation along the  $z$  direction into a bosonic particle to turn Eq. (25) into a bosonic model with two parts: an integrable part composed of noninteracting spin-wave bosons that can be used to construct a GGE, and an integrability-breaking part consisting of interactions among the spin-wave bosons that is responsible for the thermalization (Neyenhuis *et al.*, 2017). When the initial state has a low spin or bosonic excitation density and the magnetic field is much larger than the average Ising coupling  $J_{ij}$ , the bosonic excitation density remains low during the dynamics and the interactions among the bosons remains weak.

The experiment conducted by Neyenhuis *et al.* (2017) began with the preparation of a single-spin excitation on either edge of a seven-ion chain  $|\psi_R\rangle = |\downarrow\downarrow\downarrow\downarrow\downarrow\downarrow\uparrow\rangle_z$  or  $|\psi_L\rangle = |\uparrow\downarrow\downarrow\downarrow\downarrow\downarrow\downarrow\rangle_z$ . The spins then evolved under Eq. (25) and the time evolution of the spin projection in the  $z$  basis was measured. The magnetic field  $B$  was at least an order of magnitude larger than  $J_0$  in the experiment, so the number of spin excitations along the  $z$  direction was approximately conserved in the short-time dynamics where the system can be regarded as a single-spin excitation. But in the long-time dynamics, multiple spin excitations are created and interact with each other.

To characterize the dynamics of the spin excitations, we introduce a single observable that measures the relative location of the spin excitation in the chain

$$C = \sum_{i=1}^N \left( \frac{2i - N - 1}{N - 1} \right) \left( \frac{\sigma_i^z + 1}{2} \right), \quad (48)$$

where  $N$  is the number of ions. The expectation value of  $C$  varies between  $-1$  and  $1$  for a spin excitation on the left and right ends, respectively. The choice of initial states ensures that the initial value of  $\langle C \rangle$  is either  $1$  or  $-1$ . Because of the spatial inversion symmetry of the underlying Hamiltonian in Eq. (25), both the GGE and thermal values of  $\langle C \rangle$  should be  $0$ .

In Figs. 27(c) and 27(d) the value of  $\langle C \rangle$  along with its cumulative time average  $\langle \bar{C} \rangle$  is shown for the two initial states with a single spin flips on either end of the spin chain. In the short-range interacting case ( $\alpha = 1.33$ ), where the system rapidly evolves to a prethermal state predicted by the GGE associated (with  $\langle \bar{C} \rangle = 0$ ) with the integrals of motion corresponding to the momentum space distribution of the single particle representing the spin excitation. The memory of the initial spin excitation location is thus not preserved.



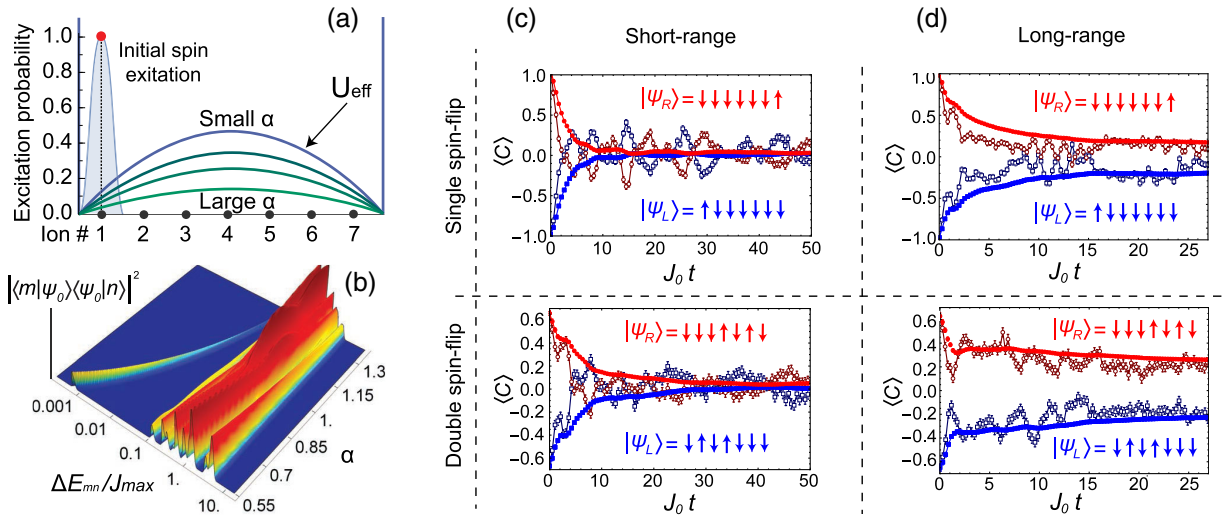


FIG. 27. (a) An initial spin excitation is prepared on one side of a seven-ion chain subject to open boundary conditions and long-range XY interactions. As the interaction range increases ( $\alpha$  decreases), the effective potential energy for the single excitation changes from a square-well potential to a potential resembling a double well. (b) The double-well potential gives rise to near-degenerate eigenstates when  $\alpha$  is decreased, as seen in the calculated energy difference between all pairs of eigenstates vs  $\alpha$ . The height of the plot quantifies the off-diagonal density matrix elements of the initial state. (c) In the case of short-range interactions, either one or two spin flips delocalize across the chain during time evolution, so that the quantity  $\langle C \rangle \approx 0$  in the long-time limit, consistent with the prediction of GGE. (d) For long-range interactions memory of initial conditions is preserved in a long-lived prethermal state. In both (c) and (d), the open squares and circles plot  $\langle C \rangle$  for initial states prepared on the left and right sides of the spin chain, while the filled circles and squares plot the cumulative time average  $\langle \bar{C} \rangle$  for these data. Adapted from Neyenhuis *et al.*, 2017.

However, in the long-range-interacting case ( $\alpha = 0.55$ ), the position of the spin excitation reaches a quasistationary value that retains memory of the initial state out to the longest experimentally achievable time of  $25/J_{\text{max}}$ . This prethermal state differs from a thermal state and the GGE prediction, which both maintain the left-right spatial symmetry of the system.

For evolution times too short to generate more than one spin flip, the dynamics of the Hamiltonian in Eq. (25) for the initial states are similar to those of a free particle in a potential, with the location of the particle representing that of the single-spin excitation. For short-range spin interactions, the shape of the potential is approximated by a square well due to the open boundary condition and no explicit spatial inhomogeneity of the interactions. However, as we increase the range of spin-spin interactions, the shape of the potential distorts from a square-well to a double-well shaped potential formed by the two hard walls at the ends of the spin chain and the bump at the center of the chain, as shown in Fig. 27(a). For a single particle on a lattice with a double-well potential, there will be an extensive number of near-degenerate eigenstates that are symmetric and antisymmetric superpositions of wave functions in the left and right potential wells. For seven lattice sites, the spectrum of energy differences between all pairs of eigenstates as a function of  $\alpha$  is shown in Fig. 27(b), together with the overlap of eigenstates with the initial state. For the longest-range interaction ( $\alpha = 0.55$ ), the two lowest energy states are almost degenerate, with an energy difference approximately 1000 times smaller than  $J_{\text{max}}$ . This stems from the tunneling rate between the two double wells, which is exponentially small in the barrier height, resulting in the spin

excitation remaining in its initial well until it tunnels across the potential barrier at long times.

To go beyond the previous single-particle picture, the experiment of Neyenhuis *et al.* (2017) prepared initial states with two spin excitations. In this case, there are weak interactions between the two particles that represent the spin excitations, similar to the scenario for many-body localization (Smith *et al.*, 2016). Despite the presence of weak interactions, similar prethermal states were found, as shown in the bottom panel of Figs. 27(c) and 27(d): Relaxation to the GGE is found for shorter-range interactions ( $\alpha = 1.3$ ), while for longer-range interactions the system does not relax to the GGE. Similar results were also found in a spin chain of 22 ions, as shown in Fig. 28 (Neyenhuis *et al.*, 2017). The persistence of the same prethermalization observed with more than a single-spin excitation is attributed by the existence of extensive number of nearly degenerate eigenstates for the single-particle spectrum in the double well shown in Fig. 28(a). Thus an extensive number of spin excitations near one end of the chain will still be localized by the double well before tunneling happens at a later time.

The interplay between single-particle tunneling in the effective double-well and particle-particle interactions is always present in this system; even when initialized in a single-spin excitation state, the finite transverse field in Eq. (25) will create more spin excitations over time. The effect of interactions will thermalize the system, while the effect of tunneling will bring the system to the GGE. Thus, depending on the range of spin-spin interactions, it is possible to either observe the prethermalization to the GGE after the prethermalization caused by the trapping in double-well

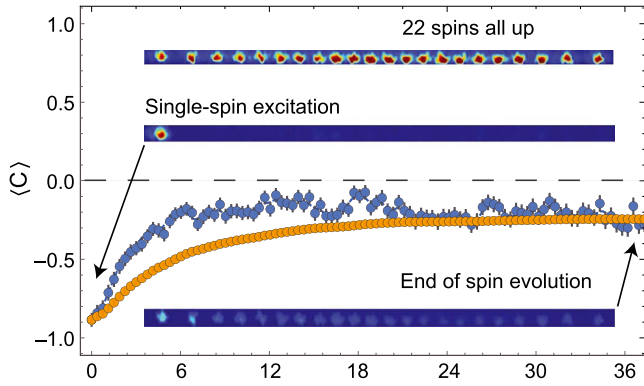


FIG. 28. Measured time evolution (darker points) and cumulative time average (lighter points) of the averaged center of excitation  $\langle C \rangle$  in a 22-ion chain (ion chain image shown at the top). The ion spins are initialized with a single-spin excitation on the left end (middle ion chain image). After evolving in the XY spin Hamiltonian for time  $t = 36/J_0$ , where  $J_0$  is the nearest-neighbor coupling and the spin excitation is delocalized, but its average position remains stuck on the left half of the chain (bottom ion chain image), the signature of prethermalization. Effective range of the interaction is  $\alpha \approx 0.9$ . Adapted from Neyenhuis *et al.*, 2017.

potential or observe thermalization directly after the observed prethermalization. Determining which scenario is relevant would require a much longer coherence time than is possible in current experiments. While improving the experimental coherence time of the spin interactions may be challenging, simulating the long-time dynamics of a nonintegrable, long-range interacting spin chain is equally, or even more, challenging on a classical computer.

We emphasize that the emergence of an effective double-well potential for the spin excitations is a phenomenon unique to an open spin chain with strongly long-range interactions. A spin chain with periodic boundary conditions and without spatial inhomogeneity is fully translationally invariant, and translational invariance is not expected to be broken in the long-time behavior of the system. Changing boundary conditions of a long-range interacting system can significantly impact its bulk properties. Prethermalization in trapped-ion spin crystals is thus a good example of new physics that is possible with programmable quantum simulators, reaching beyond existing condensed matter frameworks, as also demonstrated by other experiments mentioned in this section.

#### D. Stroboscopic dynamics and Floquet phases of matter

Section IV.B treated static time-independent Hamiltonians whose nonequilibrium nature arises from the presence of quenched disorder leading to many-body localization; such localization prevents the system's internal dynamics from thermalizing and leads to a certain memory of local initial conditions (Nandkishore and Huse, 2015; Abanin *et al.*, 2019). An alternate setting for exploring nonequilibrium phases is to begin with a time-dependent Hamiltonian whose equations of motion are intrinsically dynamical. This setting is ideal for trapped-ion quantum spin simulators, where pulsed control of both the interactions and fields of the

transverse-field Ising model of Eq. (25) naturally allows for the realization of time-dependent Hamiltonians; see Sec. III.A, where time-dependent magnetic fields are utilized.

Recently a tremendous amount of theoretical and experimental work has been devoted to exploring the mildest case of such time dependence, where the system is governed by a periodic Hamiltonian  $H(t+T) = H(t)$ . Such Floquet systems (Floquet, 1883; Bukov, D'Alessio, and Polkovnikov, 2015; Kuwahara, Mori, and Saito, 2016) are ideal from the perspective of quantum simulation since they do not require the complexities of cooling to the many-body ground state in order to observe novel dynamical phenomena (Bloch, Dalibard, and Zwerger, 2008). In the case of trapped ions, as we discussed in Sec. II, there exists a natural capability to stroboscopically apply different microscopic Hamiltonians, making this platform an ideal Floquet quantum simulator. Here we focus on two specific examples.

First, we describe the implementation of a novel class of measurements termed OTOC functions (Larkin and Ovchinnikov, 1969; Maldacena, Shenker, and Stanford, 2016). Such correlators have recently been proposed as powerful diagnostics of quantum chaos, and their dynamical behavior remains the subject of intense interest (Swingle *et al.*, 2016; Landsman *et al.*, 2019; Yoshida and Yao, 2019); indeed, the possibility of defining a quantum Lyapunov exponent based on the exponential growth of OTOCs in certain systems has led to a conjectured bound on the rate of thermalization in many-body quantum systems (Maldacena, Shenker, and Stanford, 2016).

The functional form of the OTOC is typically written as the expectation

$$F(\tau) = \langle W^\dagger(\tau) V^\dagger(0) W(\tau) V(0) \rangle, \quad (49)$$

where  $W$  and  $V$  are two commuting operators, with  $W(\tau) = e^{iH\tau} W e^{-iH\tau}$  the evolved operator  $W$  under the Hamiltonian  $H$ . The OTOC compares two quantum states obtained by either (a) applying  $V$ , waiting for a time  $t$ , and then applying  $W$ , or (b) applying  $W$  at time  $t$ , going back in time to apply  $V$  at  $t = 0$ , and then letting time resume its forward progression to  $t$ . The OTOC  $F(\tau)$  thus describes how initially commuting operators  $W$  and  $V$  fail to commute at later times due to the interactions generated by  $H$  and have a different form than the conventional autocorrelation function  $\langle W^\dagger(\tau) V(0) W^\dagger(\tau) V(0) \rangle$ . Operationally, measuring an OTOC requires an intermediate step of time reversal, representing a major challenge from an experimental implementation perspective (Gärtner *et al.*, 2017; Li *et al.*, 2017).

In the case of ions, it is possible to directly measure an OTOC stroboscopically applying both an interaction Hamiltonian and its negative counterpart, thus effectively reversing time evolution. This was experimentally demonstrated by Gärtner *et al.* (2017) by using a two-dimensional array of laser-cooled  ${}^9\text{Be}^+$  ions in a Penning trap; it is summarized in Fig. 29. Here the spin-dependent optical dipole force couples to the axial center-of-mass motion of the 2D crystal [see Fig. 2(b)], resulting in a nearly uniform all-to-all Ising interaction [Eq. (23) with  $\alpha \approx 0$ ]. Such an all-to-all interacting Ising model does not possess the complexity of

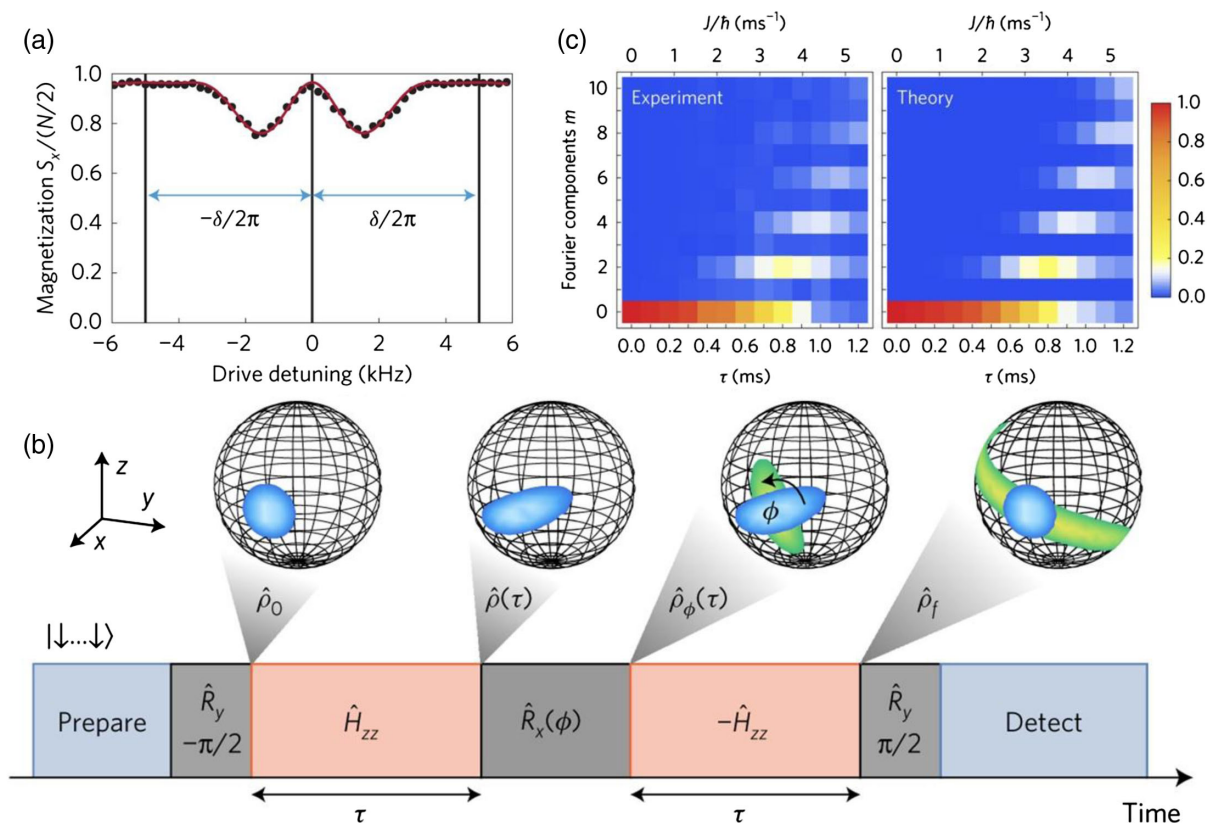


FIG. 29. Out-of-time-order-correlators (OTOC) in a 2D Penning trap ion simulator; see Fig. 2(b) for experimental schematic. (a) Demonstration of the ability to tune the sign of the Ising interaction through the symmetric detuning of the optical dipole force around a single mode of motion. Plotted is the residual spin-phonon couplings vs detuning from the center-of-mass mode. A positive (negative) detuning gives rise to an antiferromagnetic (ferromagnetic) interaction. (b) Experimental sequence used to measure an out-of-time-ordered correlation function with alternation in the sign of the Ising coupling. (c) Measured Fourier amplitudes of collective magnetization dynamics under the Ising spin-spin interactions for  $N = 111$  spins, showing the sequential buildup of higher-order spin-spin correlations. Adapted from Gärtner *et al.*, 2017.

interactions from a quantum chaos perspective. However, this system is well suited for OTOC studies, because the sign of the Hamiltonian can be controlled. Since the Ising interaction strength scales as  $J \sim 1/\delta$  [Eq. (22) with only a single mode contributing and  $\delta_m = \delta$ ], this allows for the implementation of a Hamiltonian sign reversal by simply changing the sign of the detuning. With the ability to stroboscopically apply both  $H$  and  $-H$ , a family of different OTOCs can then be measured through the collective magnetization of the system, as shown in Fig. 29 (Gärtner *et al.*, 2017). We finally note that a recent experiment has measured OTOCs in a chain of trapped atomic ions using measurements in random spin bases (Joshi *et al.*, 2020).

The second example of stroboscopic Hamiltonian simulation with trapped-ion spin systems is the quantum simulation of Floquet systems, or periodically modulated Hamiltonians (Bukov, D'Alessio, and Polkovnikov, 2015; Deng *et al.*, 2015; Kuwahara, Mori, and Saito, 2016). In a broader context, such time-periodic manipulations have long been used for controlling quantum systems including NMR qubits and atomic ensembles (Goldman *et al.*, 2014; Oka and Kitamura, 2019). However, recent explorations of Floquet systems have stumbled upon an intriguing question beyond the landscape of quantum control: in particular, can Floquet

systems host intrinsically new phases of matter that do not have any equilibrium equivalent (Moessner and Sondhi, 2017; Else *et al.*, 2020)?

In the noninteracting single-particle case, the question has been affirmatively answered with the discovery of a host of novel band structures that can exist only in the presence of periodic driving (Kitagawa *et al.*, 2010; Lindner, Refael, and Galitski, 2011; Cayssol *et al.*, 2013; Rechtsman *et al.*, 2013; Titum *et al.*, 2016). The many-body case is more subtle. On the one hand, one might naturally suspect that new phenomena can in principle arise when the driving frequency is of the order of the intrinsic energy scales of the system; indeed, this limit is far from the Suzuki-Trotter limit (as discussed in Sec. V.A), where to first order the effective Hamiltonian describing the Floquet system is simply a sum of its stroboscopic components. On the other hand, it is generally expected that a driven many-body system will absorb energy from the driving field and ultimately heat to infinite temperature (Bukov, D'Alessio, and Polkovnikov, 2015; Ponte, Chandran *et al.*, 2015). However, recent theoretical advances have demonstrated that it is possible to avoid such Floquet heating. One general scheme is to utilize many-body localization as discussed in Sec. IV.B. In principle, a Floquet MBL system (Ponte, Papić *et al.*, 2015; Abanin, Roeck, and

Huveneers, 2016) can exhibit stable dynamical phases of matter for infinitely long times (Else, Bauer, and Nayak, 2016; Khemani *et al.*, 2016; Potirniche *et al.*, 2017). Recent studies suggest an alternative disorder-free approach can also be used to combat Floquet heating, albeit not to infinite times. In particular, for large enough driving frequencies, the system can enter a regime of Floquet prethermalization (Kuwahara, Mori, and Saito, 2016; Mori, Kuwahara, and Saito, 2016), where exotic nonequilibrium phases can be observed for exponentially long timescales (Else, Bauer, and Nayak, 2017; Machado *et al.*, 2019, 2020). The underlying essence of Floquet prethermalization is analogous to the discussions of prethermalization in Sec. IV.C. The key difference is that here the lifetime of the quasistationary state is controlled by the Floquet drive frequency.

We now turn to recent experiments that demonstrated a Floquet quantum simulation using a one-dimensional trapped-ion spin chain, depicted in Fig. 30 (Zhang *et al.*, 2017). In these experiments, a combination of high-precision spatial and temporal control allowed for the implementation of three distinct types of time evolution applied repeatedly in sequence: (1) global spin rotations, (2) long-range Ising interactions, and (3) disordered on-site fields [Fig. 30(a)].

The stroboscopic combination of these evolutions is the basis for realizing a discrete time crystal (DTC) (Else, Bauer, and Nayak, 2016; Khemani *et al.*, 2016; von Keyserlingk, Khemani, and Sondhi, 2016; Yao *et al.*, 2017; Else *et al.*, 2020), where a system exhibits a spontaneous breaking of the time-translation symmetry generated by the Floquet evolution. The characteristic signature of a DTC, which is consistent with experimental observations in chains of up to  $L = 14$  ions (Zhang *et al.*, 2017), is the robust synchronization of oscillations at subharmonic frequencies relative to that of the drive, as shown in Figs. 30(b) and 30(c). Within the decoherence timescale of the experiments, the observed signatures of DTC order are independent of the initial state. The robustness of the subharmonic oscillations depends on the presence of strong interactions in the system; in the absence of

interactions, even small perturbations immediately destroy signatures of a time crystal.

In addition to implementations in trapped-ion systems, a number of other experimental platforms have also observed signatures of time crystalline order (S. Choi *et al.*, 2017; Rovny, Blum, and Barrett, 2018). Here we note a particular set of experiments performed using ensembles of nitrogen-vacancy color centers in diamonds (S. Choi *et al.*, 2017). We emphasize this particular platform because it shares a number of similar features with the trapped-ion system (i.e., long-range interactions and disorder) but also has a number of crucial differences (i.e., three-dimensional system with time-dependent disorder). Both platforms exhibit similar signatures of interaction stabilized time-translation symmetry breaking, although these signatures appear to be limited to timescales before local thermalization has fully completed (Else *et al.*, 2020). To this end, such cross-platform verifications are especially valuable once controlled quantum simulators reach a regime where classical computers cannot calculate (Leibfried, 2010; Calarco, Fazio, and Mataloni, 2018). In this regard, comparing the results from analog quantum simulators to those from digital quantum computers would also be helpful in cross-checking and assessing validity (Mahadev, 2018).

## E. Dynamical phase transitions

Having discussed the simulation of nonequilibrium phases in both disordered and periodically driven trapped-ion experiments, we now turn to the question of understanding phase transitions in such out-of-equilibrium systems. Novel dynamical phases can emerge after a quantum quench, and the transition between them can be observed experimentally by measuring nonanalytic changes in the dynamical response of the many-body spin system (Jurcevic *et al.*, 2017; Zhang, Pagano *et al.*, 2017). As described in Secs. IV.B and IV.C, out-of-equilibrium systems do not necessarily behave thermodynamically, so it is a fundamental question as to how to properly establish analogies and differences among

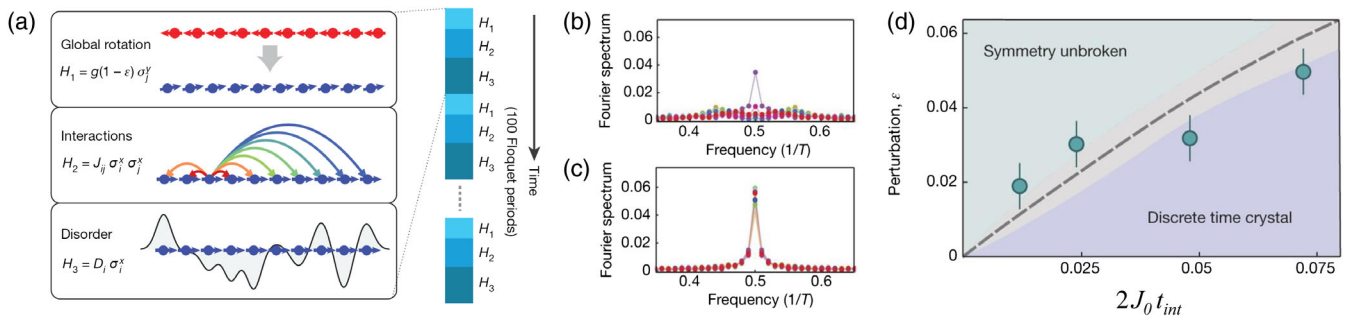


FIG. 30. Floquet quantum simulation of a discrete time crystal (DTC). (a) Schematic depiction of the Floquet evolution of a trapped-ion spin chain. Three Hamiltonians are applied sequentially in time: (i) a global nominal  $\pi$  pulse ( $2gt = \pi$ ) around the spin  $y$  axis with fractional perturbation  $\epsilon$ , (ii) long-range Ising interactions (see Sec. II), and (iii) site-dependent disorder along the spin  $x$  axes. (b) The  $x$  magnetization of each spin is measured after each Floquet sequence, up to 100 periods. The Fourier transform of the oscillations show a clear peak observed at half the driving frequency, even with a programmed perturbation on the global  $\pi$  pulses of  $\epsilon = 0.03$ , signaling the discrete breaking of time-translation symmetry and the “rigidity” of the time crystal. (c) When the perturbation is too strong ( $\epsilon = 0.11$ ), we cross the boundary from the DTC into a symmetry-unbroken phase. (d) For stronger interactions parametrized by the nearest-neighbor Ising coupling  $J_0$ , the DTC can tolerate larger imperfections to the global rotation pulse, leading to a qualitative phase diagram (Yao *et al.*, 2017). Adapted from Zhang *et al.*, 2017.

thermodynamic equilibrium phases and their dynamical counterparts (Heyl, 2018; Titum *et al.*, 2019) in terms of order parameters (Ajisaka, Barra, and Žunkovič, 2014; Žunkovič *et al.*, 2018), scaling and universality (Heyl, 2015), and discrete or continuous symmetry breaking (Žunkovič, Silva, and Fabrizio, 2016; Weidinger *et al.*, 2017; Huang, Banerjee, and Heyl, 2019).

Dynamical phases can be separated by dynamical quantum phase transitions (DQPTs), characterized by a nonanalytic response of the physical system as a function of quench parameters. Two types of DQPT signatures have been defined for an interacting spin-1/2 chain (Žunkovič *et al.*, 2018) governed by the Hamiltonian in Eq. (25) with the field along the  $z$  axis

$$H = \sum_{i<j} J_{ij} \sigma_x^i \sigma_x^j + B \sum_i \sigma_z^i, \quad (50)$$

where the spin-spin interactions  $J_{ij}$  and the transverse field  $B_z$  are generated using the technique explained in Sec. I.C.2. Both types of DQPT have been experimentally observed in a trapped-ion quantum simulator (Jurcevic *et al.*, 2017; Zhang, Pagano *et al.*, 2017). The first type of DQPT (type I) is based on the formal analogy between the nonanalytic behavior of the return probability to the initial state  $|\psi_0\rangle$  after a quantum quench under the Hamiltonian  $H$ , defined as  $\mathcal{G}(t) = \langle \psi_0 | e^{-iHt} | \psi_0 \rangle$ , and the partition function of the corresponding equilibrium system  $Z = \text{Tr}(e^{-H/k_B T})$  (Heyl, Polkovnikov, and Kehrein, 2013). It is possible to define the complex counterpart of the thermodynamic free energy density  $f = -N^{-1} k_B T \log(Z)$  using the rate function  $\lambda(t) = -N^{-1} \log[\mathcal{G}(t)]$ . This quantity, in the thermodynamic limit, exhibits dynamical real-time nonanalyticities that play an analogous role as the nonanalytic behavior of the free energy density of a thermodynamic system at equilibrium. It is possible to observe experimentally these nonanalyticities in an interacting spin chain after a quantum quench evolving

under the long-range transverse-field Ising Hamiltonian of Eq. (50).

This type of DQPT has been observed experimentally with a linear chain of trapped  $^{40}\text{Ca}^+$  ion spins (Jurcevic *et al.*, 2017). The spins are initialized in the ground state of the field part of the transverse Ising model, namely,  $|\psi_0\rangle = |\downarrow\downarrow\downarrow\dots\downarrow\rangle_z$ . Then the transverse-field Hamiltonian [Eq. (50)] is suddenly switched on (quenched) with  $B > J_0$ , with  $J_0$  the average nearest-neighbor spin-spin coupling. As shown in Fig. 31(a), in this regime the rate function  $\lambda$  exhibits pronounced nonanalyticities at the critical times  $t_c$ . This behavior can be related to other observables, such as the global average magnetization  $M_x = N^{-1} \sum_i \sigma_i^x$ . Since the initial state breaks the  $\mathbb{Z}_2$  symmetry of the Hamiltonian (25), the system restores this symmetry during the evolution at the times where the magnetization changes sign, which also corresponds to the critical times in the Loschmidt echo observable, as shown in Fig. 31(b).

The second type of DQPT (type II) has an order parameter defined in terms of long time-averaged observables, such as asymptotic late-time steady states of local observables

$$\bar{A} = \lim_{T \rightarrow \infty} \frac{1}{T} \int_0^T A(t) dt, \quad (51)$$

where the operator  $A$  is the magnetization or higher-order correlators between the spins. Here the DQPT occurs as the ratio  $B/J_0$  is varied and the order parameter changes abruptly from ferromagnetic ( $B < J_0$ ) to paramagnetic order ( $B > J_0$ ). The onset of this nonanalytic behavior can be observed by measuring the late-time average values of the two-body correlator

$$C_2 = \frac{1}{N^2} \sum_{ij} \langle \sigma_i^x \sigma_j^x \rangle \quad (52)$$

after a quantum quench with Hamiltonian (50).

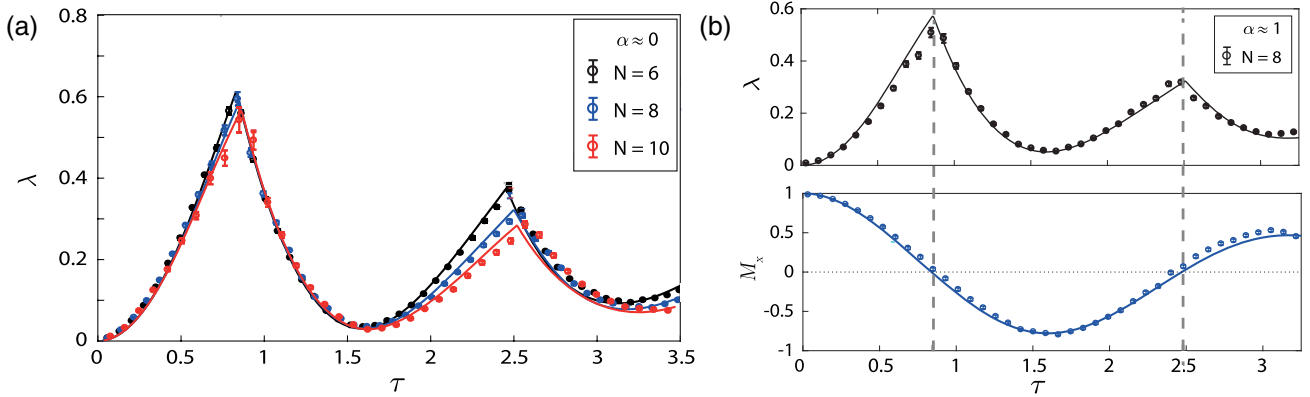


FIG. 31. Trapped-ion quantum simulation of DQPT type I. (a) Measured rate function  $\lambda$  for three different system sizes at  $B/J_0 \approx 2.38$ , with  $\tau = tB$  the dimensionless time. The kinks in the evolution become sharper for larger  $N$ . To take the  $\mathbb{Z}_2$  degeneracy of the ground state of  $H_0$  into account, here the rate function is defined based on the return probability to the ground-state manifold, namely,  $\lambda(t) = N^{-1} \log(P_{|\psi_0\rangle} + P_{|-\psi_0\rangle})$ , where  $|-\psi_0\rangle = |\uparrow\uparrow\uparrow\dots\uparrow\rangle_x$ . (b) Comparison between rate function  $\lambda(t)$  and magnetization evolution  $M_x(t)$ . The inversion of the magnetization sign corresponds to the nonanalyticity of the rate function  $\lambda(t)$ . Solid lines are exact numerical predictions based on experimental parameters ( $B/J_0 = 2$ ). Adapted from Jurcevic *et al.*, 2017.

This type of DQPT measurement was observed in a linear chain of trapped  $^{171}\text{Yb}^+$  ion spins (Zhang, Pagano *et al.*, 2017). Here the measured late-time correlator  $C_2$  exhibits a dip at the critical point that sharpens scaling up the system size  $N$  up to 53  $^{171}\text{Yb}^+$  ions, as shown in Fig. 32(a). This represents one of the largest quantum simulations ever performed on individual spins. Further evidence of the occurrence of the phase transition can also be observed in higher-order correlations, such as the distribution of domain sizes throughout the entire chain shown in Fig. 32(b). The occurrence of the DQPT is observed in the decreased probabilities of observing long strings of aligned ions at the critical point. This is more clearly shown by measuring the mean largest domain size as a function of the transverse-field strength for late times and repeated experimental shots, which exhibits a sharp transition across the critical point of DQPT type II. Note this measurement is in general an  $N$ -th-order spin correlation function, requiring high fidelity readout of all spins in a single shot, which is an attribute that is unique to trapped-ion systems.

## V. HAMILTONIAN SEQUENCING AND ENGINEERING

The tailored interactions between spins available in trapped-ion systems can also be used to realize a DQS, which is a many-body quantum system with enough control to perform a universal set of quantum operations or gates. In other words, it is a quantum computer used to implement Hamiltonian evolution rather than other quantum algorithms (Feynman, 1982). The universality means that these simulations are not limited to the inherent interactions, but any local Hamiltonian can be designed and implemented as a circuit (Lloyd, 1996). Additionally, error bounds and error correction protocols using fault-tolerant gate sets are applicable to large digital simulations (Steane, 1999).

Arbitrary Hamiltonians can be transformed into spin or qubit forms via the Jordan-Wigner (Jordan and Wigner, 1928) or Bravyi-Kitaev (Bravyi and Kitaev, 2002) transformation. First-quantization mapping can also be used (Bravyi *et al.*, 2017; Babbush *et al.*, 2018). There are several methods for approximating time evolution or adiabatic ramps through

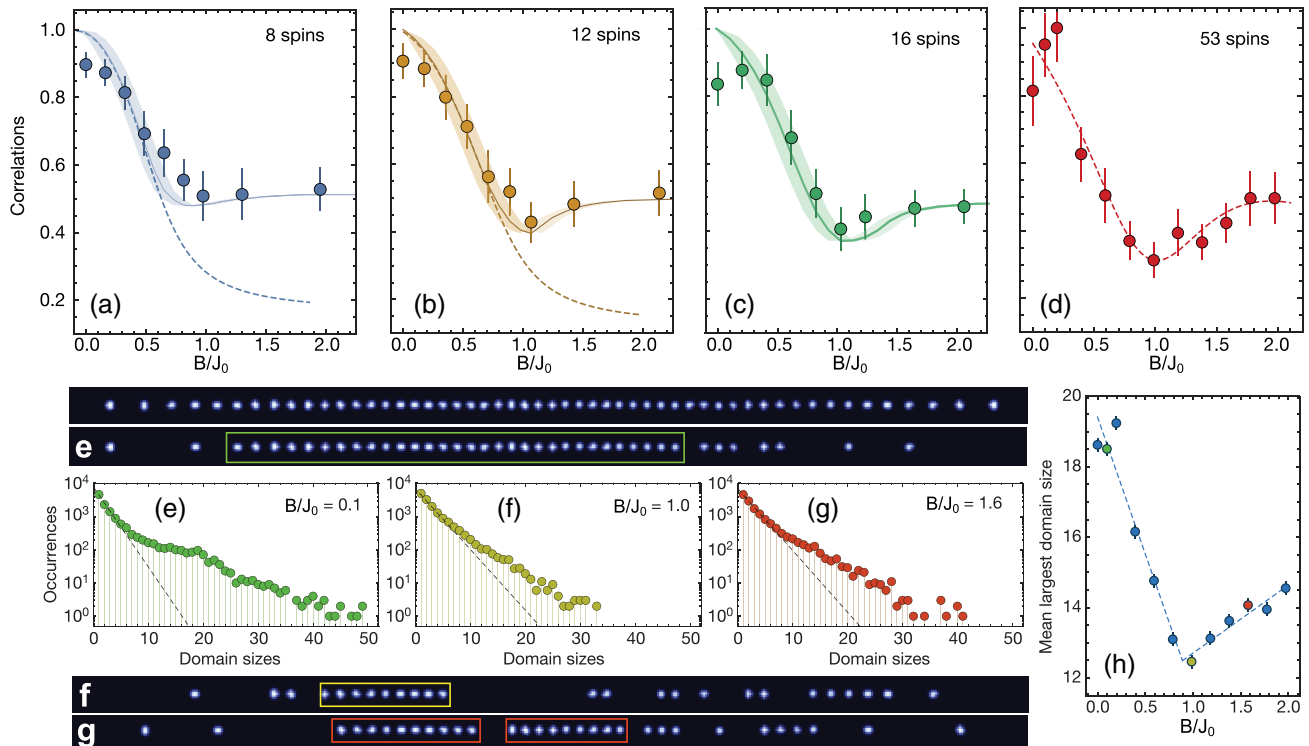


FIG. 32. (a)–(d) Trapped-ion quantum simulation of a dynamical quantum phase transition of type II following the long-range transverse Ising Hamiltonian with  $\alpha \approx 1$ . Long-time averaged values of the two-body correlations  $C_2$  for different numbers of spins in the chain ranging from 8 to 53. Solid lines are exact numerical solutions to the Schrödinger equation, and the shaded regions take into account uncertainties from experimental Stark-shift calibration errors. Dashed lines in (a) and (b) are calculations using a canonical thermal ensemble with an effective temperature corresponding to the initial energy density. (e)–(g) Domain statistics and corresponding image samples after late-time evolution for various values of  $B/J_0$  with 53 spins. The reconstructed ion chain images are based on single-shot binary detection of each ion spin state. The top image shows a chain of 53 ions all in bright spin states as a baseline. The other three images show 53 ions in combinations of bright and dark spin states. (e)–(g) Distribution of domain sizes for three different values of  $B/J_0$ , plotted on a logarithmic scale. Dashed lines are fits to exponential functions, which are expected for an infinite-temperature thermal state. Long tails of deviations are visible, and their prevalence depends on  $B/J_0$ . (h) Mean of the largest domain size in each single experimental shot vs  $B/J_0$ , showing a kink at the phase transition. Dashed lines represent a piecewise linear fit, used to extract the transition point  $B/J_0 = 0.89(7)$ . Adapted from Zhang, Pagano *et al.*, 2017.

discrete operations in a DQS, Trotterized evolution (Trotter, 1959; Suzuki, 1985) or variational techniques (Yuan *et al.*, 2019). These include the variational quantum eigensolver (VQE) (Peruzzo *et al.*, 2014) and QAOA (Farhi *et al.*, 2000) techniques. Alternatives include quantum walks (Childs *et al.*, 2003) and Taylor series expansions. We note that the latter has potential for fault-tolerant devices due to its optimal asymptotic scaling, but this has not been demonstrated experimentally (Berry *et al.*, 2015).

### A. Trotter Hamiltonian expansion

To decompose the unitary evolution under a given Hamiltonian into discrete operations or gates, Suzuki-Trotter (Trotter, 1959; Suzuki, 1985) formulas are commonly used. These provide an approximate factorization of the unitary time-evolution operator  $\hat{U}$ . For a time-independent Hamiltonian  $H$  containing a sum of terms  $H_k$ , the first-order Trotter approximation  $\hat{U} = e^{-i\hat{H}t/\hbar} = \lim_{n \rightarrow \infty} (\prod_k e^{-i\hat{H}_k t/n\hbar})^n$  for finite  $n$  leads to a sequence of small time steps  $\delta t = t/n$  with local evolution operators  $\hat{U}_k = e^{-i\hat{H}_k \delta t/\hbar}$  that is repeated  $n$  times. These operators can then be deconstructed into the operations from the simulator's universal set. Similarly, a time-dependent Hamiltonian can be simulated by breaking the evolution down into short segments (Poulin *et al.*, 2011). Since the unitaries  $U_k$  do not commute in general for finite  $n$ ,

the sequence deviates from the target evolution. These Trotter errors are bounded for small step sizes but undergo a dynamical phase transition (Heyl, Hauke, and Zoller, 2019), above which the evolution exhibits many-body quantum chaos (D'Alessio *et al.*, 2016; Sieberer *et al.*, 2019).

This technique was used by Lanyon *et al.* (2011) in a trapped-ion experiment to simulate a range of different interaction models and interaction graphs of two to six spin-1/2 particles. This spin-model problem matches the system and does not require a transformation. Using the operations available from the toolbox described in Sec. I.C.2, a universal set of operations is realized. The versatility of this approach is shown by simulating the dynamics of two particles under an  $XX$ - (Ising),  $XY$ -, and  $XYZ$ -type interaction, and an adiabatic ramp of the interaction strength. Figure 33(a) shows the dynamics of four spins initialized along  $z$  under a long-range (all-to-all) Ising interaction. The oscillation frequencies correspond to energy gaps in the system. Figure 33(b) presents the collective oscillation of six spins under a  $\sigma_y^1 \sigma_x^2 \sigma_x^3 \sigma_x^4 \sigma_x^5 \sigma_x^6$  interaction, composed digitally of Ising-type interactions and individual  $\sigma_z$  rotations, periodically producing a six-spin GHZ state.

Interleaving different native operations has also been proposed for creating an  $XXZ$  interaction in a spin-1 system (Cohen *et al.*, 2015). This will allow for the study of an integer-spin systems under Heisenberg-type interactions,

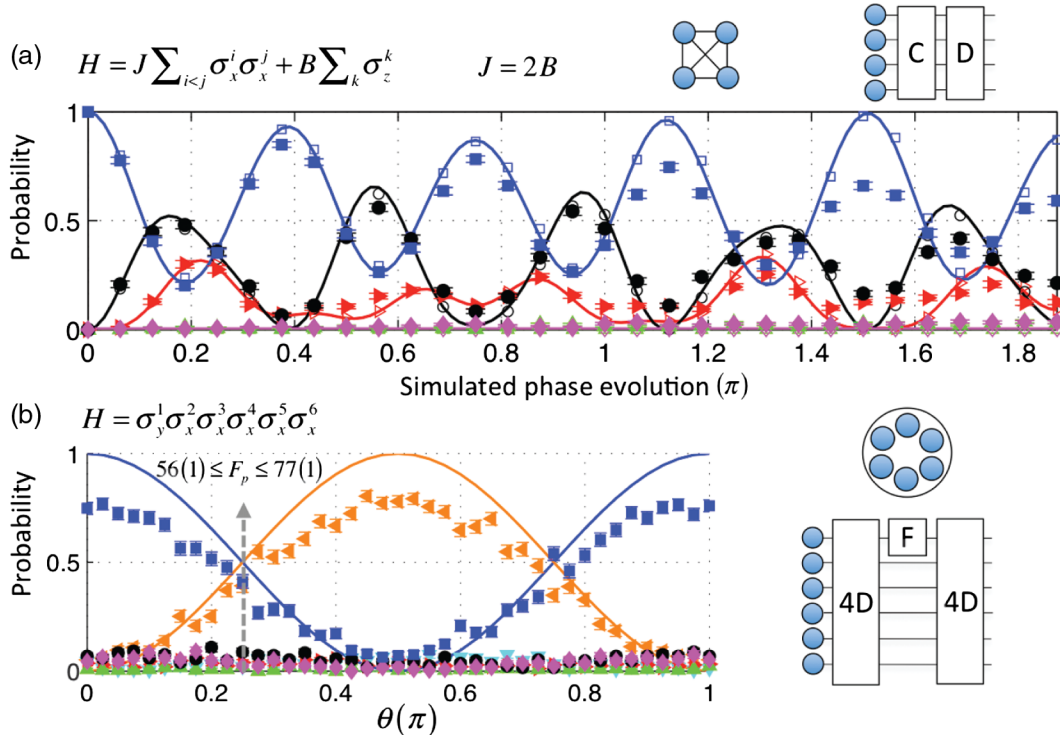


FIG. 33. Digital simulations of dynamics in four- and six-spin systems. Initially, all spins point up. (a) Four-spin long-range Ising system. Each digital step is given by operators  $C = \exp(-i\theta_C \sum_i \sigma_z^i)$  with  $\theta_C = \pi/32$  and  $D = \exp(-i\theta_D \sum_{i < j} \sigma_{\phi_D}^i \sigma_{\phi_D}^j)$ , with  $\theta_D = \pi/16$  and  $\phi_D = 0$ . (b) Six-body interaction with six spins.  $F = \exp(-i\theta \sigma_z)$  with  $\theta$  variable, and  $4D = \exp(-i\theta_0 \sum_{i < j} \sigma_{\phi_0}^i \sigma_{\phi_0}^j)$ , with  $\theta_0 = \pi/4$  and  $\phi_0 = 0$ . Bounds for the quantum process fidelity  $F_p$  are given at  $\theta = 0.25\pi$ . Lines, exact dynamics; unfilled shapes, ideal digitized; filled shapes, data (squares,  $P_0$ ; diamonds,  $P_1$ ; circles,  $P_2$ ; triangles pointing up,  $P_3$ ; triangles pointing right,  $P_4$ ; triangles pointing down,  $P_5$ ; triangles pointing left,  $P_6$ , where  $P_i$  is the total probability of finding  $i$  spins pointing down). Adapted from Lanyon *et al.*, 2011.

including the Haldane phase (Haldane, 1983). Adding optical pumping as an incoherent process to the set of operations was used by Barreiro *et al.* (2011) to create the ability to engineer open-system dynamics, and show the dissipative preparation of multiqubit stabilizer states for quantum error correction. Evolution by DQS can also be combined with standard computational gates to measure quantities of interest. A digital simulation of the two-site Fermi-Hubbard model was given by Linke *et al.* (2018). After a Trotterized adiabatic ramp composed of two-qubit  $XX$  interactions and single-qubit rotations, the second Rényi entropy was measured. In contrast to the approach taken by Brydges *et al.* (2019), this is achieved by creating two copies of the state and measuring the expectation value of the SWAP operator following (Horodecki and Ekert, 2002; Johri, Steiger, and Troyer, 2017).

The DQS approach has also been proposed for quantum field theory simulations using trapped ions (Bañuls *et al.*, 2019). The Schwinger model, an example of a lattice gauge theory, describes fermions coupled to an electromagnetic field in one spatial dimension. After mapping the model to qubits with the Jordan-Wigner transformation using open boundary conditions, the Hamiltonian reads (Muschik *et al.*, 2017; Kokail *et al.*, 2019)

$$\hat{H}_S = w \sum_{n=1}^{N-1} (\hat{\sigma}_n^+ \hat{\sigma}_{n+1}^- + \hat{\sigma}_n^- \hat{\sigma}_{n+1}^+) + \frac{m}{2} \sum_{n=1}^N (-1)^n \hat{\sigma}_n^z + g \sum_{n=1}^{N-1} \hat{L}_n^2, \quad (53)$$

where  $n$  labels the lattice sites. Following a Kogut-Susskind encoding, spin-down (spin-up) on an odd (even) lattice site indicates the presence of a positron (electron). The first term represents particle-antiparticle pair creation and annihilation with coupling  $w$ . The second term is a mass term and the third term represents the energy of the electric field  $\hat{L}_n$  with coupling  $g$ . The model reproduces key features of more complex high-energy physics theories such as quantum chromodynamics (Gattringer and Lang, 2010), which are extremely challenging for classical numerical methods.

An experiment realizing the Schwinger model in a trapped-ion spin chain was implemented by Martinez *et al.* (2016) and showed good agreement with the ideal evolution for the real-time dynamics of a two-site (four-qubit) model. The difficulty in mapping gauge theories to spins lies in the infinite-dimensional Hilbert space of the gauge field operators. Instead of truncating the model to the size of the simulator, Martinez *et al.* analytically integrated out the gauge fields using Gauss's law, allowing the electric field to be expressed in terms of Pauli operators:  $\hat{L}_n = \epsilon_0 - (1/2) \sum_{l=n+1}^N [\hat{\sigma}_l^z + (-1)^l]$ . This creates a spin Hamiltonian with asymmetric long-range couplings (Hamer, Weihong, and Oitmaa, 1997), which can be directly implemented by a sequence of multi-ion spin-spin operations (Martinez *et al.*, 2016; Muschik *et al.*, 2017). By construction, the scheme constrains the evolution within the subspace allowed by Gauss's law and hence maintains the gauge invariance of the theory (Muschik *et al.*, 2017). These features, as well as the linear scaling of the number of gate operations and qubits with lattice size, make DQSs with

trapped ions a promising avenue for the simulation of more complex gauge theories.

Quantum walks provide an alternative framework to discretize a unitary evolution for a DQS. Quantum walks, the quantum equivalent of classical random walks (Childs *et al.*, 2003), see a system evolve into a discrete grid or continuum of spacial locations based on the superposition of a quantum coin. Discrete step quantum walks have been mapped to represent simulations of different physical systems (Chandrashekar, Banerjee, and Srikanth, 2010; Di Molfetta and Pérez, 2016), including the evolution of a particle under the Dirac equation (Mallick *et al.*, 2019). The latter was realized in trapped ions by mapping the position space to multiqubit spin states, where different particle masses were chosen by varying the weight of the quantum coin (Huerta, Alderete *et al.*, 2020). Trapped-ion experiments have previously realized quantum walks (Schmitz *et al.*, 2009; Zähringer *et al.*, 2010) and separately a Dirac equation (Gerritsma *et al.*, 2010) simulation, using the harmonic-oscillator degrees of freedom in the trap rather than mapping to spins. A nonvariational digital simulation of spin models was also performed with superconducting qubits (Salathé *et al.*, 2015).

## B. Variational quantum simulation

VQS implements the versatile classical method of variational simulation (Balian and Vénéroni, 1988; Szabo and Ostlund, 2012; Shi, Demler, and Ignacio Cirac, 2018) on a quantum computer by employing a quantum-classical hybrid approach. Hybrid quantum algorithms are a promising way to solve potentially difficult problems on non-fault-tolerant, near-term quantum systems (Preskill, 2018) by combining classical and quantum resources. They distribute the task between a quantum and a classical computer. The quantum system is running a parametrized sequence of operations to generate a classically intractable state of interest following an approximate evolution under a Hamiltonian or a quantum gate sequence. The classical system varies the parameters to minimize a cost function evaluated by measuring the quantum state, a task that is considered relatively easy based on its complexity class (Yuan *et al.*, 2019). Employing trapped-ion spin simulators, this concept has been used to train a generative model, a routine from classical machine learning, using an ion-trap-based digital quantum circuit with up to 26 parameters (Zhu *et al.*, 2019). Zhu *et al.* showed that the choice of optimizer is crucial as the parameter space grows. One of the challenges of this approach lies in the cost function landscapes, which can exhibit so-called barren plateaus (McClean *et al.*, 2018), making optimization hard. Finding the classical optimization strategy and making efficient use of quantum resources is an active area of research (Wecker, Hastings, and Troyer, 2015; Yang *et al.*, 2017; Cirstoiu *et al.*, 2019; Sundar *et al.*, 2019).

VQS employs such a hybrid approach to simulating physical models. For solving static problems, the Rayleigh-Ritz variational method is generalized to the quantum regime. The ground-state energy of a Hamiltonian  $\hat{H} = \lambda_i \hat{h}_i$ , given as a linear combination of tensor products of local operators  $\hat{h}_i$ , can be estimated by considering trial wave functions  $|\phi(\vec{\theta})\rangle$



with parameters  $\vec{\theta} = (\theta_1, \theta_2, \dots)$  and approximating the ground-state energy using an upper bound (Yuan *et al.*, 2019)

$$E_0 \leq E_0^{\text{est}} = \min_{\vec{a}} \langle \phi(\vec{a}) | \hat{H} | \phi(\vec{a}) \rangle. \quad (54)$$

$E_0^{\text{est}}$  is obtained by preparing  $|\phi(\vec{\theta})\rangle$  through a sequence of parametrized quantum operations. Different circuit parameters implement different instances of  $\vec{\theta}$ , and  $\langle \phi(\vec{a}) | \hat{H} | \phi(\vec{a}) \rangle$  is obtained by measuring each term  $\langle \phi(\vec{a}) | \hat{h}_i | \phi(\vec{a}) \rangle$  and calculating the linear combination given by  $\{\lambda_i\}$ . A classical optimization routine such as a gradient-descent algorithm uses this value as a cost function to converge to  $E_0^{\text{est}}$ .

An illustration of this method was presented by Kokail *et al.* (2019), who performed a VQS of the Schwinger model described in Sec. V.A. Starting from  $|\Psi_0\rangle = |\uparrow\downarrow\dots\uparrow\downarrow\rangle$ , which corresponds to the bare vacuum state, they applied finite-range Ising interactions (see Sec. I.C.2) to all ions and alternated with individual  $\hat{\sigma}_z$  shifts realized with a Stark-shift beam. The set of discrete operations used in this ansatz enforces the symmetries of the problem, namely, Gauss's law and gauge invariance. Each operation is parametrized and the cost function is given by  $\langle \Psi(\vec{\theta}) | \hat{H}_S | \Psi(\vec{\theta}) \rangle$ , where  $\hat{H}_S$  is the Schwinger Hamiltonian from Eq. (53) and  $|\Psi(\vec{\theta})\rangle$  is the trial wave function. The cost function is evaluated by expressing  $\hat{H}_S$  as a string of Pauli operators and measuring their expectation values by projecting the experimental output state in the appropriate basis. An adaptive classical optimization process based on the dividing rectangles algorithm (Liu *et al.*, 2015) is employed in a quantum-classical feedback loop to find the minimum. At the minimum, the classical parameters  $\vec{\theta}_0$  describe a sequence to prepare the approximate ground-state wave function, and the cost function gives an upper bound estimate of the ground-state energy. Kokail *et al.* (2019) used this method with 20 (16) ions to optimize over an up to 15-dimensional parameter space and achieve 85% (90%) ground-state fidelity and an estimate of the ground-state energy within  $2\sigma$  uncertainty. One of the challenges in variational quantum algorithms is the verification of convergence since classical simulation cannot provide a measure of success. For eight ions, Kokail *et al.* (2019) used the variance of the cost function as a termination criterion by measuring the Hamiltonian in additional sets of bases to determine  $\langle \hat{H}_S^2 \rangle$ , making the optimization “self-verifying.” In a final eight-ion measurement, a phase transition (Byrnes *et al.*, 2002) was observed by varying the mass in the Schwinger Hamiltonian and observing an order parameter (Kokail *et al.*, 2019). Here the Rényi entropy was shown to peak at the critical point using the method described by Brydges *et al.* (2019). To overcome the deep circuits required for digital lattice gauge theory simulations, an analog approach with tailored spin-spin interactions in an ion chain was recently proposed (Davoudi *et al.*, 2020).

Different ways to construct circuits or sequences of quantum operations for preparing the trial wave function have been used. On the one hand, there is the so-called hardware-efficient ansatz as used by Kokail *et al.* (2019), who constructed the sequence from available operations without

trying to reproduce the precise problem Hamiltonian. It is straightforward to implement but more susceptible to optimization problems like barren plateaus (McClellan *et al.*, 2018). On the other hand, the physically inspired ansatz prescribes a more problem-specific construction for the trial states based on unitary coupled-cluster (UCC) theory, as mentioned later. The cost function tends to better match the underlying problem, but it can quickly lead to deep circuits as the complexity of the physical system increases (Shehab, Kim *et al.*, 2019).

For the simulation of physical models two flavors of variational algorithms are distinguished, which are both based on the VQS method but used in different domains of application, the VQE (Peruzzo *et al.*, 2014) for the determination of Hamiltonian eigenvalues (Yuan *et al.*, 2019), such as in the determination of ground-state and excited state energies in quantum chemistry, and the QAOA (Farhi, Goldstone, and Gutmann, 2014) for combinatorial optimization such as graph problems and approximate state preparation. In the following sections, results on both are reviewed from recent work with trapped ions. We note that a probabilistic variant has also been proposed for implementation with trapped ions (Zhang *et al.*, 2020).

## 1. Variational quantum eigensolvers

The VQE is a DQS algorithm for the calculation of operator eigenvalues that has been employed to tackle molecular electronic structure and molecular dynamics problems in quantum chemistry (Peruzzo *et al.*, 2014; Yung *et al.*, 2014; McClellan *et al.*, 2016) as an efficient alternative to quantum phase estimation (Aspuru-Guzik *et al.*, 2005). Under the Born-Oppenheimer approximation, which fixes the internuclear distances, the quantum chemistry Hamiltonian can be written in a second quantization formulation using a basis of molecular orbitals. These are formed following the Hartree-Fock method by a linear combination of atomic orbitals (Helgaker, Jørgensen, and Olsen, 2000). The electronic part of the Hamiltonian then reads

$$\hat{H} = \sum_{pq} h_{pq} \hat{a}_p^\dagger \hat{a}_q + \frac{1}{2} \sum_{pqrs} h_{pqrs} \hat{a}_p^\dagger \hat{a}_q^\dagger \hat{a}_r \hat{a}_s, \quad (55)$$

where the summation is over all of the  $M$  molecular basis states. The factors  $h_{pq}$  and  $h_{pqrs}$  are related to one-electron and two-electron transitions, respectively, and are calculated numerically (Yung *et al.*, 2014). The fermionic creation and annihilation operators fulfill  $\{\hat{a}, \hat{a}^\dagger\} = 1$ , which enforces the antisymmetry of the wave function. The Hamiltonian is mapped to spins (Jordan and Wigner, 1928; Bravyi and Kitaev, 2002) and the expectation values are calculated for trial wave functions of the ground state, generated via an ansatz circuit as previously described. A reference state, which represents a classical approximation to the ground state such as a Hartree-Fock solution, usually a product state, can be chosen as the initial state. A physically inspired ansatz circuit for this type of problem is the UCC (Helgaker, Jørgensen, and Olsen, 2000). The scheme prescribes a series of fermionic operators called cluster operators  $T = T_1 + T_2 + \dots + T_N$

for an  $N$ -electron system (Peruzzo *et al.*, 2014). These are essentially electron-hopping operators of increasing order that form a unitary to evolve the system into the ground state through the exploration of Hilbert space by going to increasing Hamming distances from the initial state (McClellan *et al.*, 2016),  $\hat{U}_{UCC} = e^{\theta(T-T^\dagger)}$ . Using a pseudo-time-evolution of this unitary by first-order Trotterization is a good approximation of this evolution (Yung *et al.*, 2014; Hempel *et al.*, 2018):  $\hat{U}_{UCC} \simeq \prod_i e^{\theta_i(T_i-T_i^\dagger)}$ . In the spin basis, this creates circuits of higher-order spin-spin interactions, which can be realized on a quantum computer, particularly in trapped ions via multi-ion Ising operations, or Mølmer-Sørensen (MS) gates. Classical coupled-cluster calculations can be employed to find reasonable starting values for  $\theta$  (Romero *et al.*, 2018). The computational complexity of the UCC method scales polynomially with the number of molecular orbitals  $M$ . The procedure can be repeated for different nuclear configurations to sample out the energy surface. Alternatively, a quantum phase estimation algorithm can be employed to this end (Yuan *et al.*, 2019).

We later document recent implementations of VQE with trapped ions, although VQE has also been implemented with other experimental platforms (Peruzzo *et al.*, 2014; O'Malley *et al.*, 2016; Kandala *et al.*, 2017; Colless *et al.*, 2018; Dumitrescu *et al.*, 2018; Arute *et al.*, 2020a). The VQE was implemented in trapped  $^{171}\text{Yb}^+$  ions (Shen *et al.*, 2017) to simulate the electronic structure of the molecular cation  $\text{HeH}^+$ . Instead of Ising operations, Shen *et al.* used the four available states in the ground level of a  $^{171}\text{Yb}^+$  ion coupled by microwave-driven and radio-frequency-driven transitions. The experiment matches the ground-state energy from exact diagonalization. Shen *et al.* also looked for excited states by measuring the expectation value of a changed target Hamiltonian to  $\langle(\hat{H} - \lambda\mathbb{1})^2\rangle$ . The measurement involved scanning  $\lambda$  and looking for zero-valued expectation values and resolved three out of four excited states.

Hempel *et al.* (2018) mapped two molecular problems to spins realized in chains of trapped  $^{40}\text{Ca}^+$  ions, the hydrogen molecule ( $\text{H}_2$ ), and lithium hydride ( $\text{LiH}$ ). For  $\text{H}_2$ , the molecular orbitals are formed by linear combinations of the two  $1s$  orbitals of each atom. The Bravyi-Kitaev (Bravyi and Kitaev, 2002) and Jordan-Wigner (Jordan and Wigner, 1928) encodings are used to map the problem onto two and four qubits, respectively. The former is more efficient since both the Hamiltonian and the UCC ansatz can be reduced to two qubits by appropriate choice of reference state (O'Malley *et al.*, 2016). In both mappings, the UCC operator leads to a single-parameter ansatz circuit, which is implemented using a pair of MS gates based on a technique developed by Müller *et al.* (2011). They made a full sweep of the parameter as well as a VQE optimization to map out the ground-state potential energy using a Nelder-Mead search algorithm, which was found not to converge in some instances due to the presence of noise. For the simulation of  $\text{LiH}$ , a minimal basis set for the molecular orbitals was chosen. The four electrons fill the energy-ordered orbitals, as determined by a Hartree-Fock calculation. The UCC ansatz is truncated to single and double excitations (UCCSD) and an active space of two electrons and three orbitals is identified (Kandala *et al.*, 2017). The two core electrons can be considered not to contribute to molecular

bonding (Roos, Taylor, and Sigbahn, 1980). Using the classical theory of configuration interaction of singles and doubles (Shavitt, 1984), they further reduced the active space to two singlet excitations. This active space is illustrated in Fig. 34(a). The resulting UCC unitary was mapped to spins via Bravyi-Kitaev encoding, which results in a three-qubit operator with two circuit parameters,  $\hat{U}_{\text{UCCSD}}(\alpha, \beta) = e^{-i\alpha\sigma_0^x\sigma_1^y} e^{-i\beta\sigma_0^x\sigma_2^y}$ , which was realized in the circuit shown in Fig. 34(c). Hempel *et al.* (2018) performed a grid scan of the parameters at different internuclear distances and reconstructed the potential energy curve for the electronic ground state by fitting the minimum in two ways, by Gaussian process regression (GPR) and to a 2D quadratic surface, where the latter yields good results, reproducing the well depth within statistical uncertainties; see the line plots in Fig. 34(b). Hempel *et al.* (2018) also performed a feedback VQE using a classical optimizer that incorporates elements of simulated annealing and matches the results of the grid scan, see data points in Fig. 34(b).

Nam *et al.* (2020) estimated the ground-state energy of the water molecule ( $\text{H}_2\text{O}$ ). The UCC ansatz circuits are optimized by taking advantage of an active subspace and by sorting the UCC operators into bosonic and nonbosonic excitations from the Hartree-Fock ground state. Bosonic terms refer to excitations of two electrons into a molecular orbital such that their spins pair up. These excitations can be represented by a single-qubit operation. Nonbosonic excitations are implemented via the Jordan-Wigner transformation. The resulting circuits are further optimized by term ordering (Hastings *et al.*, 2014). Nam *et al.* presented the cost of adding an increasing number of ansatz terms to the circuit in terms of qubits and MS gates [depicted in Fig. 35(a)]. Their results show that chemical accuracy can be reached with about 15 terms, which corresponds to 11 qubits and 140 MS gates. Experimentally, Nam *et al.* realized circuits with up to three terms and three qubits. The measurement results agree within errors with classical calculations, as shown in Fig. 35(b). Finally, they proposed the implementation of this simulation problem with a growing number of terms as a benchmark for quantum computing platforms (Nam *et al.*, 2020).

The VQE was used by Shehab, Landsman *et al.* (2019) to solve a nuclear physics problem, finding the binding energy of the deuteron nucleus. The nuclear interaction was modeled on pionless effective field theory following Dumitrescu *et al.* (2018). The Hamiltonian is expressed in the  $N$ -oscillator basis

$$\hat{H}_D = \sum_{n,n'=0}^{N-1} \langle n' | (\hat{T} + \hat{V}) | n \rangle \hat{a}_n^\dagger \hat{a}_n, \quad (56)$$

where the operators  $\hat{a}_n^\dagger$  and  $\hat{a}_n$  create and annihilate, respectively, a deuteron in the harmonic-oscillator  $s$ -wave state. Using finite harmonic-oscillator spaces introduces errors by imposing sharp cutoffs in both position and momentum space, called IR and UV errors. These depend on the basis size and the potential (König *et al.*, 2014). Using the Jordan-Wigner transformation (Shehab, Landsman *et al.*, 2019), one finds the qubit Hamiltonians for  $N = 2, 3$ , and 4.

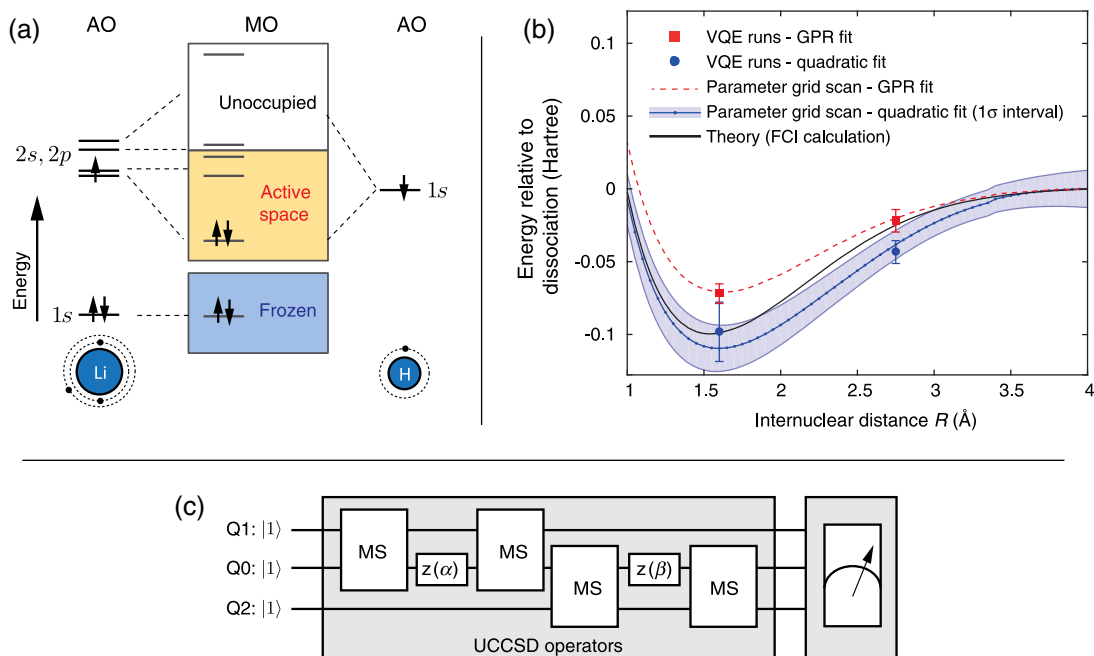


FIG. 34. Variational quantum eigensolver simulation of the lithium hydride (LiH) molecule with three trapped-ion qubits. (a) LiH molecular orbitals (MOs) formed out of atomic orbitals (AOs) contributed by each element. The active space in which the implemented UCC excitation operators act is highlighted in yellow (light gray). (b) The theoretical LiH potential energy surface calculated for the minimal basis set (black solid line) is shown in comparison to the experimentally obtained results, offset to overlap at maximum distance  $R$  to better illustrate the well-depth differences in the grid-scan reconstructions. The data points result from sampling the energy landscape using the VQE algorithm or a parameter grid scan and fitting the explored space with a GPR-based machine learning algorithm (dashed line) or a 2D quadratic fit [blue (gray) solid line]. The error bars are obtained from the fits with the underlying data weighted by quantum projection noise. (c) Abstract quantum circuit implementing each of the two target UCCSD unitary operators for the qubits indexed Q0, Q1, and Q2. A fully entangling gate (MS) acts locally between the enclosed qubits and surrounds a local qubit rotation  $z$  quantified by parameters  $\alpha$  and  $\beta$ , respectively. Adapted from Hempel *et al.*, 2018.

The value of the largest coefficient in the Hamiltonian grows with basis size  $N$  and its uncertainty bounds the overall uncertainty of the Hamiltonian expectation value. This means that increasing the basis, which already comes with more gates and qubits, also requires an increase in the number of measurements that need to be taken to reproduce the gain in model accuracy experimentally. The UCC ansatz used is based on single excitations of the different  $s$ -wave states (Lu *et al.*, 2019) and leads to an iterative scheme for circuit construction with  $N - 1$  variational parameters. Shehab, Landsman *et al.* (2019) performed a line sweep of the parameters for  $N = 4$  and measured the expectation values at theoretically optimal parameters for  $N = 2, 3$ , and 4. An error mitigation scheme was also used, based on Richardson extrapolation (Temme, Bravyi, and Gambetta, 2017; McArdle, Yuan, and Benjamin, 2019), by which each circuit is implemented with an increasing number of pairwise-canceling MS gates, i.e., 3, 5, 7, ... MS gates per actual circuit gate. These additional measurements are used to scale the noise and extrapolate the value of each Hamiltonian term to zero noise. These extrapolated values are then combined to give the final ground-state energy estimate. For the three- and four-qubit ansatz circuits the theoretical predictions lie within the error bars of the experimental results (Shehab, Landsman *et al.*, 2019).

The VQE implementation of the deuteron nuclear binding energy problem was also improved upon by Shehab, Kim

*et al.* (2019) by applying the so-called past-light-cone method to the VQE circuits. This breaks them down into minimal circuits for each term in the Hamiltonian at the cost of a larger number of measurements. Shehab, Kim *et al.* showed a significant reduction of 80% in the error of the estimated ground-state energy. This made it consistent with the theoretical value without using error mitigation.

The VQE is also applicable to condensed matter problems. Rungger *et al.* (2019) designed and implemented a variational algorithm to solve dynamical mean-field theory (DMFT) problems. DMFT is a correction to density functional theory and describes materials with strongly correlated electrons (Georges *et al.*, 1996). The model problem consists of an interacting impurity coupled to a bath and is hard to solve using classical means. After the Jordan-Wigner transformation the Hamiltonian can be expressed in terms of orbital electron creation and destruction operators, which in turn are linear combinations of Pauli operators. The number of qubits required is  $2(N_{\text{imp}} + N_{\text{bath}})$ , where  $N_{\text{imp}}$  and  $N_{\text{bath}}$  are the number of impurity and bath spin orbitals included, respectively. Rungger *et al.* (2019) used a hardware-efficient ansatz. The procedure consists of two nested optimization loops. The inner loop is a quantum-classical hybrid VQE optimization that solves for the eigenvalues based on a set of impurity Hamiltonian parameters. The outer loop is purely classical and calculates local retarded Green's functions for the original lattice model and the impurity problem. It updates these

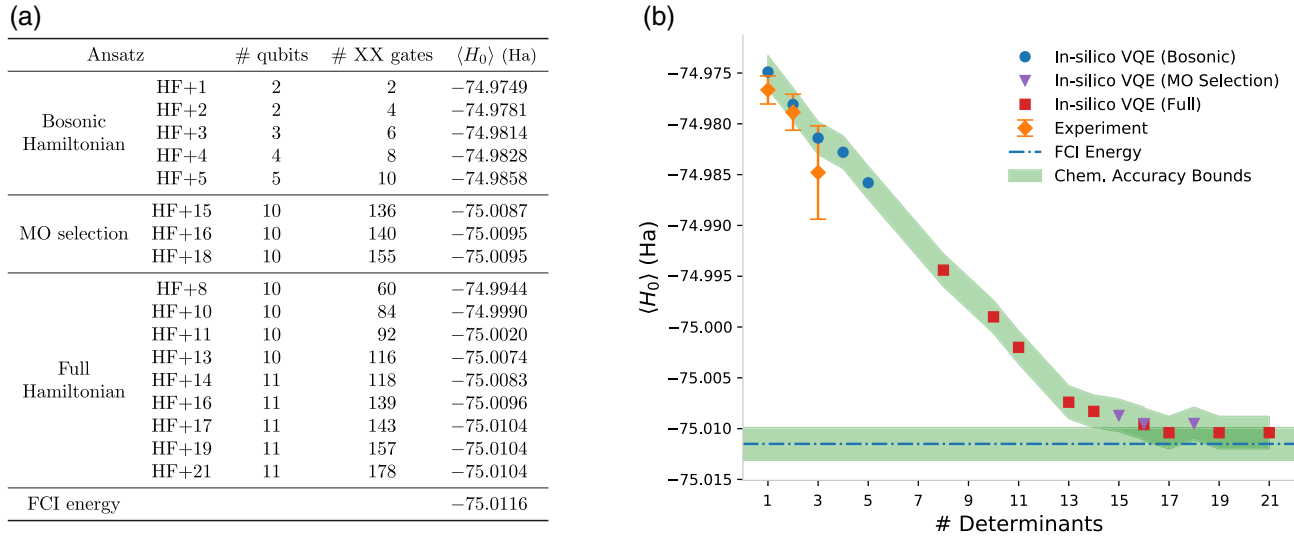


FIG. 35. VQE simulation of the ground-state energy of the water molecule ( $\text{H}_2\text{O}$ ). (a) Metrics for each circuit are labeled HF +  $N$ , as up to  $N$  of the most significant interaction terms are added to the ansatz state. The bosonic terms through HF + 5 can be represented as pair excitations to reduce the qubit resource requirements, while the MO selection strategy prunes the two least significant molecular states to reduce the qubit count slightly at the expense of accuracy at the millihartree level. Energies should be compared to the full configuration-interaction (FCI) ground-state energy, which is the exact result of diagonalizing the complete Hamiltonian in the minimal chemical basis. (b) Comparison of ground-state energy estimates as additional interactions are included in the UCC ansatz state (labeled HF +  $N$  for  $N$  significant determinants). The orange diamonds indicate experimental results from implementations with up to three qubits, with  $1\sigma$  error bars from the bootstrap distribution. The remaining points are from the *in silico* VQE simulation and show how the ansatz states converge to the full configuration-interaction ground state (indicated by the dot-dashed line). Computational error equivalent to the bound for chemical accuracy (1.6 mHa) is indicated by the shaded region. Adapted from Nam *et al.*, 2020.

parameters until a set of self-consistent impurity parameters is achieved (Liebsch and Ishida, 2012). From these, the electronic structure of the system can be calculated.

## 2. Quantum approximate optimization algorithms

The QAOA (Farhi, Goldstone, and Gutmann, 2014) is a framework for using a quantum simulator to perform tasks such as combinatorial optimization or solving satisfiability and graph problems. The QAOA can also be employed for producing highly entangled target states or finding the ground state and energy spectrum of critical Hamiltonians (Ho and Hsieh, 2019). The QAOA encodes the objective function of the optimization in a spin Hamiltonian  $H_A$ , which is applied in a bang-bang protocol followed by a noncommuting mixing operator  $H_B$  and can provide resource-efficient approximate answers, making it attractive for applications on current systems with limited gate depth or coherence time; see Fig. 36(a). The sequence is repeated  $p$  times, where each layer  $i$  is characterized by the variational parameters or angles  $(\gamma_i, \beta_i)$ , giving rise to the following evolution:

$$|\vec{\beta}, \vec{\gamma}\rangle = \prod_i^{p \leftarrow 1} e^{-i\beta_i H_B} e^{-i\gamma_i H_A} |\psi_0\rangle, \quad (57)$$

where  $|\psi_0\rangle$  is the initial state.

For certain classes of problems the QAOA has been shown to provide results that cannot be generated efficiently on a classical device (Farhi and Harrow, 2016), but in practice its performance is highly problem-dependent and

problem-instance-dependent (Willsch *et al.*, 2019). Later we highlight recent QAOA implementations in trapped ions, although there have been implementations of the QAOA in other quantum computing platforms (Otterbach *et al.*, 2017; Qiang *et al.*, 2018; Bengtsson *et al.*, 2019; Willsch *et al.*, 2019; Arute *et al.*, 2020b).

A seven-qubit digital processor based on  $^{171}\text{Yb}^+$  trapped-ion spins was used to execute a QAOA-inspired protocol (Zhu, Johri *et al.*, 2019) in order to generate a “thermofield-double” (TFD) state (Wu and Hsieh, 2019). The TFD state is a pure two-mode squeezed state that behaves as a thermal state for one mode when traced over the other mode, and it is of great interest in a number of areas of physics. These states provide a way to prepare thermal Gibbs states of a many-body Hamiltonian in a quantum simulator, which underpin phenomena like high temperature superconductivity (Lee, Nagaosa, and Wen, 2006) and quark confinement in quantum chromodynamics (Gross, Pisarski, and Yaffe, 1981). TFD states also play a key role in the holographic correspondence, where they represent so-called traversable wormholes (Gao, Jafferis, and Wall, 2017; Maldacena, Stanford, and Yang, 2017), and a number of approaches for their preparation have been proposed (Maldacena and Qi, 2018; Cottrell *et al.*, 2019; Martyn and Swingle, 2019; Wu and Hsieh, 2019). A TFD state corresponding to inverse temperature  $\beta$  is defined on a joint system of two identical Hilbert spaces  $A$  and  $B$  as

$$|\text{TFD}(\beta)\rangle = \frac{1}{Z(\beta)} \sum_n e^{-\beta E_n/2} |n\rangle_A |n\rangle_B, \quad (58)$$

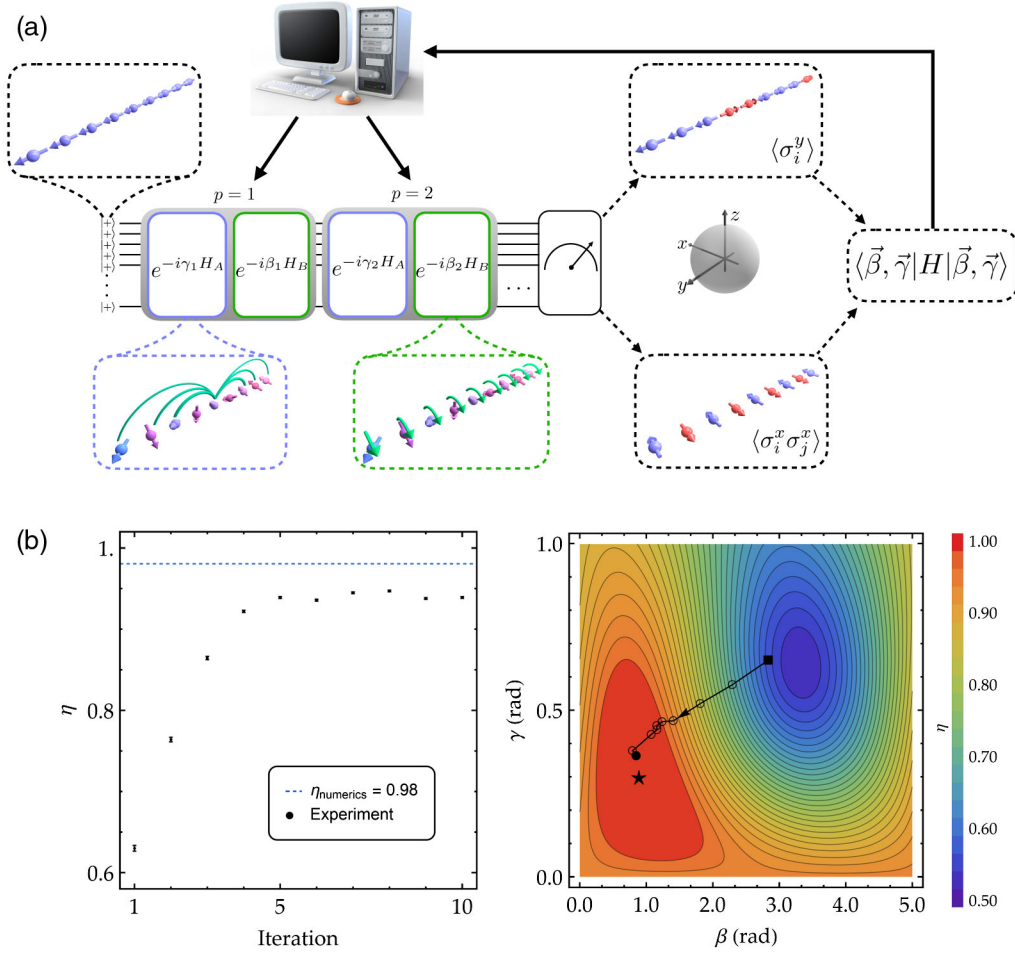


FIG. 36. QAOA applied to transverse-field long-range Ising model. (a) QAOA protocol. The system is initialized along the  $y$  direction on the Bloch sphere in the ground state of the mixing Hamiltonian  $H_B$ , namely,  $|+\rangle^{\otimes N}$ . The unitary evolution under  $H_{A(B)}$  is implemented for angles  $\gamma_i(\beta_i)$  and repeated  $p$  times. At the end of the algorithm global measurements in the  $x$  and the  $y$  basis are performed to compute the average energy  $E(\vec{\beta}, \vec{\gamma}) = \langle \vec{\beta}, \vec{\gamma} | H | \vec{\beta}, \vec{\gamma} \rangle$ . The measurement results are then processed by a classical optimization algorithm to update the variational parameters. (b) Closed-loop optimization for  $p = 1$  and  $N = 20$  qubits. Starting from an initial guess, the local gradient is approximated by performing the energy measurements along two orthogonal directions in parameter space. To quantify the performance of the QAOA, the dimensionless quantity  $\eta \equiv [E(\vec{\beta}, \vec{\gamma}) - E_{\max}] / (E_{\text{gs}} - E_{\max})$  is used, where  $E_{\max}$  ( $E_{\text{gs}}$ ) are the energies of the highest (lowest) excited state, therefore mapping the entire many-body spectrum to the  $[0, 1]$  interval. The algorithm converges after about seven iterations. Adapted from Pagano *et al.*, 2020.

where  $Z(\beta)$  is a normalization factor and  $|n\rangle_A$  and  $|n\rangle_B$  are the eigenstates in space  $A$  and  $B$  with corresponding energy  $E_n$ .

Zhu, Johri *et al.* (2019) generated a TFD state similar in form to Eq. (58) under a nearest-neighbor transverse-field Ising Hamiltonian at various temperatures, with three qubits per subsystem. Preparation starts by initializing a product of Bell-pair singlets  $|\downarrow\rangle_A |\uparrow\rangle_B - |\uparrow\rangle_A |\downarrow\rangle_B$  between pairs of  $A$  and  $B$  qubits. This is an infinite-temperature TFD state since  $\rho_A$  is maximally mixed. The evolution alternates between intersystem coupling  $H_{AB} = \sum_i X_{i,A} X_{i,B} + Z_{i,A} Z_{i,B}$  and the intrasystem Hamiltonians  $H_A + H_B$ , where  $H_A$  and  $H_B$  are identical transverse-field Ising Hamiltonians of the subsystems  $H_{XX} + gH_Z \equiv \sum_{i=1}^L X_i X_{i+1} + g \sum_{i=1}^L Z_i$ . This evolution was approximated by variational application of these Hamiltonians. The sequence was executed with theoretically optimal parameters for  $p = 1$  and found to reproduce the expected intersystem and intrasystem correlators well. Zhu,

Johri *et al.* also used a related approach (Ho, Jonay, and Hsieh, 2019) to directly prepare the zero-temperature ground state of the quantum critical transverse-field Ising model with seven trapped-ion spins using quantum-classical feedback, starting from a random point for  $p = 1$  and from the ideal parameters for  $p = 2$ .

The QAOA approach was used in an ion-trap system to approximately generate the critical ground-state energy of the long-range antiferromagnetic transverse-field Ising model [Eq. (25)] (Pagano *et al.*, 2020), where the spin-spin interaction  $J_{ij}$  is as defined in Eqs. (22) and (23) and  $B$  is the transverse field. Here we set  $H_A$  as the Ising-coupling term and  $H_B$  as the field term in Eq. (25). The QAOA was employed with up to 40 qubits in this system, using both grid search and closed-loop approaches. In the grid search approach, the entire parameter space  $(\vec{\beta}, \vec{\gamma})$  was explored experimentally to find the optimum; in the closed-loop

approach the analog trapped-ion quantum simulator was interfaced with a greedy gradient-descent algorithm to optimize the measured energy [Fig. 36(a)] starting from an initial guess. In the  $p = 1$  QAOA, the optimization trajectory in the experiment can be visualized on the theoretical performance surface as shown in Fig. 36(b).

Shehab, Kim *et al.* (2019) mapped the max-cut problem for a specific five-node graph to a five-qubit trapped-ion processor and solved it approximately using an optimized QAOA protocol that reduces circuit width and depth by splitting it into circuits for each Hamiltonian term or correlator at the cost of a larger number of measurements. For the five-node dragon graph, Shehab, Kim *et al.* reported a 36% improvement in the accuracy of the solution over the standard circuit in their system.

Finally, we note that VQS can also be used to study dynamics by employing generalizations of time-dependent variational principles (Broeckhove *et al.*, 1988) to simulate real (Li and Benjamin, 2017; Heya *et al.*, 2019) and imaginary (Chen *et al.*, 2019; Jones *et al.*, 2019; McArdle *et al.*, 2019) time evolution of pure quantum systems, as well as mixed states (Yuan *et al.*, 2019).

## VI. OUTLOOK AND FUTURE CHALLENGES

Quantum interacting spin models are among the simplest many-body quantum systems with nontrivial features that can elude classical computational approaches. Trapped atomic ion spins offer the ability to implement and control quantum spin models with tunability of the interaction form and range. Much of the research in this field has concentrated on studies of the long-range transverse Ising model, which can feature frustrated ground states with associated degeneracies and entanglement in the ground state. The many types of phase transitions and dynamical processes in this system form a fruitful test bed for studying quantum nonequilibrium processes, in many cases challenging classical computational power even for small numbers of spins. There are many extensions in this physical system to simulating more complex spin models with trapped ions such as Heisenberg couplings (Graß and Lewenstein, 2014), higher-dimensional spin models, and interactions involving three or more spins. These future directions may allow for the quantum simulation of more exotic spin phases such as spin liquids (Balents, 2010) or topological orders in spin systems such as the Haldane chain (Haldane, 1983) or the Kitaev lattice (Kitaev, 2006). There are a number of technical challenges to overcome in the path of scaling trapped-ion systems up to  $\sim 100$  qubits and beyond. However, none of these obstacles are fundamental and many groups have shown effective mitigation techniques in this growing area of research. With a single linear chain of ions, it should be possible to extend the number of ions to hundreds using anharmonic trapping potentials that generate uniform spacing and thus avoid structural phase transitions for larger ion crystals (Lin *et al.*, 2009; Pagano *et al.*, 2018). Two technical challenges include the increased sensitivity of equally spaced ion crystals to background fluctuating electric fields (Cetina *et al.*, 2020) and the shorter lifetime of the ion chain due to collisions with the background gas. Solutions to these challenges include the use of cryogenic trapped-ion

systems, which significantly lower the vacuum pressure so that storage times of hours or longer can be achieved with large ion crystals (Poitzsch *et al.*, 1996; Pagano *et al.*, 2018) and the use of sympathetic cooling with multiple species of ions in the system (Larson *et al.*, 1986; Lin *et al.*, 2009; Chou *et al.*, 2010; Pino *et al.*, 2020), allowing the background heating to be quenched without disturbing the spins in the simulation.

With a 1D ion chain, it is possible to simulate any frustrated spin graph with multiple engineered laser pulses (Korenblit *et al.*, 2012; Davoudi *et al.*, 2020). However, it is possible to further increase the number of ions in a quantum simulator by using higher-dimensional ion crystals (Wang, Shen, and Duan, 2015). The Penning trap geometry is amenable to 2D and 3D crystal structures, as discussed in this review. In a rf trap, 2D or 3D ion crystals are necessarily accompanied by significant rf micromotion for ions not positioned at a rf null (Dehmelt, 1968), which is limited to a point or a line in space. Although micromotion introduces a number of subtleties for laser cooling, gate operations, and ion detection, it is a coherent and well-controlled motion whose effects can be mitigated through proper gate design and the engineering of spin interactions (Shen, Zhang, and Duan, 2014; Wang, Shen, and Duan, 2015). Alternatively, an array of rf traps can be engineered to create multidimensional designer ion crystals (Cirac and Zoller, 2000; Kumph *et al.*, 2016), although this may require small distances between the ions and the electrodes to generate sufficiently strong spin interactions. Apart from offering an avenue to increase the ion number, 2D and 3D ion crystals provide a natural platform to realize rich frustrated spin Hamiltonians in a more complicated geometry that can match the native dimension of the underlying target spin Hamiltonian.

Finally, we note that well-known modular approaches to scaling trapped-ion systems can be directly applied to quantum spin simulations. For instance, large numbers of ions can be grouped in spatially separated modules, where each module contains many trapped-ion spins with the Coulomb-mediated spin-spin couplings discussed in Sec. I. Here the system is scaled by shuttling subsets of ions between modules to extend the size of the system (Kielpinski, Monroe, and Wineland, 2002; Pino *et al.*, 2020). Because the idle spin states are nearly perfectly decoupled from ion motion between modules, the scaling procedure is largely a systems engineering task. Ultimately, separated modules of trapped-ion crystals can also be connected via heralded photonic interconnects, even between separated trap structures, for a remote modular scalable architecture (Duan and Monroe, 2010; Li and Benjamin, 2012; Monroe *et al.*, 2014).

Useful quantum simulations should have unambiguous benchmarks to indicate performance beyond what is possible with classical computational simulation. As opposed to recent simulations of random quantum circuit evolution (Arute *et al.*, 2019), we desire a benchmark that also indicates the usefulness of the underlying problem. When we use a quantum simulator to probe the ground state of a quantum many-body Hamiltonian, for instance, a possible heuristic benchmark could be the ground-state variational energy of the Hamiltonian. Although in general there is no quantum algorithm to guarantee that we can successfully find the

genuine ground state of a many-body Hamiltonian, the associated variational energy of the approximate ground state realized by a quantum simulator can always be efficiently measured by the experimental setup. If such a measured energy is lower than the energy obtained by any classical simulation even with the most powerful computers, it is an indication that the quantum simulator finds a useful solution that better approximates the ground state of the target Hamiltonian than any known classical method. There is a close relationship between spin simulations and quantum computations with qubits, and the underlying mechanism behind the Ising couplings in trapped-ion spin simulations is exactly that used for discrete quantum gates between trapped-ion qubits (Sørensen and Mølmer, 2000), which are sometimes called Ising gates. Quantum simulations in this sense can be considered a special case of quantum computation, and we expect that as trapped-ion quantum computers scale in the future (Monroe and Kim, 2013; Brown, Kim, and Monroe, 2016; Wright *et al.*, 2019; Pino *et al.*, 2020), so will the reach of trapped-ion quantum spin simulators.

## ACKNOWLEDGMENTS

We acknowledge key collaborations with Patrick Becker, Howard Carmichael, Ming-Shien Chang, Itzak Cohen, Katherine Collins, Arinjoy De, Emily Edwards, Lei Feng, Michael Foss-Feig, James Freericks, Mohammad Hafezi, Phillip Hauke, Markus Heyl, David Huse, Dvir Kafri, Harvey Kaplan, Simcha Korenblit, Antonis Kyprianidis, Aaron Lee, Guin-Dar Lin, Mohammad Maghrebi, Brian Neyenhuis, Nhung H. Nguyen, Changsuk Noh, Andrew Potter, Alex Retzker, Jacob Smith, Wen-Lin Tan, Ashvin Vishwanath, C.-C. Joseph Wang, and Jiehang Zhang. We thank R. Blatt, J. Bollinger, T. Schätz, and C. Wunderlich for discussions.

## REFERENCES

- Abanin, Dmitry A., Ehud Altman, Immanuel Bloch, and Maksym Serbyn, 2019, “Colloquium: Many-body localization, thermalization, and entanglement,” *Rev. Mod. Phys.* **91**, 021001.
- Abanin, Dmitry A., Wojciech De Roeck, and François Huvener, 2016, “Theory of many-body localization in periodically driven systems,” *Ann. Phys. (Amsterdam)* **372**, 1–11.
- Acín, A., A. Andrianov, E. Jané, and R. Tarrach, 2001, “Three-qubit pure-state canonical forms,” *J. Phys. A* **34**, 6725–6739.
- Acton, M., K.-A. Brickman, P. C. Haljan, P. J. Lee, L. Deslauriers, and C. Monroe, 2006, “Near-perfect simultaneous measurement of a qubit register,” *Quantum Inf. Comput.* **6**, 465.
- Ajisaka, Shigeru, Felipe Barra, and Bojan Žunkovič, 2014, “Nonequilibrium quantum phase transitions in the XY model: Comparison of unitary time evolution and reduced density operator approaches,” *New J. Phys.* **16**, 033028.
- Albasha, Tameem, and Daniel A. Lidar, 2018, “Adiabatic quantum computation,” *Rev. Mod. Phys.* **90**, 015002.
- An, Shuoming, Jing-Ning Zhang, Mark Um, Dingshun Lv, Yao Lu, Junhua Zhang, Zhang-Qi Yin, H. T. Quan, and Kihwan Kim, 2015, “Experimental test of the quantum Jarzynski equality with a trapped-ion system,” *Nat. Phys.* **11**, 193–199.
- Anderson, P. W., 1958, “Absence of diffusion in certain random lattices,” *Phys. Rev.* **109**, 1492–1505.
- Arute, Frank, *et al.*, 2019, “Quantum supremacy using a programmable superconducting processor,” *Nature (London)* **574**, 505–510.
- Arute, Frank, *et al.*, 2020a, “Hartree-Fock on a superconducting qubit quantum computer,” [arXiv:2004.04174](https://arxiv.org/abs/2004.04174).
- Arute, Frank, *et al.*, 2020b, “Quantum approximate optimization of non-planar graph problems on a planar superconducting processor,” [arXiv:2004.04197](https://arxiv.org/abs/2004.04197).
- Aspuru-Guzik, Alán, Anthony D. Dutoi, Peter J. Love, and Martin Head-Gordon, 2005, “Simulated quantum computation of molecular energies,” *Science* **309**, 1704–1707.
- Babbush, Ryan, Dominic W. Berry, Yuval R. Sanders, Ian D. Kivlichan, Artur Scherer, Annie Y. Wei, Peter J. Love, and Alán Aspuru-Guzik, 2018, “Exponentially more precise quantum simulation of fermions in the configuration interaction representation,” *Quantum Sci. Technol.* **3**, 015006.
- Bachelard, Romain, and Michael Kastner, 2013, “Universal Threshold for the Dynamical Behavior of Lattice Systems with Long-Range Interactions,” *Phys. Rev. Lett.* **110**, 170603.
- Bak, Per, and R. Bruinsma, 1982, “One-Dimensional Ising Model and the Complete Devil’s Staircase,” *Phys. Rev. Lett.* **49**, 249.
- Balasubramanian, S., Shuyang Han, B. T. Yoshimura, and J. K. Freericks, 2018, “Bang-bang shortcut to adiabaticity in trapped-ion quantum simulators,” *Phys. Rev. A* **97**, 022313.
- Balents, Leon, 2010, “Spin liquids in frustrated magnets,” *Nature (London)* **464**, 199–208.
- Balian, R., and M. Vénéroni, 1988, “Static and dynamic variational principles for expectation values of observables,” *Ann. Phys. (N.Y.)* **187**, 29–78.
- Bañuls, M. C., *et al.*, 2019, “Simulating lattice gauge theories within quantum technologies,” [arXiv:1911.00003](https://arxiv.org/abs/1911.00003).
- Barderson, Jens H., Frank Pollmann, and Joel E. Moore, 2012, “Unbounded Growth of Entanglement in Models of Many-Body Localization,” *Phys. Rev. Lett.* **109**, 017202.
- Barreiro, Julio T., Markus Müller, Philipp Schindler, Daniel Nigg, Thomas Monz, Michael Chwalla, Markus Hennrich, Christian F. Roos, Peter Zoller, and Rainer Blatt, 2011, “An open-system quantum simulator with trapped ions,” *Nature (London)* **470**, 486.
- Baugh, Jonathan, Osama Moussa, Colm A Ryan, Ashwin Nayak, and Raymond Laflamme, 2005, “Experimental implementation of heat-bath algorithmic cooling using solid-state nuclear magnetic resonance,” *Nature (London)* **438**, 470.
- Bengtsson, Andreas, *et al.*, 2019, “Quantum approximate optimization of the exact-cover problem on a superconducting quantum processor,” [arXiv:1912.10495](https://arxiv.org/abs/1912.10495).
- Benhelm, J., G. Kirchmair, C. F. Roos, and R. Blatt, 2008, “Towards fault-tolerant quantum computing with trapped ions,” *Nat. Phys.* **4**, 463–466.
- Ben-Kish, A., *et al.*, 2003, “Experimental Demonstration of a Technique to Generate Arbitrary Quantum Superposition States of a Harmonically Bound Spin-1/2 Particle,” *Phys. Rev. Lett.* **90**, 037902.
- Berges, J., Sz. Borsányi, and C. Wetterich, 2004, “Prethermalization,” *Phys. Rev. Lett.* **93**, 142002.
- Bergquist, J. C., Randall G. Hulet, Wayne M. Itano, and D. J. Wineland, 1986, “Observation of Quantum Jumps in a Single Atom,” *Phys. Rev. Lett.* **57**, 1699–1702.
- Bernien, Hannes, *et al.*, 2017, “Probing many-body dynamics on a 51-atom quantum simulator,” *Nature (London)* **551**, 579.
- Berry, Dominic W., Andrew M. Childs, Richard Cleve, Robin Kothari, and Rolando D. Somma, 2015, “Simulating Hamiltonian Dynamics with a Truncated Taylor Series,” *Phys. Rev. Lett.* **114**, 090502.

- Binder, K., and A. P. Young, 1986, “Spin glasses: Experimental facts, theoretical concepts, and open questions,” *Rev. Mod. Phys.* **58**, 801–976.
- Blatt, R., and C. F. Roos, 2012, “Quantum simulations with trapped ions,” *Nat. Phys.* **8**, 277–284.
- Bloch, Immanuel, Jean Dalibard, and Wilhelm Zwerger, 2008, “Many-body physics with ultracold gases,” *Rev. Mod. Phys.* **80**, 885.
- Bohnet, Justin G., Brian C. Sawyer, Joseph W. Britton, Michael L. Wall, Ana Maria Rey, Michael Foss-Feig, and John J. Bollinger, 2016, “Quantum spin dynamics and entanglement generation with hundreds of trapped ions,” *Science* **352**, 1297–1301.
- Bordia, Pranjal, Henrik Lüschen, Sebastian Scherg, Sarang Gopalakrishnan, Michael Knap, Ulrich Schneider, and Immanuel Bloch, 2017, “Probing Slow Relaxation and Many-Body Localization in Two-Dimensional Quasiperiodic Systems,” *Phys. Rev. X* **7**, 041047.
- Bordia, Pranjal, Henrik P. Lüschen, Sean S. Hodgman, Michael Schreiber, Immanuel Bloch, and Ulrich Schneider, 2016, “Coupling Identical One-Dimensional Many-Body Localized Systems,” *Phys. Rev. Lett.* **116**, 140401.
- Bravyi, S., M. B. Hastings, and F. Verstraete, 2006, “Lieb-Robinson Bounds and the Generation of Correlations and Topological Quantum Order,” *Phys. Rev. Lett.* **97**, 050401.
- Bravyi, S., and A. Kitaev, 2002, “Fermionic quantum computation,” *Ann. Phys. (Amsterdam)* **298**, 210–226.
- Bravyi, Sergey, Jay M. Gambetta, Antonio Mezzacapo, and Kristan Temme, 2017, “Tapering off qubits to simulate fermionic Hamiltonians,” [arXiv:1701.08213](https://arxiv.org/abs/1701.08213).
- Britton, Joseph W., Brian C. Sawyer, Adam C. Keith, C.-C. Joseph Wang, James K. Freericks, Hermann Uys, Michael J. Biercuk, and John J. Bollinger, 2012, “Engineered two-dimensional Ising interactions in a trapped-ion quantum simulator with hundreds of spins,” *Nature (London)* **484**, 489–492.
- Broeckhove, J., L. Lathouwers, E. Kesteloot, and P. Van Leuven, 1988, “On the equivalence of time-dependent variational principles,” *Chem. Phys. Lett.* **149**, 547–550.
- Brown, K. R., J. Kim, and C. Monroe, 2016, “Co-designing a scalable quantum computer with trapped atomic ions,” *npj Quantum Inf.* **2**, 16034.
- Brown, Kenneth R., Robert J. Clark, and Isaac L. Chuang, 2006, “Limitations of Quantum Simulation Examined by Simulating a Pairing Hamiltonian Using Nuclear Magnetic Resonance,” *Phys. Rev. Lett.* **97**, 050504.
- Brown, Lowell S., and Gerald Gabrielse, 1986, “Geonium theory: Physics of a single electron or ion in a Penning trap,” *Rev. Mod. Phys.* **58**, 233–311.
- Brydges, Tiff, Andreas Elben, Petar Jurcevic, Benoît Vermersch, Christine Maier, Ben P. Lanyon, Peter Zoller, Rainer Blatt, and Christian F. Roos, 2019, “Probing Rényi entanglement entropy via randomized measurements,” *Science* **364**, 260–263.
- Bukov, Marin, Luca D’Alessio, and Anatoli Polkovnikov, 2015, “Universal high-frequency behavior of periodically driven systems: From dynamical stabilization to Floquet engineering,” *Adv. Phys.* **64**, 139–226.
- Burin, Alexander L., 2006, “Energy delocalization in strongly disordered systems induced by the long-range many-body interaction,” [arXiv:cond-mat/0611387](https://arxiv.org/abs/cond-mat/0611387).
- Burin, Alexander L., 2015, “Localization in a random XY model with long-range interactions: Intermediate case between single-particle and many-body problems,” *Phys. Rev. B* **92**, 104428.
- Buyskikh, Anton S., Maurizio Fagotti, Johannes Schachenmayer, Fabian Essler, and Andrew J. Daley, 2016, “Entanglement growth and correlation spreading with variable-range interactions in spin and fermionic tunneling models,” *Phys. Rev. A* **93**, 053620.
- Byrnes, T. M. R., P. Sriganesh, R. J. Bursill, and C. J. Hamer, 2002, “Density matrix renormalization group approach to the massive Schwinger model,” *Phys. Rev. D* **66**, 013002.
- Calarco, T., Rosario Fazio, and P. Mataloni, 2018, *Quantum Simulators*, Vol. 198 (IOS Press, Amsterdam).
- Caneva, Tommaso, Rosario Fazio, and Giuseppe E. Santoro, 2008, “Adiabatic quantum dynamics of the Lipkin-Meshkov-Glick model,” *Phys. Rev. B* **78**, 104426.
- Cayssol, Jérôme, Balázs Dóra, Ferenc Simon, and Roderich Moessner, 2013, “Floquet topological insulators,” *Phys. Status Solidi RRL* **7**, 101–108.
- Cetina, M., L. N. Egan, C. A. Noel, M. L. Goldman, A. R. Risinger, D. Zhu, D. Biswas, and C. Monroe, 2020, “Quantum gates on individually-addressed atomic qubits subject to noisy transverse motion,” [arXiv:2007.06768](https://arxiv.org/abs/2007.06768).
- Cevolani, Lorenzo, Giuseppe Carleo, and Laurent Sanchez-Palencia, 2015, “Protected quasilocality in quantum systems with long-range interactions,” *Phys. Rev. A* **92**, 041603.
- Cevolani, Lorenzo, Giuseppe Carleo, and Laurent Sanchez-Palencia, 2016, “Spreading of correlations in exactly solvable quantum models with long-range interactions in arbitrary dimensions,” *New J. Phys.* **18**, 093002.
- Cevolani, Lorenzo, Julien Despres, Giuseppe Carleo, Luca Tagliacozzo, and Laurent Sanchez-Palencia, 2018, “Universal scaling laws for correlation spreading in quantum systems with short- and long-range interactions,” *Phys. Rev. B* **98**, 024302.
- Chandrashekar, C. M., Subhashish Banerjee, and R. Srikanth, 2010, “Relationship between quantum walks and relativistic quantum mechanics,” *Phys. Rev. A* **81**, 062340.
- Chen, Chi-Fang, and Andrew Lucas, 2019, “Finite Speed of Quantum Scrambling with Long Range Interactions,” *Phys. Rev. Lett.* **123**, 250605.
- Chen, Ming-Cheng, *et al.*, 2019, “Demonstration of adiabatic variational quantum computing with a superconducting quantum coprocessor,” [arXiv:1905.03150](https://arxiv.org/abs/1905.03150).
- Chen, Xiao, and Tianci Zhou, 2019, “Quantum chaos dynamics in long-range power law interaction systems,” *Phys. Rev. B* **100**, 064305.
- Chen, Xiao, Tianci Zhou, and Cenke Xu, 2018, “Measuring the distance between quantum many-body wave functions,” *J. Stat. Mech.* 073101.
- Cheneau, Marc, Peter Barnettler, Dario Poletti, Manuel Endres, Peter Schausz, Takeshi Fukuhara, Christian Gross, Immanuel Bloch, Corinna Kollath, and Stefan Kuhr, 2012, “Light-cone-like spreading of correlations in a quantum many-body system,” *Nature (London)* **481**, 484.
- Childs, A. M., R. Cleve, E. Deotto, E. Farhi, S. Gutmann, and D. A. Spielman, 2003, “Exponential algorithmic speedup by a quantum walk,” in *Proceedings of the Thirty-Fifth Annual ACM Symposium on Theory of Computing (STOC ’03), San Diego, 2003* (ACM, New York), pp. 259–267.
- Choi, Jae-yoon, Sebastian Hild, Johannes Zeiher, Peter Schauf, Antonio Rubio-Abadal, Tarik Yefsah, Vedika Khemani, David A. Huse, Immanuel Bloch, and Christian Gross, 2016, “Exploring the many-body localization transition in two dimensions,” *Science* **352**, 1547–1552.
- Choi, Joonhee, *et al.*, 2017, “Depolarization Dynamics in a Strongly Interacting Solid-State Spin Ensemble,” *Phys. Rev. Lett.* **118**, 093601.
- Choi, Soonwon, *et al.*, 2017, “Observation of discrete time-crystalline order in a disordered dipolar many-body system,” *Nature (London)* **543**, 221.



- Chou, C. W., D. B. Hume, J. C. J. Koelemeij, D. J. Wineland, and T. Rosenband, 2010, “Frequency Comparison of Two High-Accuracy  $Al^+$  Optical Clocks,” *Phys. Rev. Lett.* **104**, 070802.
- Christensen, Justin E., David Hucul, Wesley C. Campbell, and Eric R. Hudson, 2020, “High-fidelity manipulation of a qubit enabled by a manufactured nucleus,” *npj Quantum Inf.* **6**, 35.
- Cirac, J. I., and P. Zoller, 1995, “Quantum Computation with Cold Trapped Ions,” *Phys. Rev. Lett.* **74**, 4091–4094.
- Cirac, J. I., and P. Zoller, 2000, “A scalable quantum computer with ions in an array of microtraps,” *Nature (London)* **404**, 579–581.
- Cirac, J. Ignacio, and Peter Zoller, 2012, “Goals and opportunities in quantum simulation,” *Nat. Phys.* **8**, 264–266.
- Cirstoiu, Cristina, Zoe Holmes, Joseph Iosue, Lukasz Cincio, Patrick J. Coles, and Andrew Sornborger, 2019, “Variational fast forwarding for quantum simulation beyond the coherence time,” *arXiv:1910.04292*.
- Clark, Craig R., Tzvetan S. Metodi, Samuel D. Gasster, and Kenneth R. Brown, 2009, “Resource requirements for fault-tolerant quantum simulation: The ground state of the transverse Ising model,” *Phys. Rev. A* **79**, 062314.
- Cohen, I., P. Richerme, Z.-X. Gong, C. Monroe, and A. Retzker, 2015, “Simulating the Haldane phase in trapped-ion spins using optical fields,” *Phys. Rev. A* **92**, 012334.
- Colless, J. I., V. V. Ramasesh, D. Dahlen, M. S. Blok, M. E. Kimchi-Schwartz, J. R. McClean, J. Carter, W. A. de Jong, and I. Siddiqi, 2018, “Computation of Molecular Spectra on a Quantum Processor with an Error-Resilient Algorithm,” *Phys. Rev. X* **8**, 011021.
- Cottrell, William, Ben Freivoegel, Diego M. Hofman, and Sagar F. Lokhande, 2019, “How to build the thermofield double state,” *J. High Energy Phys.* **02**, 58.
- D’Alessio, Luca, Yariv Kafri, Anatoli Polkovnikov, and Marcos Rigol, 2016, “From quantum chaos and eigenstate thermalization to statistical mechanics and thermodynamics,” *Adv. Phys.* **65**, 239–362.
- Damski, Bogdan, and Wojciech H. Zurek, 2006, “Adiabatic-impulse approximation for avoided level crossings: From phase-transition dynamics to Landau-Zener evolutions and back again,” *Phys. Rev. A* **73**, 063405.
- Das, Arnab, and Bikas K. Chakrabarti, 2008, “Colloquium: Quantum annealing and analog quantum computation,” *Rev. Mod. Phys.* **80**, 1061–1081.
- Davoudi, Zohreh, Mohammad Hafezi, Christopher Monroe, Guido Pagano, Alireza Seif, and Andrew Shaw, 2020, “Towards analog quantum simulations of lattice gauge theories with trapped ions,” *Phys. Rev. Research* **2**, 023015.
- Debnath, S., M. N. Linke, S.-T. Wang, C. Figgatt, A. K. Landsman, L.-M. Duan, and C. Monroe, 2018, “Observation of Hopping and Blockade of Bosons in a Trapped Ion Spin Chain,” *Phys. Rev. Lett.* **120**, 073001.
- Dehmelt, Hans, 1968, “Radiofrequency spectroscopy of stored ions I: Storage,” *Adv. At. Mol. Phys.* **3**, 53–72.
- de Léséleuc, Sylvain, Vincent Lienhard, Pascal Scholl, Daniel Barredo, Sebastian Weber, Nicolai Lang, Hans Peter Büchler, Thierry Lahaye, and Antoine Browaeys, 2019, “Observation of a symmetry-protected topological phase of interacting bosons with Rydberg atoms,” *Science* **365**, 775.
- Deng, Chunqing, Jean-Luc Orgiazzi, Feiruo Shen, Sahel Ashhab, and Adrian Lupascu, 2015, “Observation of Floquet States in a Strongly Driven Artificial Atom,” *Phys. Rev. Lett.* **115**, 133601.
- Deng, X.-L., D. Porras, and J. I. Cirac, 2005, “Effective spin quantum phases in systems of trapped ions,” *Phys. Rev. A* **72**, 063407.
- den Nijs, Marcel, and Koos Rommelse, 1989, “Preroughening transitions in crystal surfaces and valence-bond phases in quantum spin chains,” *Phys. Rev. B* **40**, 4709.
- De Roeck, Wojciech, and John Z. Imbrie, 2017, “Many-body localization: Stability and instability,” *Phil. Trans. R. Soc. A* **375**, 20160422.
- Deutsch, J. M., 1991, “Quantum statistical mechanics in a closed system,” *Phys. Rev. A* **43**, 2046–2049.
- Di Molfetta, G., and A. Pérez, 2016, “Quantum walks as simulators of neutrino oscillations in a vacuum and matter,” *New J. Phys.* **18**, 103038.
- Ding, Shiqian, Gleb Maslennikov, Roland Häublitzel, and Dmitry Matsukevich, 2018, “Quantum Simulation with a Trilinear Hamiltonian,” *Phys. Rev. Lett.* **121**, 130502.
- Duan, L.-M., and C. Monroe, 2010, “Colloquium: Quantum networks with trapped ions,” *Rev. Mod. Phys.* **82**, 1209–1224.
- Dumitrescu, E. F., A. J. McCaskey, G. Hagen, G. R. Jansen, T. D. Morris, T. Papenbrock, R. C. Pooser, D. J. Dean, and P. Lougovski, 2018, “Cloud Quantum Computing of an Atomic Nucleus,” *Phys. Rev. Lett.* **120**, 210501.
- Edwards, E. E., S. Korenblit, K. Kim, R. Islam, M.-S. Chang, J. K. Freericks, G.-D. Lin, L.-M. Duan, and C. Monroe, 2010, “Quantum simulation and phase diagram of the transverse-field Ising model with three atomic spins,” *Phys. Rev. B* **82**, 060412.
- Eisert, Jens, Mauritz van den Worm, Salvatore R. Manmana, and Michael Kastner, 2013, “Breakdown of Quasilocality in Long-Range Quantum Lattice Models,” *Phys. Rev. Lett.* **111**, 260401.
- Eldredge, Zachary, Zhe-Xuan Gong, Jeremy T. Young, Ali Hamed Moosavian, Michael Foss-Feig, and Alexey V. Gorshkov, 2017, “Fast Quantum State Transfer and Entanglement Renormalization Using Long-Range Interactions,” *Phys. Rev. Lett.* **119**, 170503.
- Else, Dominic V., Bela Bauer, and Chetan Nayak, 2016, “Floquet Time Crystals,” *Phys. Rev. Lett.* **117**, 090402.
- Else, Dominic V., Bela Bauer, and Chetan Nayak, 2017, “Prethermal Phases of Matter Protected by Time-Translation Symmetry,” *Phys. Rev. X* **7**, 011026.
- Else, Dominic V., Francisco Machado, Chetan Nayak, and Norman Y. Yao, 2020, “Improved Lieb-Robinson bound for many-body Hamiltonians with power-law interactions,” *Phys. Rev. A* **101**, 022333.
- Else, Dominic V., Christopher Monroe, Chetan Nayak, and Norman Y. Yao, 2020, “Discrete time crystals,” *Annu. Rev. Condens. Matter Phys.* **11**, 467–499.
- Farhi, E., J. Goldstone, and S. Gutmann, 2014, “A quantum approximate optimization algorithm,” *arXiv:1411.4028*.
- Farhi, Edward, Jeffrey Goldstone, Sam Gutmann, and Michael Sipser, 2000, “Quantum computation by adiabatic evolution,” *arXiv:quant-ph/0001106*.
- Farhi, Edward, and Aram W Harrow, 2016, “Quantum supremacy through the quantum approximate optimization algorithm,” *arXiv:1602.07674*.
- Feynman, Richard, 1982, “Simulating physics with computers,” *Int. J. Theor. Phys.* **21**, 467–488.
- Floquet, Gaston, 1883, “On linear differential equations with periodic coefficients,” *Ann. Sci. Ec. Norm. Sup.* **12**, 47–88.
- Foss-Feig, Michael, Zhe-Xuan Gong, Charles W. Clark, and Alexey V. Gorshkov, 2015, “Nearly Linear Light Cones in Long-Range Interacting Quantum Systems,” *Phys. Rev. Lett.* **114**, 157201.
- Foulkes, W. M. C., L. Mitas, R. J. Needs, and G. Rajagopal, 2001, “Quantum Monte Carlo simulations of solids,” *Rev. Mod. Phys.* **73**, 33–83.

- Frérot, Irénée, Piero Naldesi, and Tommaso Roscilde, 2018, “Multi-speed Prethermalization in Quantum Spin Models with Power-Law Decaying Interactions,” *Phys. Rev. Lett.* **120**, 050401.
- Friedenauer, Axel, Hector Schmitz, Jan Tibor Glueckert, Diego Porras, and Tobias Schätz, 2008, “Simulating a quantum magnet with trapped ions,” *Nat. Phys.* **4**, 757.
- Friis, Nicolai, *et al.*, 2018, “Observation of Entangled States of a Fully Controlled 20-Qubit System,” *Phys. Rev. X* **8**, 021012.
- Gao, Ping, Daniel Louis Jafferis, and Aron C. Wall, 2017, “Traversable wormholes via a double trace deformation,” *J. High Energy Phys.* **12**, 151.
- Gärtner, Martin, Justin G. Bohnet, Arghavan Safavi-Naini, Michael L. Wall, John J. Bollinger, and Ana Maria Rey, 2017, “Measuring out-of-time-order correlations and multiple quantum spectra in a trapped-ion quantum magnet,” *Nat. Phys.* **13**, 781.
- Gattringer, Christof, and Christian B. Lang, 2010, *Quantum Chromodynamics on the Lattice* (Springer, New York).
- Georges, Antoine, Gabriel Kotliar, Werner Krauth, and Marcelo J. Rozenberg, 1996, “Dynamical mean-field theory of strongly correlated fermion systems and the limit of infinite dimensions,” *Rev. Mod. Phys.* **68**, 13–125.
- Gerritsma, R., G. Kirchmair, F. Zähringer, E. Solano, R. Blatt, and C. F. Roos, 2010, “Quantum simulation of the Dirac equation,” *Nature (London)* **463**, 68–71.
- Glauber, Roy J., 1963, “Coherent and incoherent states of the radiation field,” *Phys. Rev.* **131**, 2766–2788.
- Goldman, Nathan, G. Juzeliūnas, P. Öhberg, and Ian B. Spielman, 2014, “Light-induced gauge fields for ultracold atoms,” *Rep. Prog. Phys.* **77**, 126401.
- Gong, Z.-X., Mohammad F. Maghrebi, Anzi Hu, Michael Foss-Feig, Phillip Richerme, Christopher Monroe, and Alexey V. Gorshkov, 2016, “Kaleidoscope of quantum phases in a long-range interacting spin-1 chain,” *Phys. Rev. B* **93**, 205115.
- Gong, Zhe-Xuan, and L.-M. Duan, 2013, “Prethermalization and dynamic phase transition in an isolated trapped ion spin chain,” *New J. Phys.* **15**, 113051.
- Gong, Zhe-Xuan, Michael Foss-Feig, Spyridon Michalakis, and Alexey V. Gorshkov, 2014a, “Persistence of Locality in Systems with Power-Law Interactions,” *Phys. Rev. Lett.* **113**, 030602.
- Gong, Zhe-Xuan, Michael Foss-Feig, Spyridon Michalakis, and Alexey V. Gorshkov, 2014b, “Persistence of locality in systems with power-law interactions,” *arXiv:1401.6174v1*.
- Gorman, Dylan J., Boerge Hemmerling, Eli Megidish, Soenke A. Moeller, Philipp Schindler, Mohan Sarovar, and Hartmut Haeflner, 2018, “Engineering Vibrationally Assisted Energy Transfer in a Trapped-Ion Quantum Simulator,” *Phys. Rev. X* **8**, 011038.
- Gottesman, Daniel, 1998, “Theory of fault-tolerant quantum computation,” *Phys. Rev. A* **57**, 127.
- Graß, Tobias, and Maciej Lewenstein, 2014, “Trapped-ion quantum simulation of tunable-range Heisenberg chains,” *Eur. Phys. J. Quantum Technol.* **1**, 8.
- Gring, M., M. Kuhnert, T. Langen, T. Kitagawa, B. Rauer, M. Schreitl, I. Mazets, D. Adu Smith, E. Demler, and J. Schmiedmayer, 2012, “Relaxation and prethermalization in an isolated quantum system,” *Science* **337**, 1318–1322.
- Gross, Christian, and Immanuel Bloch, 2017, “Quantum simulations with ultracold atoms in optical lattices,” *Science* **357**, 995–1001.
- Gross, David J., Robert D. Pisarski, and Laurence G. Yaffe, 1981, “QCD and instantons at finite temperature,” *Rev. Mod. Phys.* **53**, 43–80.
- Guardado-Sanchez, Elmer, Peter T. Brown, Debayan Mitra, Trithip Devakul, David A. Huse, Peter Schauß, and Waseem S. Bakr, 2018, “Probing the Quench Dynamics of Antiferromagnetic Correlations in a 2D Quantum Ising Spin System,” *Phys. Rev. X* **8**, 021069.
- Gühne, Otfried, and Géza Tóth, 2009, “Entanglement detection,” *Phys. Rep.* **474**, 1–75.
- Guo, Andrew Y., Minh C. Tran, Andrew M. Childs, Alexey V. Gorshkov, and Zhe-Xuan Gong, 2019, “Signaling and scrambling with strongly long-range interactions,” *arXiv:1906.02662*.
- Häffner, H., S. Gulde, M. Riebe, G. Lancaster, C. Becher, J. Eschner, F. Schmidt-Kaler, and R. Blatt, 2003, “Precision Measurement and Compensation of Optical Stark Shifts for an Ion-Trap Quantum Processor,” *Phys. Rev. Lett.* **90**, 143602.
- Haldane, F. D. M., 1983, “Nonlinear Field Theory of Large-Spin Heisenberg Antiferromagnets: Semiclassically Quantized Solitons of the One-Dimensional Easy-Axis Néel State,” *Phys. Rev. Lett.* **50**, 1153–1156.
- Haljan, P. C., K.-A. Brickman, L. Deslauriers, P. J. Lee, and C. Monroe, 2005, “Spin-Dependent Forces on Trapped Ions for Phase-Stable Quantum Gates and Entangled States of Spin and Motion,” *Phys. Rev. Lett.* **94**, 153602.
- Hamer, C. J., Zheng Weihong, and J. Oitmaa, 1997, “Series expansions for the massive Schwinger model in Hamiltonian lattice theory,” *Phys. Rev. D* **56**, 55–67.
- Hangleiter, D., M. Kliesch, M. Schwarz, and J. Eisert, 2017, “Direct certification of a class of quantum simulations,” *Quantum Sci. Technol.* **2**, 015004.
- Happer, William, 1972, “Optical pumping,” *Rev. Mod. Phys.* **44**, 169–249.
- Hastings, Matthew B., and Tohru Koma, 2006, “Spectral gap and exponential decay of correlations,” *Commun. Math. Phys.* **265**, 781.
- Hastings, Matthew B., Dave Wecker, Bela Bauer, and Matthias Troyer, 2014, “Improving quantum algorithms for quantum chemistry,” *Quantum Inf. Comput.* **15**, 1–21.
- Hauke, P., and L. Tagliacozzo, 2013, “Spread of Correlations in Long-Range Interacting Quantum Systems,” *Phys. Rev. Lett.* **111**, 207202.
- Hauke, Philipp, Fernando M. Cucchietti, Luca Tagliacozzo, Ivan Deutsch, and Maciej Lewenstein, 2012, “Can one trust quantum simulators?,” *Rep. Prog. Phys.* **75**, 082401.
- Hauke, Philipp, and Markus Heyl, 2015, “Many-body localization and quantum ergodicity in disordered long-range Ising models,” *Phys. Rev. B* **92**, 134204.
- Hayes, David, Steven T. Flammia, and Michael J. Biercuk, 2014, “Programmable quantum simulation by dynamic Hamiltonian engineering,” *New J. Phys.* **16**, 083027.
- Hazzard, Kaden R. A., Salvatore R. Manmana, Michael Foss-Feig, and Ana Maria Rey, 2013, “Far-from-Equilibrium Quantum Magnetism with Ultracold Polar Molecules,” *Phys. Rev. Lett.* **110**, 075301.
- Hazzard, Kaden R. A., *et al.*, 2014, “Many-Body Dynamics of Dipolar Molecules in an Optical Lattice,” *Phys. Rev. Lett.* **113**, 195302.
- Helgaker, T., P. Jørgensen, and J. Olsen, 2000, *Molecular Electronic Structure Theory* (John Wiley & Sons, New York).
- Hempel, Cornelius, *et al.*, 2018, “Quantum Chemistry Calculations on a Trapped-Ion Quantum Simulator,” *Phys. Rev. X* **8**, 031022.
- Heya, Kentaro, Ken M. Nakanishi, Kosuke Mitarai, and Keisuke Fujii, 2019, “Subspace variational quantum simulator,” *arXiv:1904.08566*.
- Heyl, M., A. Polkovnikov, and S. Kehrein, 2013, “Dynamical Quantum Phase Transitions in the Transverse-Field Ising Model,” *Phys. Rev. Lett.* **110**, 135704.

- Heyl, Markus, 2015, “Scaling and Universality at Dynamical Quantum Phase Transitions,” *Phys. Rev. Lett.* **115**, 140602.
- Heyl, Markus, 2018, “Dynamical quantum phase transitions: A review,” *Rep. Prog. Phys.* **81**, 054001.
- Heyl, Markus, Philipp Hauke, and Peter Zoller, 2019, “Quantum localization bounds Trotter errors in digital quantum simulation,” *Sci. Adv.* **5**, eaau8342.
- Ho, Wen Wei, and Timothy H. Hsieh, 2019, “Efficient variational simulation of non-trivial quantum states,” *SciPost Phys.* **6**, 29.
- Ho, Wen Wei, Cheryne Jonay, and Timothy H. Hsieh, 2019, “Ultrafast variational simulation of nontrivial quantum states with long-range interactions,” *Phys. Rev. A* **99**, 052332.
- Horodecki, Paweł, and Artur Ekert, 2002, “Method for Direct Detection of Quantum Entanglement,” *Phys. Rev. Lett.* **89**, 127902.
- Huang, Yi-Ping, Debasish Banerjee, and Markus Heyl, 2019, “Dynamical Quantum Phase Transitions in U(1) Quantum Link Models,” *Phys. Rev. Lett.* **122**, 250401.
- Huerta, Alderete, C., Shivani Singh, Nhung H. Nguyen, Daiwei Zhu, Radhakrishnan Balu, Christopher Monroe, C. M. Chandrashekar, and Norbert M. Linke, 2020, “Quantum walks and Dirac cellular automata on a programmable trapped-ion quantum computer,” *Nat. Commun.* **11**, 3720.
- Hume, D. B., T. Rosenband, and D. J. Wineland, 2007, “High-Fidelity Adaptive Qubit Detection through Repetitive Quantum Nondemolition Measurements,” *Phys. Rev. Lett.* **99**, 120502.
- Ip, Michael, Anthony Ransford, Andrew M. Jayich, Xueping Long, Conrad Roman, and Wesley C. Campbell, 2018, “Phonon Lasing from Optical Frequency Comb Illumination of Trapped Ions,” *Phys. Rev. Lett.* **121**, 043201.
- Islam, Kazi Rajibul, 2012, “Quantum simulation of interacting spin models with trapped ions,” Ph.D. thesis (University of Maryland).
- Islam, R., C. Senko, W. C. Campbell, S. Korenblit, J. Smith, A. Lee, E. E. Edwards, C.-C. J. Wang, J. K. Freericks, and C. Monroe, 2013, “Emergence and frustration of magnetism with variable-range interactions in a quantum simulator,” *Science* **340**, 583–587.
- Islam, R., *et al.*, 2011, “Onset of a quantum phase transition with a trapped ion quantum simulator,” *Nat. Commun.* **2**, 377.
- Itano, W. M., J. C. Bergquist, J. J. Bollinger, J. M. Gilligan, D. J. Heinzen, F. L. Moore, M. G. Raizen, and D. J. Wineland, 1993, “Quantum projection noise: Population fluctuations in two-level systems,” *Phys. Rev. A* **47**, 3554.
- James, D. F. V., 1998, “Quantum dynamics of cold trapped ions, with application to quantum computation,” *Appl. Phys. B* **66**, 181–190.
- Jensen, Frank, 1989, *An Introduction to Computational Chemistry* (John Wiley & Sons, New York).
- Johri, Sonika, Damian S. Steiger, and Matthias Troyer, 2017, “Entanglement spectroscopy on a quantum computer,” *Phys. Rev. B* **96**, 195136.
- Jones, Tyson, Suguru Endo, Sam McArdle, Xiao Yuan, and Simon C. Benjamin, 2019, “Variational quantum algorithms for discovering Hamiltonian spectra,” *Phys. Rev. A* **99**, 062304.
- Jordan, P., and E. P. Wigner, 1928, “About the Pauli exclusion principle,” *Z. Phys.* **47**, 631–651.
- Joshi, Manoj K., Andreas Elben, Benoît Vermersch, Tiff Brydges, Christine Maier, Peter Zoller, Rainer Blatt, and Christian F. Roos, 2020, “Quantum Information Scrambling in a Trapped-Ion Quantum Simulator with Tunable Range Interactions,” *Phys. Rev. Lett.* **124**, 240505.
- Jünemann, J., A. Cadarso, D. Pérez-García, A. Bermudez, and J. J. García-Ripoll, 2013, “Lieb-Robinson Bounds for Spin-Boson Lattice Models and Trapped Ions,” *Phys. Rev. Lett.* **111**, 230404.
- Jurcevic, P., B. P. Lanyon, P. Hauke, C. Hempel, P. Zoller, R. Blatt, and C. F. Roos, 2014, “Quasiparticle engineering and entanglement propagation in a quantum many-body system,” *Nature (London)* **511**, 202–205.
- Jurcevic, P., H. Shen, P. Hauke, C. Maier, T. Brydges, C. Hempel, B. P. Lanyon, M. Heyl, R. Blatt, and C. F. Roos, 2017, “Direct Observation of Dynamical Quantum Phase Transitions in an Interacting Many-Body System,” *Phys. Rev. Lett.* **119**, 080501.
- Kadowaki, Tadashi, and Hidetoshi Nishimori, 1998, “Quantum annealing in the transverse Ising model,” *Phys. Rev. E* **58**, 5355–5363.
- Kandala, Abhinav, Antonio Mezzacapo, Kristan Temme, Maika Takita, Markus Brink, Jerry M. Chow, and Jay M. Gambetta, 2017, “Hardware-efficient variational quantum eigensolver for small molecules and quantum magnets,” *Nature (London)* **549**, 242–246.
- Kastner, Michael, 2011, “Diverging Equilibration Times in Long-Range Quantum Spin Models,” *Phys. Rev. Lett.* **106**, 130601.
- Katayama, Kengo, and Hiroyuki Narihisa, 2001, “Performance of simulated annealing-based heuristic for the unconstrained binary quadratic programming problem,” *Eur. J. Oper. Res.* **134**, 103.
- Kendon, Vivien M., Kae Nemoto, and William J. Munro, 2010, “Quantum analogue computing,” *Phil. Trans. R. Soc. A* **368**, 3609.
- Kennedy, Tom, and Hal Tasaki, 1992, “Hidden  $Z_2 \times Z_2$  symmetry breaking in Haldane-gap antiferromagnets,” *Phys. Rev. B* **45**, 304.
- Khaneja, Navin, Timo Reiss, Cindie Kehlet, Thomas Schulte-Herbrüggen, and Steffen J. Glaser, 2005, “Optimal control of coupled spin dynamics: Design of NMR pulse sequences by gradient ascent algorithms,” *J. Magn. Reson.* **172**, 296.
- Khemani, Vedika, Achilleas Lazarides, Roderich Moessner, and Shivaji L. Sondhi, 2016, “Phase Structure of Driven Quantum Systems,” *Phys. Rev. Lett.* **116**, 250401.
- Khromova, A., Ch. Piltz, B. Scharfenberger, T. F. Gloger, M. Johanning, A. F. Varón, and Ch. Wunderlich, 2012, “Designer Spin Pseudomolecule Implemented with Trapped Ions in a Magnetic Gradient,” *Phys. Rev. Lett.* **108**, 220502.
- Kielpinski, D., C. Monroe, and D. J. Wineland, 2002, “Architecture for a large-scale ion-trap quantum computer,” *Nature (London)* **417**, 709–711.
- Kienzler, D., H.-Y. Lo, V. Negnevitsky, C. Flühmann, M. Marinelli, and J. P. Home, 2017, “Quantum Harmonic Oscillator State Control in a Squeezed Fock Basis,” *Phys. Rev. Lett.* **119**, 033602.
- Kim, K., M.-S. Chang, R. Islam, S. Korenblit, L.-M. Duan, and C. Monroe, 2009, “Entanglement and Tunable Spin-Spin Couplings between Trapped Ions Using Multiple Transverse Modes,” *Phys. Rev. Lett.* **103**, 120502.
- Kim, K., *et al.*, 2011, “Quantum simulation of the transverse Ising model with trapped ions,” *New J. Phys.* **13**, 105003.
- Kim, Kihwan, Ming-Shien Chang, Simcha Korenblit, Rajibul Islam, Emily E. Edwards, James K. Freericks, Guin-Dar Lin, Lu-Ming Duan, and Christopher Monroe, 2010, “Quantum simulation of frustrated Ising spins with trapped ions,” *Nature (London)* **465**, 590.
- Kinoshita, Toshiya, Trevor Wenger, and David S. Weiss, 2006, “A quantum Newton’s cradle,” *Nature (London)* **440**, 900–903.
- Kitaev, Alexei, 2006, “Anyons in an exactly solved model and beyond,” *Ann. Phys. (Amsterdam)* **321**, 2–111.
- Kitagawa, Takuya, Erez Berg, Mark Rudner, and Eugene Demler, 2010, “Topological characterization of periodically driven quantum systems,” *Phys. Rev. B* **82**, 235114.
- Kloss, Benedikt, and Yevgeny Bar Lev, 2019, “Spin transport in a long-range-interacting spin chain,” *Phys. Rev. A* **99**, 032114.
- Knap, Michael, Adrian Kantian, Thierry Giamarchi, Immanuel Bloch, Mikhail D. Lukin, and Eugene Demler, 2013, “Probing

- Real-Space and Time-Resolved Correlation Functions with Many-Body Ramsey Interferometry,” *Phys. Rev. Lett.* **111**, 147205.
- Kohlert, Thomas, Sebastian Scherg, Xiao Li, Henrik P. Lüschen, Sankar Das Sarma, Immanuel Bloch, and Monika Aidelsburger, 2019, “Observation of Many-Body Localization in a One-Dimensional System with a Single-Particle Mobility Edge,” *Phys. Rev. Lett.* **122**, 170403.
- Kohn, W., 1999, “Nobel Lecture: Electronic structure of matter-wave functions and density functionals,” *Rev. Mod. Phys.* **71**, 1253–1266.
- Kokail, C., *et al.*, 2019, “Self-verifying variational quantum simulation of lattice models,” *Nature (London)* **569**, 355–360.
- Kolsgaard, M. L., G. Joner, C. Brunborg, S. A. Anderssen, S. Tonstad, and L. F. Andersen, 2001, “A quantum adiabatic evolution algorithm applied to random instances of an NP-complete problem,” *Science* **292**, 472–476.
- Kondov, S. S., W. R. McGehee, W. Xu, and B. DeMarco, 2015, “Disorder-Induced Localization in a Strongly Correlated Atomic Hubbard Gas,” *Phys. Rev. Lett.* **114**, 083002.
- König, S., S. K. Bogner, R. J. Furnstahl, S. N. More, and T. Papenbrock, 2014, “Ultraviolet extrapolations in finite oscillator bases,” *Phys. Rev. C* **90**, 064007.
- Korenblit, S., *et al.*, 2012, “Quantum simulation of spin models on an arbitrary lattice with trapped ions,” *New J. Phys.* **14**, 095024.
- Krotov, V. F., 1996, *Global Methods in Optimal Control Theory* (Dekker, New York).
- Kumph, M., P. Holz, K. Langer, M. Meraner, M. Niedermayr, M. Brownnutt, and R. Blatt, 2016, “Operation of a planar-electrode ion-trap array with adjustable RF electrodes,” *New J. Phys.* **18**, 023047.
- Kuwahara, Tomotaka, Takashi Mori, and Keiji Saito, 2016, “Floquet-Magnus theory and generic transient dynamics in periodically driven many-body quantum systems,” *Ann. Phys. (Amsterdam)* **367**, 96–124.
- Kuwahara, Tomotaka, and Keiji Saito, 2020, “Strictly Linear Light Cones in Long-Range Interacting Systems of Arbitrary Dimensions,” *Phys. Rev. X* **10**, 031010.
- Ladd, T. D., F. Jelezko, R. Laflamme, Y. Nakamura, C. Monroe, and J. L. O’Brien, 2010, “Quantum computers,” *Nature (London)* **464**, 45.
- Lanczos, C., 1950, “An iteration method for the solution of the eigenvalue problem of linear differential and integral operators,” *J. Res. Natl. Bur. Stand.* **45**, 255.
- Landsman, Kevin A., Caroline Figgatt, Thomas Schuster, Norbert M. Linke, Beni Yoshida, Norman Y. Yao, and Christopher Monroe, 2019, “Verified quantum information scrambling,” *Nature (London)* **567**, 61.
- Langen, Tim, Sebastian Erne, Remi Geiger, Bernhard Rauer, Thomas Schweigler, Maximilian Kuhnert, Wolfgang Rohringer, Igor E. Mazets, Thomas Gasenzer, and Jörg Schmiedmayer, 2015, “Experimental observation of a generalized Gibbs ensemble,” *Science* **348**, 207–211.
- Lanyon, Ben P., *et al.*, 2011, “Universal digital quantum simulation with trapped ions,” *Science* **334**, 57–61.
- Larkin, A. I., and Yu. N. Ovchinnikov, 1969, “Quasiclassical method in the theory of superconductivity,” *Sov. Phys. JETP* **28**, 1200–1205.
- Larson, D. J., J. C. Bergquist, J. J. Bollinger, Wayne M. Itano, and D. J. Wineland, 1986, “Sympathetic Cooling of Trapped Ions: A Laser-Cooled Two-Species Nonneutral Ion Plasma,” *Phys. Rev. Lett.* **57**, 70–73.
- Lashkari, Nima, Douglas Stanford, Matthew Hastings, Tobias Osborne, and Patrick Hayden, 2013, “Towards the fast scrambling conjecture,” *J. High Energy Phys.* **04**, 022.
- Lee, A. C., J. Smith, P. Richerme, B. Neyenhuis, P. W. Hess, J. Zhang, and C. Monroe, 2016, “Engineering large Stark shifts for control of individual clock state qubits,” *Phys. Rev. A* **94**, 042308.
- Lee, P. J., K.-A. Brickman, L. Deslauriers, P. C. Haljan, L.-M. Duan, and C. Monroe, 2005, “Phase control of trapped ion quantum gates,” *J. Opt. B* **7**, S371.
- Lee, Patrick A., Naoto Nagaosa, and Xiao-Gang Wen, 2006, “Doping a Mott insulator: Physics of high-temperature superconductivity,” *Rev. Mod. Phys.* **78**, 17.
- Leibfried, D., R. Blatt, C. Monroe, and D. Wineland, 2003, “Quantum dynamics of single trapped ions,” *Rev. Mod. Phys.* **75**, 281–324.
- Leibfried, D., *et al.*, 2002, “Trapped-Ion Quantum Simulator: Experimental Application to Nonlinear Interferometers,” *Phys. Rev. Lett.* **89**, 247901.
- Leibfried, Dietrich, 2010, “Could a boom in technologies trap Feynman’s simulator?,” *Nature (London)* **463**, 608.
- Lepori, L., A. Trombettoni, and D. Vodola, 2017, “Singular dynamics and emergence of nonlocality in long-range quantum models,” *J. Stat. Mech.* **033102**.
- Li, Jun, Ruihua Fan, Hengyan Wang, Bingtian Ye, Bei Zeng, Hui Zhai, Xinhua Peng, and Jiangfeng Du, 2017, “Measuring Out-of-Time-Order Correlators on a Nuclear Magnetic Resonance Quantum Simulator,” *Phys. Rev. X* **7**, 031011.
- Li, Ying, and Simon C. Benjamin, 2012, “High threshold distributed quantum computing with three-qubit nodes,” *New J. Phys.* **14**, 093008.
- Li, Ying, and Simon C. Benjamin, 2017, “Efficient Variational Quantum Simulator Incorporating Active Error Minimization,” *Phys. Rev. X* **7**, 021050.
- Lieb, Elliott H., and Derek W. Robinson, 1972, “The finite group velocity of quantum spin systems,” *Commun. Math. Phys.* **28**, 251.
- Liebsch, Ansgar, and Hiroshi Ishida, 2012, “Temperature and bath size in exact diagonalization dynamical mean field theory,” *J. Phys. Condens. Matter* **24**, 053201.
- Lienhard, Vincent, Sylvain de Léséleuc, Daniel Barredo, Thierry Lahaye, Antoine Browaeys, Michael Schuler, Louis-Paul Henry, and Andreas M. Läuchli, 2018, “Observing the Space- and Time-Dependent Growth of Correlations in Dynamically Tuned Synthetic Ising Models with Antiferromagnetic Interactions,” *Phys. Rev. X* **8**, 021070.
- Lin, G.-D., C. Monroe, and L.-M. Duan, 2011, “Sharp Phase Transitions in a Small Frustrated Network of Trapped Ion Spins,” *Phys. Rev. Lett.* **106**, 230402.
- Lin, G.-D., S.-L. Zhu, R. Islam, K. Kim, M.-S. Chang, S. Korenblit, C. Monroe, and L.-M. Duan, 2009, “Large-scale quantum computation in an anharmonic linear ion trap,” *Europhys. Lett.* **86**, 60004.
- Lin, Yiheng, J. P. Gaebler, Florentin Reiter, Ting Rei Tan, Ryan Bowler, A. S. Sørensen, Dietrich Leibfried, and David J. Wineland, 2013, “Dissipative production of a maximally entangled steady state of two quantum bits,” *Nature (London)* **504**, 415.
- Lindner, Netanel H., Gil Refael, and Victor Galitski, 2011, “Floquet topological insulator in semiconductor quantum wells,” *Nat. Phys.* **7**, 490.
- Linke, N. M., S. Johri, C. Figgatt, K. A. Landsman, A. Y. Matsuura, and C. Monroe, 2018, “Measuring the Rényi entropy of a two-site Fermi-Hubbard model on a trapped ion quantum computer,” *Phys. Rev. A* **98**, 052334.
- Liu, Haitao, Shengli Xu, Xiaofang Wang, Junnan Wu, and Yang Song, 2015, “A global optimization algorithm for simulation-based problems via the extended direct scheme,” *Eng. Optim.* **47**, 1441–1458.

- Lloyd, Seth, 1996, “Universal quantum simulators,” *Science* **273**, 1073.
- Lloyd, Seth, 2008, “Quantum information matters,” *Science* **319**, 1209–1211.
- Lu, Hsuan-Hao, *et al.*, 2019, “Simulations of subatomic many-body physics on a quantum frequency processor,” *Phys. Rev. A* **100**, 012320.
- Luitz, David J., Nicolas Laflorencie, and Fabien Alet, 2015, “Many-body localization edge in the random-field Heisenberg chain,” *Phys. Rev. B* **91**, 081103.
- Luitz, David J., and Yevgeny Bar Lev, 2019, “Emergent locality in systems with power-law interactions,” *Phys. Rev. A* **99**, 010105.
- Lukin, Alexander, Matthew Rispoli, Robert Schittko, M. Eric Tai, Adam M. Kaufman, Soonwon Choi, Vedika Khemani, Julian Léonard, and Markus Greiner, 2019, “Probing entanglement in a many-body-localized system,” *Science* **364**, 256–260.
- Lüschen, Henrik P., Pranjal Bordia, Sean S. Hodgman, Michael Schreiber, Saubhik Sarkar, Andrew J. Daley, Mark H. Fischer, Ehud Altman, Immanuel Bloch, and Ulrich Schneider, 2017, “Signatures of Many-Body Localization in a Controlled Open Quantum System,” *Phys. Rev. X* **7**, 011034.
- Lüschen, Henrik P., Pranjal Bordia, Sebastian Scherg, Fabien Alet, Ehud Altman, Ulrich Schneider, and Immanuel Bloch, 2017, “Observation of Slow Dynamics near the Many-Body Localization Transition in One-Dimensional Quasiperiodic Systems,” *Phys. Rev. Lett.* **119**, 260401.
- Lv, Dingshun, Shuoming An, Zhenyu Liu, Jing-Ning Zhang, Julen S. Pedernales, Lucas Lamata, Enrique Solano, and Kihwan Kim, 2018, “Quantum Simulation of the Quantum Rabi Model in a Trapped Ion,” *Phys. Rev. X* **8**, 021027.
- Machado, Francisco, Dominic V. Else, Gregory D. Kahanamoku-Meyer, Chetan Nayak, and Norman Y. Yao, 2020, “Long-Range Prethermal Phases of Nonequilibrium Matter,” *Phys. Rev. X* **10**, 011043.
- Machado, Francisco, Gregory D. Kahanamoku-Meyer, Dominic V. Else, Chetan Nayak, and Norman Y. Yao, 2019, “Exponentially slow heating in short and long-range interacting Floquet systems,” *Phys. Rev. Research* **1**, 033202.
- Maghrebi, Mohammad F., Zhe-Xuan Gong, Michael Foss-Feig, and Alexey V. Gorshkov, 2016, “Causality and quantum criticality in long-range lattice models,” *Phys. Rev. B* **93**, 125128.
- Mahadev, Urmila, 2018, “Classical verification of quantum computations,” in *Proceedings of the 59th Annual IEEE Symposium on Foundations of Computer Science (FOCS 2018), Paris, 2018* (IEEE, New York), pp. 259–267.
- Maier, Christine, Tiff Brydges, Petar Jurcevic, Nils Trautmann, Cornelius Hempel, Ben P. Lanyon, Philipp Hauke, Rainer Blatt, and Christian F. Roos, 2019, “Environment-Assisted Quantum Transport in a 10-Qubit Network,” *Phys. Rev. Lett.* **122**.
- Maksymov, Andrii O., Noah Rahman, Eliot Kapit, and Alexander L. Burin, 2017, “Comment on ‘Many-body localization in Ising models with random long-range interactions,’” *Phys. Rev. A* **96**, 057601.
- Maldacena, Juan, and Xiao-Liang Qi, 2018, “Eternal traversable wormhole,” [arXiv:1804.00491](https://arxiv.org/abs/1804.00491).
- Maldacena, Juan, Stephen H. Shenker, and Douglas Stanford, 2016, “A bound on chaos,” *J. High Energy Phys.* **08**, 106.
- Maldacena, Juan, Douglas Stanford, and Zhenbin Yang, 2017, “Diving into traversable wormholes,” *Fortschr. Phys.* **65**, 1700034.
- Mallick, Arindam, Sanjoy Mandal, Anirban Karan, and C. M. Chandrashekar, 2019, “Simulating Dirac Hamiltonian in curved space-time by split-step quantum walk,” *J. Phys. Commun.* **3**, 015012.
- Manmana, S. R., S. Wessel, R. M. Noack, and A. Muramatsu, 2007, “Strongly Correlated Fermions after a Quantum Quench,” *Phys. Rev. Lett.* **98**, 210405.
- Marquet, C., F. Schmidt-Kaler, and D. F. V. James, 2003, “Phonon-phonon interactions due to non-linear effects in a linear ion trap,” *Appl. Phys. B* **76**, 199–208.
- Martinez, Esteban A., *et al.*, 2016, “Real-time dynamics of lattice gauge theories with a few-qubit quantum computer,” *Nature (London)* **534**, 516–519.
- Martyn, John, and Brian Swingle, 2019, “Product spectrum ansatz and the simplicity of thermal states,” *Phys. Rev. A* **100**, 032107.
- Maslennikov, G., S. Ding, R. Hablützel, J. Gan, A. Roulet, S. Nimmrichter, J. Dai, V. Scarani, and D. Matsukevich, 2019, “Quantum absorption refrigerator with trapped ions,” *Nat. Commun.* **10**, 202.
- Matsuta, T., T. Koma, and S. Nakamura, 2017, “Improving the Lieb-Robinson bound for long-range interactions,” *Ann. Henri Poincaré* **18**, 519–528.
- McArdle, Sam, Tyson Jones, Suguru Endo, Ying Li, Simon C. Benjamin, and Xiao Yuan, 2019, “Variational ansatz-based quantum simulation of imaginary time evolution,” *npj Quantum Inf.* **5**, 75.
- McArdle, Sam, Xiao Yuan, and Simon Benjamin, 2019, “Error-Mitigated Digital Quantum Simulation,” *Phys. Rev. Lett.* **122**, 180501.
- McClean, Jarrod R., Sergio Boixo, Vadim N. Smelyanskiy, Ryan Babbush, and Hartmut Neven, 2018, “Barren plateaus in quantum neural network training landscapes,” *Nat. Commun.* **9**, 4812.
- McClean, Jarrod R., Jonathan Romero, Ryan Babbush, and Alán Aspuru-Guzik, 2016, “The theory of variational hybrid quantum-classical algorithms,” *New J. Phys.* **18**, 023023.
- Messiah, Albert, 1962, *Quantum Mechanics* (North-Holland, Amsterdam).
- Milburn, G. J., S. Schneider, and D. F. V. James, 2000, “Ion trap quantum computing with warm ions,” *Fortschr. Phys.* **48**, 801–810.
- Moessner, R., and A. P. Ramirez, 2006, “Geometrical frustration,” *Phys. Today* **59**, No. 2, 24–29.
- Moessner, Roderich, and Shivaji Lal Sondhi, 2017, “Equilibration and order in quantum Floquet matter,” *Nat. Phys.* **13**, 424.
- Mølmer, Klaus, and Anders Sørensen, 1999, “Multiparticle Entanglement of Hot Trapped Ions,” *Phys. Rev. Lett.* **82**, 1835.
- Monroe, C., and J. Kim, 2013, “Scaling the ion trap quantum processor,” *Science* **339**, 1164.
- Monroe, C., R. Raussendorf, A. Ruthven, K. R. Brown, P. Maunz, L.-M. Duan, and J. Kim, 2014, “Large-scale modular quantum-computer architecture with atomic memory and photonic interconnects,” *Phys. Rev. A* **89**, 022317.
- Mori, Takashi, Tomotaka Kuwahara, and Keiji Saito, 2016, “Rigorous Bound on Energy Absorption and Generic Relaxation in Periodically Driven Quantum Systems,” *Phys. Rev. Lett.* **116**, 120401.
- Morita, Satoshi, and Hidetoshi Nishimori, 2008, “Mathematical foundation of quantum annealing,” *J. Math. Phys. (N.Y.)* **49**, 125210.
- Müller, M., K. Hammerer, Y. L. Zhou, C. F. Roos, and P. Zoller, 2011, “Simulating open quantum systems: From many-body interactions to stabilizer pumping,” *New J. Phys.* **13**, 085007.
- Muschik, C., M. Heyl, E. Martinez, T. Monz, P. Schindler, B. Vogell, M. Dalmonte, P. Hauke, R. Blatt, and P. Zoller, 2017, “U(1) Wilson lattice gauge theories in digital quantum simulators,” *New J. Phys.* **19**, 103020.
- Myerson, A. H., D. J. Szwer, S. C. Webster, D. T. C. Allcock, M. J. Curtis, G. Imreh, J. A. Sherman, D. N. Stacey, A. M. Steane, and

- D. M. Lucas, 2008, “High-Fidelity Readout of Trapped-Ion Qubits,” *Phys. Rev. Lett.* **100**, 200502.
- Nagourney, Warren, Jon Sandberg, and Hans Dehmelt, 1986, “Shelved Optical Electron Amplifier: Observation of Quantum Jumps,” *Phys. Rev. Lett.* **56**, 2797–2799.
- Nam, Yunseong, *et al.*, 2020, “Ground-state energy estimation of the water molecule on a trapped-ion quantum computer,” *npj Quantum Inf.* **6**, 33.
- Nandkishore, Rahul, and David A. Huse, 2015, “Many-body localization and thermalization in quantum statistical mechanics,” *Annu. Rev. Condens. Matter Phys.* **6**, 15–38.
- Nandkishore, Rahul M., and Shivaji Lal Sondhi, 2017, “Many-Body Localization with Long-Range Interactions,” *Phys. Rev. X* **7**, 041021.
- Nevado, Pedro, and Diego Porras, 2016, “Hidden frustrated interactions and quantum annealing in trapped-ion spin-phonon chains,” *Phys. Rev. A* **93**, 013625.
- Neyenhuis, Brian, Jiehang Zhang, Paul W. Hess, Jacob Smith, Aaron C. Lee, Phil Richerme, Zhe-Xuan Gong, Alexey V. Gorshkov, and Christopher Monroe, 2017, “Observation of prethermalization in long-range interacting spin chains,” *Sci. Adv.* **3**, e1700672.
- Nezhadhighi, M. Ghasemi, and M. A. Rajabpour, 2014, “Entanglement dynamics in short- and long-range harmonic oscillators,” *Phys. Rev. B* **90**, 205438.
- Nielsen, M. A., and I. L. Chuang, 2000, *Quantum Computation and Quantum Information* (Cambridge University Press, Cambridge, England).
- Noek, Rachel, Geert Vrijsen, Daniel Gaultney, Emily Mount, Taehyun Kim, Peter Maunz, and Jungsang Kim, 2013, “High speed, high fidelity detection of an atomic hyperfine qubit,” *Opt. Lett.* **38**, 4735–4738.
- Oganesyan, Vadim, and David A. Huse, 2007, “Localization of interacting fermions at high temperature,” *Phys. Rev. B* **75**, 155111.
- Ohira, Ryutaro, Shota Kume, Kyoichi Takayama, Silpa Muralidharan, Hiroki Takahashi, and Kenji Toyoda, 2020, “Confinement and retrieval of local phonons in a trapped-ion chain,” [arXiv:2003.03962](https://arxiv.org/abs/2003.03962).
- Oka, Takashi, and Sota Kitamura, 2019, “Floquet engineering of quantum materials,” *Annu. Rev. Condens. Matter Phys.* **10**, 387–408.
- Olmschenk, S., K. C. Younge, D. L. Moehring, D. N. Matsukevich, P. Maunz, and C. Monroe, 2007, “Manipulation and detection of a trapped Yb<sup>+</sup> hyperfine qubit,” *Phys. Rev. A* **76**, 052314.
- O’Malley, P. J. J., *et al.*, 2016, “Scalable Quantum Simulation of Molecular Energies,” *Phys. Rev. X* **6**, 031007.
- Otterbach, J. S., *et al.*, 2017, “Unsupervised machine learning on a hybrid quantum computer,” [arXiv:1712.05771](https://arxiv.org/abs/1712.05771).
- Ozeri, R., *et al.*, 2007, “Errors in trapped-ion quantum gates due to spontaneous photon scattering,” *Phys. Rev. A* **75**, 042329.
- Pagano, G., *et al.*, 2018, “Cryogenic trapped-ion system for large scale quantum simulation,” *Quantum Sci. Technol.* **4**, 014004.
- Pagano, G., *et al.*, 2020, “Quantum approximate optimization of the long-range Ising model with a trapped-ion quantum simulator,” *Proc. Natl. Acad. Sci. U.S.A.* **117**, 25396.
- Peruzzo, Alberto, Jarrod McClean, Peter Shadbolt, Man-Hong Yung, Xiao-Qi Zhou, Peter J. Love, Alán Aspuru-Guzik, and Jeremy L. O’Brien, 2014, “A variational eigenvalue solver on a photonic quantum processor,” *Nat. Commun.* **5**, 4213.
- Piltz, Christian, Theeraphot Sriarunothai, Svetoslav S. Ivanov, Sabine Wölk, and Christof Wunderlich, 2016, “Versatile microwave-driven trapped ion spin system for quantum information processing,” *Sci. Adv.* **2**, e1600093.
- Pino, J. M., *et al.*, 2020, [arXiv:2003.01293](https://arxiv.org/abs/2003.01293).
- Pino, M., 2014, “Entanglement growth in many-body localized systems with long-range interactions,” *Phys. Rev. B* **90**, 174204.
- Poitzsch, M. E., J. C. Bergquist, W. M. Itano, and D. J. Wineland, 1996, “Cryogenic linear ion trap for accurate spectroscopy,” *Rev. Sci. Instrum.* **67**, 129–134.
- Polkovnikov, Anatoli, Krishnendu Sengupta, Alessandro Silva, and Mukund Vengalattore, 2011, “Colloquium: Nonequilibrium dynamics of closed interacting quantum systems,” *Rev. Mod. Phys.* **83**, 863.
- Pollmann, Frank, Ari M. Turner, Erez Berg, and Masaki Oshikawa, 2010, “Entanglement spectrum of a topological phase in one dimension,” *Phys. Rev. B* **81**, 064439.
- Ponte, Pedro, Anushya Chandran, Z. Papić, and Dmitry A. Abanin, 2015, “Periodically driven ergodic and many-body localized quantum systems,” *Ann. Phys. (Amsterdam)* **353**, 196–204.
- Ponte, Pedro, Z. Papić, François Huveneers, and Dmitry A. Abanin, 2015, “Many-Body Localization in Periodically Driven Systems,” *Phys. Rev. Lett.* **114**, 140401.
- Porras, Diego, and J. Ignacio Cirac, 2004, “Effective Quantum Spin Systems with Trapped Ions,” *Phys. Rev. Lett.* **92**, 207901.
- Potirniche, I.-D., Andrew C. Potter, Monika Schleier-Smith, Ashvin Vishwanath, and Norman Y. Yao, 2017, “Floquet Symmetry-Protected Topological Phases in Cold-Atom Systems,” *Phys. Rev. Lett.* **119**, 123601.
- Poulin, David, Angie Qarry, Rolando Somma, and Frank Verstraete, 2011, “Quantum Simulation of Time-Dependent Hamiltonians and the Convenient Illusion of Hilbert Space,” *Phys. Rev. Lett.* **106**, 170501.
- Preskill, John, 1998, “Reliable quantum computers,” *Proc. R. Soc. A* **454**, 385.
- Preskill, John, 2018, “Quantum Computing in the NISQ era and beyond,” *Quantum* **2**, 79.
- Qiang, Xiaogang, *et al.*, 2018, “Large-scale silicon quantum photonics implementing arbitrary two-qubit processing,” *Nat. Photonics* **12**, 534–539.
- Quan, H. T., and W. H. Zurek, 2010, “Testing quantum adiabaticity with quench echo,” *New J. Phys.* **12**, 093025.
- Raimond, J. M., M. Brune, and S. Haroche, 2001, “Manipulating quantum entanglement with atoms and photons in a cavity,” *Rev. Mod. Phys.* **73**, 565–582.
- Raizen, M. G., J. M. Gilligan, J. C. Bergquist, W. M. Itano, and D. J. Wineland, 1992, “Linear trap for high-accuracy spectroscopy of stored ions,” *J. Mod. Opt.* **39**, 233–242.
- Rajabi, Fereshteh, Sainath Motlakunta, Chung-You Shih, Nikhil Kotibhaskar, Qudsia Quraishi, Ashok Ajoy, and Rajibul Islam, 2019, “Dynamical Hamiltonian engineering of 2D rectangular lattices in a one-dimensional ion chain,” *npj Quantum Inf.* **5**, 32.
- Rajabpour, M. A., and S. Sotiriadis, 2015, “Quantum quench in long-range field theories,” *Phys. Rev. B* **91**, 045131.
- Rebentrost, Patrick, Masoud Mohseni, Ivan Kassal, Seth Lloyd, and Alán Aspuru-Guzik, 2009, “Environment-assisted quantum transport,” *New J. Phys.* **11**, 033003.
- Rechtsman, Mikael C., Julia M. Zeuner, Yonatan Plotnik, Yaakov Lumer, Daniel Podolsky, Felix Dreisow, Stefan Nolte, Mordechai Segev, and Alexander Szameit, 2013, “Photonic Floquet topological insulators,” *Nature (London)* **496**, 196.
- Richerme, Philip, Zhe-Xuan Gong, Aaron Lee, Crystal Senko, Jacob Smith, Michael Foss-Feig, Spyridon Michalakis, Alexey V. Gorshkov, and Christopher Monroe, 2014, “Non-local propagation of correlations in quantum systems with long-range interactions,” *Nature (London)* **511**, 198–201.
- Richerme, Philip, Crystal Senko, Simcha Korenblit, Jacob Smith, Aaron Lee, Rajibul Islam, Wesley C. Campbell, and Christopher Monroe, 2013, “Quantum Catalysis of Magnetic Phase Transitions in a Quantum Simulator,” *Phys. Rev. Lett.* **111**, 100506.

- Richerme, Philip, Crystal Senko, Jacob Smith, Aaron Lee, and Christopher Monroe, 2013, “Experimental performance of a quantum simulator: Optimizing adiabatic evolution and identifying many-body ground states,” *Phys. Rev. A* **88**, 012334.
- Rigol, Marcos, Vanja Dunjko, and Maxim Olshanii, 2008, “Thermalization and its mechanism for generic isolated quantum systems,” *Nature (London)* **452**, 854–858.
- Rigol, Marcos, Vanja Dunjko, Vladimir Yurovsky, and Maxim Olshanii, 2007, “Relaxation in a Completely Integrable Many-Body Quantum System: An *Ab Initio* Study of the Dynamics of the Highly Excited States of 1D Lattice Hard-Core Bosons,” *Phys. Rev. Lett.* **98**, 050405.
- Roland, Jeremie, and Nicolas J. Cerf, 2002, “Quantum search by local adiabatic evolution,” *Phys. Rev. A* **65**, 042308.
- Romero, Jonathan, Ryan Babbush, Jarrod R. McClean, Cornelius Hempel, Peter J. Love, and Alán Aspuru-Guzik, 2018, “Strategies for quantum computing molecular energies using the unitary coupled cluster ansatz,” *Quantum Sci. Technol.* **4**, 014008.
- Roos, B. O., P. R. Taylor, and Per E. M. Sigbahn, 1980, “A complete active space SCF method (CASSCF) using a density matrix formulated super-CI approach,” *Chem. Phys. Lett.* **48**, 157–173.
- Roßnagel, Johannes, Samuel T. Dawkins, Karl N. Tolazzi, Obinna Abah, Eric Lutz, Ferdinand Schmidt-Kaler, and Kilian Singer, 2016, “A single-atom heat engine,” *Science* **352**, 325–329.
- Roushan, P., *et al.*, 2017, “Spectroscopic signatures of localization with interacting photons in superconducting qubits,” *Science* **358**, 1175–1179.
- Rovny, Jared, Robert L. Blum, and Sean E. Barrett, 2018, “Observation of Discrete-Time-Crystal Signatures in an Ordered Dipolar Many-Body System,” *Phys. Rev. Lett.* **120**, 180603.
- Rungger, I., *et al.*, 2019, “Dynamical mean field theory algorithm and experiment on quantum computers,” [arXiv:1910.04735](https://arxiv.org/abs/1910.04735).
- Ruster, T., C. T. Schmiegelow, H. Kaufmann, C. Warschburger, F. Schmidt-Kaler, and U. G. Poschinger, 2016, “A long-lived Zeeman trapped-ion qubit,” *Appl. Phys. B* **122**, 254.
- Sachdev, Subir, 2011, *Quantum Phase Transitions* (Cambridge University Press, Cambridge, England).
- Sackett, C. A., D. Kielpinski, B. E. King, C. Langer, V. Meyer, C. J. Myatt, M. Rowe, Q. A. Turchette, W. M. Itano, and D. J. Wineland, 2000, “Experimental entanglement of four particles,” *Nature (London)* **404**, 256–259.
- Safavi-Naini, A., R. J. Lewis-Swan, J. G. Bohnet, M. Gärtner, K. A. Gilmore, J. E. Jordan, J. Cohn, J. K. Freericks, A. M. Rey, and J. J. Bollinger, 2018, “Verification of a Many-Ion Simulator of the Dicke Model Through Slow Quenches across a Phase Transition,” *Phys. Rev. Lett.* **121**, 040503.
- Salathé, Y., *et al.*, 2015, “Digital Quantum Simulation of Spin Models with Circuit Quantum Electrodynamics,” *Phys. Rev. X* **5**, 021027.
- Sandvik, A. W., 2010, “Ground States of a Frustrated Quantum Spin Chain with Long-Range Interactions,” *Phys. Rev. Lett.* **104**, 137204.
- Sauter, Th., W. Neuhauser, R. Blatt, and P. E. Toschek, 1986, “Observation of Quantum Jumps,” *Phys. Rev. Lett.* **57**, 1696–1698.
- Sawyer, Brian C., Joseph W. Britton, Adam C. Keith, C.-C. Joseph Wang, James K. Freericks, Hermann Uys, Michael J. Biercuk, and John J. Bollinger, 2012, “Spectroscopy and Thermometry of Drumhead Modes in a Mesoscopic Trapped-Ion Crystal Using Entanglement,” *Phys. Rev. Lett.* **108**, 213003.
- Schachenmayer, J., B. P. Lanyon, C. F. Roos, and A. J. Daley, 2013, “Entanglement Growth in Quench Dynamics with Variable Range Interactions,” *Phys. Rev. X* **3**, 031015.
- Schmitz, H., R. Matjeschk, Ch. Schneider, J. Glueckert, M. Enderlein, T. Huber, and T. Schaetz, 2009, “Quantum Walk of a Trapped Ion in Phase Space,” *Phys. Rev. Lett.* **103**, 090504.
- Schneider, Ch., Diego Porras, and Tobias Schaetz, 2012, “Experimental quantum simulations of many-body physics with trapped ions,” *Rep. Prog. Phys.* **75**, 024401.
- Schollwöck, U., 2005, “The density-matrix renormalization group,” *Rev. Mod. Phys.* **77**, 259–315.
- Schreiber, Michael, Sean S. Hodgman, Pranjal Bordia, Henrik P. Lüschen, Mark H. Fischer, Ronen Vosk, Ehud Altman, Ulrich Schneider, and Immanuel Bloch, 2015, “Observation of many-body localization of interacting fermions in a quasirandom optical lattice,” *Science* **349**, 842–845.
- Senko, C., P. Richerme, J. Smith, A. Lee, I. Cohen, A. Retzker, and C. Monroe, 2015, “Realization of a Quantum Integer-Spin Chain with Controllable Interactions,” *Phys. Rev. X* **5**, 021026.
- Senko, C., J. Smith, P. Richerme, A. Lee, W. C. Campbell, and C. Monroe, 2014, “Coherent imaging spectroscopy of a quantum many-body spin system,” *Science* **345**, 430–433.
- Serbyn, M., Michael Knap, Sarang Gopalakrishnan, Z. Papić, Norman Ying Yao, C. R. Laumann, D. A. Abanin, Mikhail D. Lukin, and Eugene A. Demler, 2014, “Interferometric Probes of Many-Body Localization,” *Phys. Rev. Lett.* **113**, 147204.
- Shavitt, Isaiah, 1984, “The treatment of electron correlation: Where do we go from here?,” in *Advanced Theories and Computational Approaches to the Electronic Structure of Molecules*, edited by Clifford E. Dykstra (Springer Netherlands, Dordrecht), pp. 185–196.
- Shehab, O., I. H. Kim, N. H. Nguyen, K. A. Landsman, C. Huerta Alderete, D. Zhu, C. Monroe, and N. M. Linke, 2019, “Noise reduction using past causal cones in variational quantum algorithms,” [arXiv:1906.00476](https://arxiv.org/abs/1906.00476).
- Shehab, O., K. Landsman, Y. Nam, D. Zhu, N. M. Linke, M. Keesan, R. C. Pooser, and C. Monroe, 2019, “Toward convergence of effective-field-theory simulations on digital quantum computers,” *Phys. Rev. A* **100**, 062319.
- Shen, C., Z. Zhang, and L.-M. Duan, 2014, “Scalable Implementation of Boson Sampling with Trapped Ions,” *Phys. Rev. Lett.* **112**, 050504.
- Shen, Chao, and L.-M. Duan, 2012, “Correcting detection errors in quantum state engineering through data processing,” *New J. Phys.* **14**, 053053.
- Shen, Yangchao, Yao Lu, Kuan Zhang, Junhua Zhang, Shuaining Zhang, Joonsuk Huh, and Kihwan Kim, 2018, “Quantum optical emulation of molecular vibronic spectroscopy using a trapped-ion device,” *Chem. Sci.* **9**, 836–840.
- Shen, Yangchao, Xiang Zhang, Shuaining Zhang, Jing-Ning Zhang, Man-Hong Yung, and Kihwan Kim, 2017, “Quantum implementation of the unitary coupled cluster for simulating molecular electronic structure,” *Phys. Rev. A* **95**, 020501.
- Shi, Tao, Eugene Demler, and J. Ignacio Cirac, 2018, “Variational study of fermionic and bosonic systems with non-Gaussian states: Theory and applications,” *Ann. Phys. (Amsterdam)* **390**, 245–302.
- Sieberer, Lukas M., Tobias Olsacher, Andreas Elben, Markus Heyl, Philipp Hauke, Fritz Haake, and Peter Zoller, 2019, “Digital quantum simulation, Trotter errors, and quantum chaos of the kicked top,” *npj Quantum Inf.* **5**, 78.
- Smith, J., A. Lee, P. Richerme, B. Neyenhuis, P. W. Hess, P. Hauke, M. Heyl, D. A. Huse, and C. Monroe, 2016, “Many-body localization in a quantum simulator with programmable random disorder,” *Nat. Phys.* **12**, 907–911.

- Solano, E., R. L. de Matos Filho, and N. Zagury, 1999, “Deterministic Bell states and measurement of the motional state of two trapped ions,” *Phys. Rev. A* **59**, R2539–R2543.
- Sørensen, Anders, and Klaus Mølmer, 1999, “Quantum Computation with Ions in Thermal Motion,” *Phys. Rev. Lett.* **82**, 1971–1974.
- Sørensen, Anders, and Klaus Mølmer, 2000, “Entanglement and quantum computation with ions in thermal motion,” *Phys. Rev. A* **62**, 022311.
- Srednicki, Mark, 1994, “Chaos and quantum thermalization,” *Phys. Rev. E* **50**, 888–901.
- Steane, A., 1997, “The ion trap quantum information processor,” *Appl. Phys. B* **64**, 623–643.
- Steane, Andrew M., 1999, “Efficient fault-tolerant quantum computing,” *Nature (London)* **399**, 124–126.
- Storch, David-Maximilian, Mauritz van den Worm, and Michael Kastner, 2015, “Interplay of soundcone and supersonic propagation in lattice models with power law interactions,” *New J. Phys.* **17**, 063021.
- Sundar, Bhuvanesh, Roger Paredes, David T. Damanik, Leonardo Dueñas-Osorio, and Kaden R. A. Hazzard, 2019, “A quantum algorithm to count weighted ground states of classical spin Hamiltonians,” [arXiv:1908.01745](https://arxiv.org/abs/1908.01745).
- Suzuki, Masuo, 1985, “Decomposition formulas of exponential operators and Lie exponentials with some applications to quantum mechanics and statistical physics,” *J. Math. Phys. (N.Y.)* **26**, 601–612.
- Sweke, Ryan, Jens Eisert, and Michael Kastner, 2019, “Lieb-Robinson bounds for open quantum systems with long-ranged interactions,” *J. Phys. A* **52**, 424003.
- Swingle, Brian, Gregory Bentsen, Monika Schleier-Smith, and Patrick Hayden, 2016, “Measuring the scrambling of quantum information,” *Phys. Rev. A* **94**, 040302.
- Szabo, Attila, and Neil S. Ostlund, 2012, *Modern Quantum Chemistry: Introduction to Advanced Electronic Structure Theory*, Dover Books on Chemistry (Dover Publications, New York).
- Taylor, J. M., and T. Calarco, 2008, “Wigner crystals of ions as quantum hard drives,” *Phys. Rev. A* **78**, 062331.
- Temme, Kristan, Sergey Bravyi, and Jay M. Gambetta, 2017, “Error Mitigation for Short-Depth Quantum Circuits,” *Phys. Rev. Lett.* **119**, 180509.
- Teoh, Yi Hong, Marina Drygala, Roger G. Melko, and Rajibul Islam, 2020, “Machine learning design of a trapped-ion quantum spin simulator,” *Quantum Sci. Technol.* **5**, 024001.
- Terhal, Barbara M., 2015, “Quantum error correction for quantum memories,” *Rev. Mod. Phys.* **87**, 307–346.
- Titum, Paraj, Erez Berg, Mark S. Rudner, Gil Refael, and Netanel H. Lindner, 2016, “Anomalous Floquet-Anderson Insulator as a Nonadiabatic Quantized Charge Pump,” *Phys. Rev. X* **6**, 021013.
- Titum, Paraj, Joseph T. Iosue, James R. Garrison, Alexey V. Gorshkov, and Zhe-Xuan Gong, 2019, “Probing Ground-State Phase Transitions through Quench Dynamics,” *Phys. Rev. Lett.* **123**, 115701.
- Toyoda, Kenji, Ryoto Hiji, Atsushi Noguchi, and Shinji Urabe, 2015, “Hong-Ou-Mandel interference of two phonons in trapped ions,” *Nature (London)* **527**, 74–77.
- Trabesinger, A., 2012, “Insight issue: Quantum simulation,” *Nat. Phys.* **8**, 264–299.
- Tran, Minh C., Chi-Fang Chen, Adam Ehrenberg, Andrew Y. Guo, Abhinav Deshpande, Yifan Hong, Zhe-Xuan Gong, Alexey V. Gorshkov, and Andrew Lucas, 2020, “Hierarchy of Linear Light Cones with Long-Range Interactions,” *Phys. Rev. X* **10**, 031009.
- Tran, Minh C., A. Deshpande, A. Y. Guo, A. Lucas, and A. V. Gorshkov, 2020, “Optimal state transfer and entanglement generation in power-law interacting systems,” [arXiv:2010.02930](https://arxiv.org/abs/2010.02930).
- Tran, Minh C., Adam Ehrenberg, Andrew Y. Guo, Paraj Titum, Dmitry A. Abanin, and Alexey V. Gorshkov, 2019, “Locality and heating in periodically driven, power-law-interacting systems,” *Phys. Rev. A* **100**, 052103.
- Tran, Minh C., Andrew Y. Guo, Yuan Su, James R. Garrison, Zachary Eldredge, Michael Foss-Feig, Andrew M. Childs, and Alexey V. Gorshkov, 2019, “Locality and Digital Quantum Simulation of Power-Law Interactions,” *Phys. Rev. X* **9**, 031006.
- Trotter, H. F., 1959, “On the product of semi-groups of operators,” *Proc. Am. Math. Soc.* **10**, 545–551.
- Um, Mark, Junhua Zhang, Dingshun Lv, Yao Lu, Shuoming An, Jing-Ning Zhang, Hyunchul Nha, M. S. Kim, and Kihwan Kim, 2016, “Phonon arithmetic in a trapped ion system,” *Nat. Commun.* **7**, 11410.
- Vahala, K., M. Herrmann, S. Knünz, V. Batteiger, G. Saathoff, T. W. Hänsch, and Th. Udem, 2009, “A phonon laser,” *Nat. Phys.* **5**, 682–686.
- Van Regemortel, Mathias, Dries Sels, and Michiel Wouters, 2016, “Information propagation and equilibration in long-range Kitaev chains,” *Phys. Rev. A* **93**, 032311.
- Viola, Lorenza, and Seth Lloyd, 1998, “Dynamical suppression of decoherence in two-state quantum systems,” *Phys. Rev. A* **58**, 2733–2744.
- von Keyserlingk, Curt W., Vedika Khemani, and Shivaji L. Sondhi, 2016, “Absolute stability and spatiotemporal long-range order in Floquet systems,” *Phys. Rev. B* **94**, 085112.
- Wall, Michael L., Arghavan Safavi-Naini, and Ana Maria Rey, 2017, “Boson-mediated quantum spin simulators in transverse fields: XY model and spin-boson entanglement,” *Phys. Rev. A* **95**, 013602.
- Wallraff, A., D. I. Schuster, A. Blais, L. Frunzio, R.-S. Huang, J. Majer, S. Kumar, S. M. Girvin, and R. J. Schoelkopf, 2004, “Strong coupling of a single photon to a superconducting qubit using circuit quantum electrodynamics,” *Nature (London)* **431**, 162–167.
- Wang, C.-C. Joseph, and J. K. Freericks, 2010, “Disentangling phonons from spins in ion-trap-based quantum spin simulators,” [arXiv:1003.5901](https://arxiv.org/abs/1003.5901).
- Wang, C.-C. Joseph, and J. K. Freericks, 2012, “Intrinsic phonon effects on analog quantum simulators with ultracold trapped ions,” *Phys. Rev. A* **86**, 032329.
- Wang, S. T., C. Shen, and L. M. Duan, 2015, “Quantum computation under micromotion in a planar ion crystal,” *Sci. Rep.* **5**, 8555.
- Wecker, Dave, Matthew B. Hastings, and Matthias Troyer, 2015, “Progress towards practical quantum variational algorithms,” *Phys. Rev. A* **92**, 042303.
- Wei, Ken Xuan, Chandrasekhar Ramanathan, and Paola Cappellaro, 2018, “Exploring Localization in Nuclear Spin Chains,” *Phys. Rev. Lett.* **120**, 070501.
- Weidinger, Simon A., Markus Heyl, Alessandro Silva, and Michael Knap, 2017, “Dynamical quantum phase transitions in systems with continuous symmetry breaking,” *Phys. Rev. B* **96**, 134313.
- Wigner, E., 1934, “On the interaction of electrons in metals,” *Phys. Rev.* **46**, 1002.
- Willsch, Madita, Dennis Willsch, Fengping Jin, Hans De Raedt, and Kristel Michielsen, 2019, “Benchmarking the quantum approximate optimization algorithm,” [arXiv:1907.02359](https://arxiv.org/abs/1907.02359).
- Wineland, D. J., C. Monroe, W. M. Itano, D. Leibfried, B. E. King, and D. M. Meekhof, 1998, “Experimental issues in coherent quantum-state manipulation of trapped atomic ions,” *J. Res. Natl. Inst. Stand. Technol.* **103**, 259–328.
- Wineland, David, and Rainer Blatt, 2008, “Entangled states of trapped atomic ions,” *Nature (London)* **453**, 1008–1014.
- Wolfgang, Paul, 1990, “Electromagnetic traps for charged and neutral particles,” *Rev. Mod. Phys.* **62**, 531–540.



- Worm, Mauritz van den, Brian C. Sawyer, John J. Bollinger, and Michael Kastner, 2013, “Relaxation timescales and decay of correlations in a long-range interacting quantum simulator,” *New J. Phys.* **15**, 083007.
- Wright, K., *et al.*, 2019, “Benchmarking an 11-qubit quantum computer,” *Nat. Commun.* **10**, 5464.
- Wu, Jingxiang, and Timothy H. Hsieh, 2019, “Variational Thermal Quantum Simulation via Thermofield Double States,” *Phys. Rev. Lett.* **123**, 220502.
- Wu, Yang-Le, and S. Das Sarma, 2016, “Understanding analog quantum simulation dynamics in coupled ion-trap qubits,” *Phys. Rev. A* **93**, 022332.
- Xu, Jin-Shi, Man-Hong Yung, Xiao-Ye Xu, Sergio Boixo, Zheng-Wei Zhou, Chuan-Feng Li, Alán Aspuru-Guzik, and Guang-Can Guo, 2014, “Demon-like algorithmic quantum cooling and its realization with quantum optics,” *Nat. Photonics* **8**, 113.
- Xu, Kai, *et al.*, 2018, “Emulating Many-Body Localization with a Superconducting Quantum Processor,” *Phys. Rev. Lett.* **120**, 050507.
- Yan, Bo, Steven A. Moses, Bryce Gadway, Jacob P. Covey, Kaden R. A. Hazzard, Ana Maria Rey, Deborah S. Jin, and Jun Ye, 2013, “Observation of dipolar spin-exchange interactions with lattice-confined polar molecules,” *Nature (London)* **501**, 521.
- Yang, Zhi-Cheng, Armin Rahmani, Alireza Shabani, Hartmut Neven, and Claudio Chamon, 2017, “Optimizing Variational Quantum Algorithms Using Pontryagin’s Minimum Principle,” *Phys. Rev. X* **7**, 021027.
- Yao, Norman Y., Chris R. Laumann, Sarang Gopalakrishnan, Michael Knap, Markus Mueller, Eugene A. Demler, and Mikhail D. Lukin, 2014, “Many-Body Localization in Dipolar Systems,” *Phys. Rev. Lett.* **113**, 243002.
- Yao, Norman Y., Andrew C. Potter, I.-D. Potirniche, and Ashvin Vishwanath, 2017, “Discrete Time Crystals: Rigidity, Criticality, and Realizations,” *Phys. Rev. Lett.* **118**, 030401.
- Ye, Jun, H. J. Kimble, and Hidetoshi Katori, 2008, “Quantum state engineering and precision metrology using state-insensitive light traps,” *Science* **320**, 1734–1738.
- Yoshida, Beni, and Norman Y. Yao, 2019, “Disentangling Scrambling and Decoherence via Quantum Teleportation,” *Phys. Rev. X* **9**, 011006.
- Yuan, Xiao, Suguru Endo, Qi Zhao, Ying Li, and Simon C. Benjamin, 2019, “Theory of variational quantum simulation,” *Quantum* **3**, 191.
- Yung, M.-H., J. Casanova, A. Mezzacapo, J. McClean, L. Lamata, A. Aspuru-Guzik, and E. Solano, 2014, “From transistor to trapped-ion computers for quantum chemistry,” *Sci. Rep.* **4**, 3589.
- Zähringer, F., G. Kirchmair, R. Gerritsma, E. Solano, R. Blatt, and C. F. Roos, 2010, “Realization of a Quantum Walk with One and Two Trapped Ions,” *Phys. Rev. Lett.* **104**, 100503.
- Zeiher, Johannes, Jae-yoon Choi, Antonio Rubio-Abadal, Thomas Pohl, Rick van Bijnen, Immanuel Bloch, and Christian Gross, 2017, “Coherent Many-Body Spin Dynamics in a Long-Range Interacting Ising Chain,” *Phys. Rev. X* **7**, 041063.
- Zener, Clarence, 1932, “Non-adiabatic crossing of energy levels,” *Proc. R. Soc. A* **137**, 696.
- Zhang, J., G. Pagano, P.W. Hess, A. Kyprianidis, P. Becker, H. Kaplan, A.V. Gorshkov, Z.X. Gong, and C. Monroe, 2017, “Observation of a many-body dynamical phase transition with a 53-qubit quantum simulator,” *Nature (London)* **551**, 601.
- Zhang, J., *et al.*, 2017, “Observation of a discrete time crystal,” *Nature (London)* **543**, 217.
- Zhang, Jing-Ning, Iñigo Arrazola, Jorge Casanova, Lucas Lamata, Kihwan Kim, and Enrique Solano, 2020, “Probabilistic eigensolver with a trapped-ion quantum processor,” *Phys. Rev. A* **101**, 052333.
- Zhu, D., S. Johri, N. M. Linke, K. A. Landsman, N. H. Nguyen, C. H. Alderete, A. Y. Matsuura, T. H. Hsieh, and C. Monroe, 2019, “Generation of thermofield double states and critical ground states with a quantum computer,” *arXiv:1906.02699*.
- Zhu, D., *et al.*, 2019, “Training of quantum circuits on a hybrid quantum computer,” *Sci. Adv.* **5**, eaaw9918.
- Zhu, Shi-Liang, C. Monroe, and L.-M. Duan, 2006, “Trapped Ion Quantum Computation with Transverse Phonon Modes,” *Phys. Rev. Lett.* **97**, 050505.
- Žunkovič, Bojan, Markus Heyl, Michael Knap, and Alessandro Silva, 2018, “Dynamical Quantum Phase Transitions in Spin Chains with Long-Range Interactions: Merging Different Concepts of Non-equilibrium Criticality,” *Phys. Rev. Lett.* **120**, 130601.
- Žunkovič, Bojan, Alessandro Silva, and Michele Fabrizio, 2016, “Dynamical phase transitions and Loschmidt echo in the infinite-range XY model,” *Phil. Trans. R. Soc. A* **374**, 20150160.